

CYANOMETALLATE COORDINATION POLYMER NANOSTRUCTURES AND THIN
FILMS: SYNTHESIS AND APPLICATIONS

By

IAN AMMON RUMMEL

A DISSERTATION PRESENTED TO THE GRADUATE SCHOOL
OF THE UNIVERSITY OF FLORIDA IN PARTIAL FULFILLMENT
OF THE REQUIREMENTS FOR THE DEGREE OF
DOCTOR OF PHILOSOPHY

UNIVERSITY OF FLORIDA

2009

© 2009 Ian Ammon Rummel

To my wife Julia

ACKNOWLEDGMENTS

I thank my wife Julia for keeping me sane throughout gradschool, my advisor Dr. Talham, Dr. Mark Meisel, Elisabeth Knowles, all current and past members of the Talham group, Dr. Nathan Heston, Dr. John Reynolds, and UF MAIC, and my parents.

TABLE OF CONTENTS

	<u>page</u>
ACKNOWLEDGMENTS	4
LIST OF FIGURES	8
LIST OF ABBREVIATIONS	15
ABSTRACT	16
CHAPTER	
1 INTRODUCTION TO SUPRAMOLECULAR CHEMISTRY AND SYNTHESIS AT THE AIR/WATER INTERFACE	18
Supramolecular Chemistry.....	18
Supramolecular Assembly with Langmuir Monolayers	19
Use of Langmuir Monolayers as a Structure-Directing Element	22
Characterization of Langmuir Monolayers with Underlying Cyanometallate Coordination Networks	24
Brewster Angle Microscopy	24
Attenuated total reflectance infrared spectroscopy	25
Scope of the Thesis	26
2 PRIMITIVE SQUARE NETWORKS AT THE AIR-WATER INTERFACE	32
Introduction	32
Experimental	34
Synthesis	34
Pentacyanoferrate amphiphile synthesis	34
<i>N</i> -methyl-4-(didodecylamino)pyridinium iodide	34
4-(Didodecylamino)pyridine	34
Bis(tetramethylammonium)pentacyano(4-(didodecylamino)-pyridine) ferrate(III)	35
Ru(II/III)tetracarboxylate chloride	36
1,4,8,11-tetraazacyclotetradecane nickel (II) perchlorate	36
1-octadecyl-1,3,6,10,13-pentaazacyclotetradecane nickel (II) chloride.....	37
Materials	37
Instrumentation.....	37
Langmuir Monolayer Preparation	38
Results	39
Synthesis	39
Bis(tetramethylammonium)pentacyano(4-(didodecylamino)-pyridine) ferrate(III)	39
Ru(II/III)tetracarboxylate chloride	39
1,4,8,11-tetraazacyclotetradecane nickel (II) perchlorate	39
1-octadecyl-1,3,6,10,13-pentaazacyclotetradecane nickel (II) chloride.....	40

Macrocyclic Ni ^{II} Amphiphile with K ₄ Fe(CN) ₆ Subphase.....	40
Surface pressure vs. mean molecular area isotherms	40
BAM	40
ATR FT-IR	41
XPS.....	41
AFM.....	41
Creep observations	41
Pentacyanoferrate Amphiphile with Macrocyclic Tetraaza Ni (II) Subphase	42
Surface pressure vs. mean molecular area isotherms	42
BAM	43
XPS.....	43
Pentacyanoferrate Amphiphile with Ru (II/III) Tetracarboxylate Subphase	43
Surface pressure vs. mean molecular area isotherms	43
BAM	44
ATR FT-IR	44
XPS.....	44
Discussion.....	45
Macrocyclic Ni ^{II} Amphiphile with K ₄ Fe(CN) ₆ Subphase.....	45
Pentacyanoferrate Amphiphile with Macrocyclic Tetraaza Ni (II) Subphase	46
Pentacyanoferrate Amphiphile with Ru (II/III) Tetracarboxylate Subphase	47
General Discussion	47
Conclusions and Future Work.....	49
3 CYANOMETALLATE OLIGOMERS AS BUILDING UNITS IN SUPRAMOLECULAR BUILDING BLOCKS AT THE AIR/WATER INTERFACE	68
Introduction	68
Experimental	69
Synthesis.....	69
Monolayer Preparation.....	69
Results	69
Surface Pressure vs. Mean Molecular Area Isotherms	69
BAM	70
ATR FT-IR.....	70
XPS.....	70
SQUID Magnetometry.....	71
Discussion.....	71
Conclusions	73
4 PRUSSIAN BLUE/TITANIUM DIOXIDE NANOCOMPOSITES.....	79
Introduction	79
Experimental	83
Synthesis.....	83
Prussian blue nanoparticles	83
Ni ^{II} Cr ^{III} PBA nanoparticles	83
TiO ₂ -Coated Prussian Blue Particles	84

Thallium Staining for TEM Analysis	84
Photo-oxidative Experiments	84
Visible Light-Induced Charge Transfer Evaluation	85
Materials	85
Instrumentation	85
Results	86
Prussian Blue/TiO ₂ Nanocomposite Synthesis	86
NiCr PBA/TiO ₂ Nanocomposite Synthesis	86
UV Photo-Induced Charge Transfer Evaluation	86
Photocatalysis	88
Visible Light Sensitization with Rhodamine B.	88
Discussion	89
Conclusions and Future Work	91
5 PRUSSIAN BLUE ANALOGS AS SOLID ELECTROLYTES FOR DYE- SENSITIZED SOLAR CELLS	103
Introduction	103
Dye-Sensitized Solar Cells	103
DSSC Electrolytes	104
Prussian Blue Analogs as Solid DSSC Electrolytes	105
Experimental	107
Dye Synthesis	107
Dyed TiO ₂ Electrode Fabrication	108
PBA electrolyte deposition	109
Back electrode deposition	110
Efficiency measurements	110
Results	110
(4,4'-dcbpy) ₂ (CN) ₂ Ru(II) Dye Synthesis	110
Finished Cell	111
PBA Deposition	111
CoFe PBA Penetration into TiO ₂ Film	112
Cell Efficiency Under Simulated Sunlight	112
Discussion	113
Conclusions and Future Work	114
6 CONCLUSION	127
APENDIX: FT-IR SPECTRA OF SYNTHESIZED COMPOUNDS	130
LIST OF REFERENCES	134
BIOGRAPHICAL SKETCH	144

LIST OF FIGURES

<u>Figure</u>	<u>page</u>
1-1	A material with a specific geometry created via the supramolecular assembly of smaller molecular building blocks that bind in a predictable way. ² 27
1-2	The various phase transitions of a Langmuir monolayer as it is compressed. 27
1-3	A Langmuir monolayer being transferred onto a hydrophilic substrate..... 28
1-4	Control of a Langmuir monolayer's geometry via formation of an underlying coordination network. A) Free amphiphiles B) Amphiphiles with binding subphase component and C) Amphiphiles ordered by network formation. 28
1-5	A face-centered square network created from an iron-containing amphiphile over an aqueous subphase containing Ni ²⁺ ions. Alkyl tails on the amphiphiles are omitted for clarity..... 29
1-6	Surface pressure vs. mean molecular area isotherm of Culp's pentacyano amphiphile over a NaCl subphase (open circles) and Ni ²⁺ subphase (filled circles). ²¹ 29
1-7	FT-IR spectra of the pentacyanoferrate amphiphile after spreading over a Ni ²⁺ subphase (a) and in a KBr pellet (b). ²¹ 30
1-8	GXR spectrum of a 30-bilayer sample of Culp's centered-square cyanometallate monolayer material. ²¹ 30
1-9	Field-cooled temperature-dependant magnetization of the centered-square film material taken at 20 G while the sample is aligned parallel to the applied field (filled circles) and perpendicular to the applied field (open circles)..... 31
2-1	A centered square two-dimensional network formed by two four-coordinate components (left) and a primitive square two-dimensional network formed by one four-coordinate component and one two-coordinate component (right). 52
2-2	The geometry of the expected film produced by reacting a Langmuir monolayer of amphiphile 1 with subphase component 3. Alkyl tails are omitted to the right for clarity. 52
2-3	The geometry of the expected film produced by reacting a Langmuir monolayer of amphiphile 1 with subphase component 4. Alkyl tails are omitted to the left for clarity..... 53
2-4	A bulk primitive-cubic cyanometallate material with an analogous structure to the network in Figure 2-2 and 2-6. ²⁶ 53

2-5	A bulk ruthenium dimer/cyanometallate material with a structure analogous to the monolayer network in Figure 2-3. ²⁷	54
2-6	The geometry of the expected film produced by reacting a Langmuir monolayer of amphiphile 2 with $\text{Fe}(\text{CN})_6^{4-}$ in the subphase.	54
2-7	Synthesis of bis(tetramethylammonium)pentacyano(4-(didodecylamino)-pyridine) ferrate(III).....	55
2-8	Synthesis of Ru (II/III) tetracarboxylate chloride.	55
2-9	Synthesis of 1,4,8,11-tetraazacyclotetradecane nickel (II) perchlorate.	55
2-10	Synthesis of 1-octadecyl-1,3,6,10,13-pentaazacyclotetradecane nickel (II) chloride (1).....	56
2-11	Surface pressure vs. mean molecular area of amphiphile 2 over subphases of 0.5M NaCl and 0.42M NaCl+0.02M $\text{K}_4\text{Fe}(\text{CN})_6$	56
2-12	BAM images of macrocyclic Ni^{2+} amphiphile, 2 , at various mean molecular areas over a 0.5 M NaCl subphase.	56
2-13	BAM images of macrocyclic Ni^{2+} amphiphile at various mean molecular areas over a 0.42 M NaCl/0.02M $\text{K}_4\text{Fe}(\text{CN})_6$ subphase.	57
2-14	ATR FT-IR spectra of four layers of amphiphile 2 over a 0.42 M NaCl/0.02M $\text{K}_4\text{Fe}(\text{CN})_6$ subphase.....	57
2-15	The cyanide stretching region of ATR FT-IR spectra of four layers of amphiphile 2 over a 0.42 M NaCl/0.02M $\text{K}_4\text{Fe}(\text{CN})_6$ subphase.	57
2-16	The CH_2 stretching region of ATR FT-IR spectra of four layers of amphiphile 2 over a 0.42 M NaCl/0.02M $\text{K}_4\text{Fe}(\text{CN})_6$ subphase (dashed) and 0.5 M NaCl subphase (solid).	58
2-17	An XPS survey scan of amphiphile 2 over a subphase of $\text{K}_4\text{Fe}(\text{CN})_6$ after transfer to a Si substrate.	58
2-18	An XPS multiplex scan of the Ni 2p _{3/2} peak region of amphiphile 2 over a subphase of $\text{K}_4\text{Fe}(\text{CN})_6$ after transfer to a Si substrate.....	59
2-19	An XPS multiplex scan of the Fe 2p _{3/2} peak region of amphiphile 2 over a subphase of $\text{K}_4\text{Fe}(\text{CN})_6$ after transfer to a Si substrate.....	59
2-20	Tapping mode AFM of a monolayer of amphiphile 2 prepared over a ferrocyanide subphase after transfer to an OTS-coated Si substrate.....	59

2-21	Mean molecular area vs. time of a monolayer of amphiphile 2 over a 0.42 M NaCl/0.02M K ₄ Fe(CN) ₆ subphase held at a constant surface pressure of 1 mN/m.	60
2-22	Rigid islands of macrocyclic Ni ²⁺ amphiphile over a ferrocyanide subphase held at 1 mN/m. a) time=0 minutes. b) time=60 minutes. c) t=100 minutes.	60
2-23	Collapse of macrocyclic Ni ²⁺ amphiphile over ferrocyanide at 50 Å ² . a) With continuous compression. b) After equilibrating at 1 mN/m for 100 minutes	61
2-24	Isotherm of pentacyanoferrate amphiphile 1 over a 1mM NaCl subphase (open) and 1mM Ni(II)cyclam subphase (solid).	61
2-25	BAM observations of the pentacyanoferrate amphiphile 1 over 1 mM Ni(II)cyclam (left) and 1 mM NaCl (right).....	62
2-26	XPS scan of the pentacyanoferrate amphiphile 1 over a Ni(II) cyclam subphase after transfer to an Si substrate.	62
2-27	Multiplex XPS scan of the Fe region of the pentacyanoferrate amphiphile 1 over a Ni(II) cyclam subphase after transfer to a Si substrate.	63
2-28	Multiplex XPS scan of the Fe region of the pentacyanoferrate amphiphile 1 over a Ni(II) cyclam subphase after transfer to a Si substrate.	63
2-29	Surface pressure vs. mean molecular area isotherms of amphiphile 2 over a Ru(II/III) dimer subphase after 1, 3, and 16 hours.	64
2-30	BAM images of amphiphile 1 over a 1 mM Ru(II/III)Cl / 1mM NaCl subphase immediately after spreading (left) and after four hours (right) at 200 Å ²	64
2-31	ATR FT-IR spectrum of the pentacyanoferrate amphiphile 1 over the Ru(II/III) carboxylate dimer 4	65
2-32	Cyanide stretching region of the ATR FT-IR spectrum of the pentacyanoferrate amphiphile 1 over the Ru(II/III) carboxylate dimer 4	65
2-33	Carboxylate stretching region of the ATR FT-IR spectrum of the pentacyanoferrate amphiphile 1 over the Ru(II/III) carboxylate dimer 4	65
2-34	CH ₂ stretching region of the ATR FT-IR spectrum of the pentacyanoferrate amphiphile 1 over the Ru(II/III) carboxylate dimer 4	66
2-35	A survey scan of a monolayer of amphiphile 1 over a subphase of ruthenium carboxylate dimer.	66
2-36	The iron 2p _{3/2} XPS peak region of a monolayer of amphiphile 1 over a subphase of ruthenium carboxylate dimer.	66

2-37	The ruthenium 3p3 XPS peak region of a monolayer of amphiphile 1 over a subphase of ruthenium carboxylate dimer.	67
3-1	A <i>trans</i> -[(py) ₄ Ru[M(CN) ₆] ₂] ⁴⁻ trimer molecule	74
3-2	Surface pressure vs. mean molecular area isotherm of macrocyclic Ni amphiphile over NaCl subphase (circles), CrRuCr trimer subphase (square), and FeRuFe trimer (triangles).....	74
3-3	BAM of macrocyclic Ni amphiphile over CrRuCr trimer subphase at 200 Å ² (right), 160 Å ² (center) and 120 Å ² (left).....	74
3-4	BAM of macrocyclic Ni amphiphile over FeRuFe trimer subphase at 200 Å ² (right), 160 Å ² (center) and 120 Å ² (left).....	75
3-5	ATR FT-IR spectrum of the macrocyclic Ni amphiphile over a CrRuCr trimer subphase, transferred to a Si ATR crystal.	75
3-6	Cyanide stretching region of ATR FT-IR spectrum of the macrocyclic Ni amphiphile over a CrRuCr trimer subphase, transferred to a Si ATR crystal.	75
3-7	ATR FT-IR spectrum of macrocyclic Ni amphiphile over FeRuFe trimer subphase, transferred to a Si ATR crystal.	76
3-8	XPS spectrum of the macrocyclic Ni amphiphile over CrRuCr trimer subphase.	76
3-9	XPS spectrum of macrocyclic Ni amphiphile over FeRuFe trimer subphase.	77
3-10	Magnetic characterization of the macrocyclic Ni amphiphile over CrRuCr trimer subphase. Paramagnetic magnetization (M _p) as a function of magnetic field (H) (left) and paramagnetic susceptibility (χ _p) as a function of temperature (T) (right).....	77
3-9	Magnetic characterization of the macrocyclic Ni amphiphile over FeRuFe trimer subphase. Paramagnetic magnetization (M _p) as a function of magnetic field (H) (left) and paramagnetic susceptibility (χ _p) as a function of temperature (T) (right).....	78
4-1	A cubic unit cell of Prussian blue lattice	96
4-2	Relative orbital energy levels of Prussian blue and TiO ₂ vs. Ag/AgCl	96
4-3	Number of electrons that a Prussian blue (open) and silver (filled) nanoparticle can store vs. size. The number of electrons that Prussian blue can store increases linearly with volume, while the number of electrons that silver can store increases linearly with surface area.	97

4-4	Relative orbital energy levels of Prussian blue, TiO ₂ , and rhodamine B.....	97
4-5	Synthesis of TiO ₂ coated Prussian blue nanoparticles	98
4-6	TEM of Prussian blue nanoparticles before TiO ₂ coating (left), TiO ₂ -coated Prussian blue particles after TI staining(center). TEM of TiO ₂ product prepared without PB nanoparticles in suspension, with lacy carbon grid visible (right).	98
4-7	TEM of NiCr PBA before TiO ₂ coating (left), TiO ₂ -coated NiCr PBA particles (right).....	98
4-8	UV-Vis spectra of Prussian blue nanoparticles before and after TiO ₂ coating. ...	99
4-9	Prussian blue/TiO ₂ nanocomposite before and after irradiation.....	99
4-10	Absorption of the Prussian blue/TiO ₂ nanocomposite vs. time as the UV lamp it turned on and off.	100
4-11	Comparison of decrease in intervalence charge transfer absorption vs. UV irradiation time in Prussian blue/TiO ₂ nanocomposite (open circles) and separately prepared TiO ₂ and Prussian blue (filled circles).....	100
4-12	Comparisons of the amount of benzyl aldehyde oxidation product produced upon irradiation of benzyl alcohol with PB/TiO ₂ nanoparticles, NiCr BPA control nanoparticles, and no nanoparticles.....	101
4-13	Comparisons of the amount of acetone oxidation product produced upon irradiation of isopropanol with PB/TiO ₂ nanoparticles, NiCr BPA control nanoparticles, and no nanoparticles.....	102
4-14	UV-Vis spectra of Prussian blue/TiO ₂ nanocomposite in the presence of rhodamine B before irradiation (blue), after irradiation (yellow), and after irradiation in the presence of I ⁻	102
5-1	Mechanism of a Gratzel cell.....	119
5-2	Relative energy levels of TiO ₂ , sensitizing dye, and Prussian blue analog necessary for a DSSC to function with a solid PBA electrolyte.....	119
5-4	Synthesis of the (4,4'-dcbpy) ₂ (CN) ₂ Ru(II) dye	120
5-5	Schematic of finished cell	120
5-6	SEM of the TiO ₂ film at various magnifications.....	121
5-7	SEM of the TiO ₂ film at various magnifications after 15 deposition cycles of the FeCr PBA from water. Desiccation cracks are visible in the center and right images.	121

5-8	SEM of the TiO ₂ film at various magnifications after 30 deposition cycles of the FeCr PBA from water. Desiccation cracks are visible in the center and right images.	121
5-9	SEM of the TiO ₂ film at various magnifications after 45 deposition cycles of the FeCr PBA from water. Desiccation cracks are visible in the center and right images.	122
5-10	Tapping mode AFM image of the TiO ₂ film before PBA deposition (left). AFM Depth profile of the TiO ₂ film before PBA deposition (right).	122
5-11	Tapping mode AFM of the TiO ₂ film after 45 FeCr PBA deposition cycles(left). AFM Depth profile of the TiO ₂ film after PBA deposition (right).....	122
5-12	SEM of the TiO ₂ film at various magnifications after 10 deposition cycles of the FeCr PBA from methanol.....	123
5-13	SEM of the TiO ₂ film at various magnification after 20 deposition cycles of the FeCr PBA from methanol.....	123
5-14	SEM of the TiO ₂ film at various magnifications after 30 deposition cycles of the FeCr PBA from methanol.....	123
5-15	SEM of the TiO ₂ film at various magnifications after 40 deposition cycles of the FeCr PBA from methanol.....	124
5-16	SEM of the TiO ₂ film at various magnifications after 5 deposition cycles of the CoFe PBA from water.	124
5-17	SEM of the TiO ₂ film at various magnifications after 15 deposition cycles of the CoFe PBA from water.	124
5-18	SEM of the TiO ₂ film at various magnifications after 30 deposition cycles of the CoFe PBA from water.	125
5-19	SEM of the TiO ₂ film at various magnifications after 70 deposition cycles of the CoFe PBA from water. A desiccation crack is visible in the left image.	125
5-20	Area of EDS analysis on broken PBA-coated TiO ₂ film.....	125
5-21	Photocurrent vs. voltage curve for the FeCr PBA cell	126
5-22	Photocurrent vs. voltage curve for the CoFe PBA cell.....	126
A-1	FT-IR spectrum of Bis(tetramethylammonium)pentacyano(4-(didodecylamino)-pyridine) ferrate(III)	130
A-2	FT-IR spectrum of 1-4-8-11 tetraazacyclotetradecane nickel (II) perchlorate ...	130

A-3	FT-IR spectrum of 1-octadecyl-1-3-6-10-13 pentaazacyclotetradecane nickel (II) chloride.....	131
A-4	FT-IR spectrum of Ru(II/III)tetracarboxylate chloride.....	131
A-5	FT-IR spectrum of Prussian blue nanoparticles	132
A-6	FT-IR spectrum of NiCR Prussian blue analog nanoparticles	132
A-7	FT-IR spectrum of $(4,4'\text{-dcbpy})_2(\text{CN})_2\text{Ru(II)}$	133

LIST OF ABBREVIATIONS

AFM	Atomic force microscopy
ATR	Attenuated total reflectance
BAM	Brewster angle microscopy
DSSC	Dye-sensitized solar cell
FT-IR	Fourier-transform infrared
FTO	Fluorine-doped tin oxide
HOMO	Highest occupied molecular orbital
LUMO	Lowest unoccupied molecular orbital
OTS	Octadecyltrichlorosilane
PB	Prussian blue
PBA	Prussian blue analog
QCM	Quartz crystal microbalance
SEM	Scanning electron microscopy
TEM	Transmission electron microscopy
TTEAIP	Titanium triethanolaminoisopropoxide
UV-Vis.	Ultraviolet-visible
XPS	X-ray photoelectron spectroscopy

Abstract of Dissertation Presented to the Graduate School
of the University of Florida in Partial Fulfillment of the
Requirements for the Degree of Doctor of Philosophy

CYANOMETALLATE COORDINATION POLYMER NANOSCTRUCTRE AND THIN
FILMS: SYNTHESIS AND APPLICATIONS

By

Ian Ammon Rummel

December 2009

Chair: Daniel Talham

Major: Chemistry

Prussian blue analogs (PBAs) are cyanometallate coordination polymers whose electronic properties can be modified by varying the material's constituent metals. This research investigated how the structural and electronic properties of PBA nanostructures such as monolayers, thin films, and nanoparticles can be exploited in applications related to charge storage, solid-state electrolytics, and supramolecular assembly of materials.

It was demonstrated herein that two-dimensional monolayers of PBA with specific geometries can be synthesized at the air/water interface by employing blocking ligands when reacting an amphiphilic monolayer with aqueous subphase components. Charge balance was found to be a key consideration in such systems. The feasibility of creating two-dimensional networks of PBA at the air/water interface by employing more complex oligomeric cyanometallate subphase species was also investigated. It was hoped that such networks would demonstrate ferromagnetism due to coupling between the cyanometallate oligomers and the amphiphilic monolayer component. Although evidence of cyanometallate network formation was present, no evidence of magnetic interactions was observed.

The charge-storage capabilities of PB were investigated by creating nanoparticles of PB coated in TiO₂. It was demonstrated that photo-excited electrons from the TiO₂ transferred into the PB upon irradiation with near-UV light, that the electrons could be removed by oxidizing the PB, and that the material could be cycled multiple times.

Finally, thin films of PBA were deposited onto dyed TiO₂ substrates to investigate the feasibility of using PBAs as solid-state electrolytes in DSSCs. The efficiency of the resulting cells was found to be extremely low, likely due to poor contact between the highly-porous TiO₂ film and the PBA.

CHAPTER 1
INTRODUCTION TO SUPRAMOLECULAR CHEMISTRY AND SYNTHESIS AT THE
AIR/WATER INTERFACE

Supramolecular Chemistry

Supramolecular chemistry has gained increasing popularity as a synthetic technique for creating novel materials with complex structures and unusual properties. By combining relatively simple chemical building blocks that react in predictable ways, chemists can control the structure of materials on a scale that is far smaller than is normally accessible to conventional nano-fabrication techniques. (Figure 1-1) ¹

To rationally design supramolecular architectures, chemists must consider how intra-molecular forces like hydrogen bonding, hydrophobic/hydrophilic interactions, π stacking, electrostatic interactions, and covalent or coordinate-covalent bonding geometry will order the reactants and influence the geometry of the resulting material. All of these interactions represent “structure directing elements” that allow the synthetic chemist to control the final structure of the resulting material.³

Transition metal complexes are particularly attractive building blocks in supramolecular chemistry, thanks to their wide range of geometries and the ease with which synthetic chemists can control their binding motifs by varying their ligands.² The use of transition metals also allows the synthetic chemist to take advantage of the diverse optical, catalytic, and magnetic properties of transition metals. Many new materials created through supramolecular assembly of transition metal complexes have been demonstrated with complex geometries and novel properties,⁴⁻¹⁰ and such materials have found applications in fields such as gas storage¹¹⁻¹³ and chemical sensing.¹⁴ Electrical circuit components in particular are continuously shrinking, and will

soon be at a scale where molecular-level control of their geometry is necessary for their proper functioning.

Although the applications for nano-scale materials created through supramolecular assembly are numerous, in order to employ these materials in useful devices it will likely be necessary to position them onto surfaces. Since present techniques for manipulating nano-scale structures on surfaces are limited and inefficient, an attractive alternative to synthesizing and then positioning nano-scale structures is to synthesize them directly onto surfaces.

One technique for synthesizing supra-molecular assemblies onto surfaces that has been investigated by our research group is the creation of supramolecular materials at the air/water interface by employing Langmuir monolayers. The feasibility of using the interface as a structure-directing element was investigated, as well as how traditional supramolecular structure-directing elements change when employed in interfacial synthesis. The restriction of molecules in Langmuir monolayers to two dimensions was found to serve as a useful structure-directing element for controlling the geometry of the resulting material, allowing the synthetic chemist to force materials to adopt a two-dimensional geometry when it might otherwise take on a three-dimensional structure.

Supramolecular Assembly with Langmuir Monolayers

Langmuir monolayers are a well-established technique for creating thin films at the air/water interface. The basic principles of a Langmuir monolayer are outlined in Figure 1-2. An amphiphilic molecule is dissolved in a volatile, water-insoluble solvent like chloroform, methylene chloride, or hexane. Small quantities of water-soluble solvents such as methanol or benzene are sometimes included when necessary to completely dissolve the amphiphilic material. When the solution is dripped onto the

surface of water the organic solvent quickly evaporates, leaving the amphiphiles behind to float on the water's surface. If the average area available to each amphiphile molecule on the water's surface is large relative to the area taken up by the amphiphiles, the amphiphiles will spread out as a two-dimensional pseudo-gas and have little interaction with each other. The amphiphiles can then be forced to pack together and order by lowering their available area on the water's surface via a movable barrier that compresses the amphiphilic monolayer.

As the barrier compresses the monolayer, the amphiphiles begin to interact and may undergo one or more phase transitions. The initial phase, which is analogous to a two-dimensional gas, will begin to transition to a "liquid expanded" phase, a two-dimensional liquid analog. Although amphiphiles in the liquid expanded phase are condensed and interacting with their neighbors, they lack long-range order and are fluid. Further compression leads to more interaction between the amphiphiles, eventually causing them to transition to the liquid condensed phase that is similar to a two-dimensional solid in which the amphiphiles have orientational ordering but little positional ordering. Not all Langmuir monolayers will necessarily display all three phases or distinct phase transitions, and phase behavior will vary depending on factors such as temperature and the nature and concentration of any ions that are present in the aqueous subphase. To promote amphiphile spreading and distinct phase behavior it is often necessary to dissolve ions into the aqueous subphase to increase its ionic strength, promoting interaction between the subphase and the amphiphile's hydrophilic head group.

The lateral pressure within the Langmuir monolayer can be monitored through the use of a Wilhelmy balance that is suspended through the monolayer. As the monolayer is compressed by the movable barrier, amphiphiles will begin to interact with each other and experience pressure along the plane of the monolayer. This “surface pressure,” Π , of the monolayer is given by:

$$\Pi = \gamma_w - \gamma_m$$

where γ_w is the surface tension of water (73 mN/m at STP) and γ_m is the apparent surface tension when the monolayer is present. Π is therefore in units of millinewtons of force per meter of Wilhelmy balance.

Isothermal plots of the monolayer’s surface pressure vs. the mean molecular area available to each amphiphilic molecule (determined by dividing the number of amphiphilic molecules present in the film by the film’s area) are frequently used to study monolayer behavior. The monolayer’s surface pressure will increase as a given phase is compressed. Often coexistence of two phases will be possible at a given area, which will be reflected as plateaus in the monolayer’s surface pressure vs. mean molecular area isotherm. Continued compression of the monolayer beyond the liquid condensed phase will eventually result in the collapse of the monolayer. Collapse could occur when the monolayer buckles upward or downward, or rearranges into multilayers that begin sliding over each other. Collapse will usually be evidenced by a sudden decrease in the slope of the liquid condensed phase’s surface pressure vs. mean molecular area isotherm.

Care must be taken to properly balance the hydrophilicity and hydrophobicity of the amphiphile molecules. If the hydrophilic chain is too long, the amphiphiles will not

disperse on the water's surface. If it is too short, they will quickly dissolve away into the aqueous subphase.

Once a Langmuir monolayer has been prepared, it can be transferred onto a solid substrate for further analysis. If the monolayer is to be transferred onto a hydrophobic substrate, the substrate is slowly lowered horizontally into the monolayer. The amphiphiles in the monolayer attach to the substrate in order to relieve surface pressure. Once the substrate has been lowered as far as desired, it can then be slowly raised back up, resulting in the transfer of a second layer of material. By repeatedly raising and lowering the substrate while maintaining the desired surface pressure, many layers can be transferred.

Similarly, a hydrophilic substrate can be positioned below the surface of the water prior to spreading and compressing the amphiphiles. Upon reaching the desired surface pressure, the substrate is slowly raised vertically up through the monolayer, causing the hydrophilic head groups of the amphiphiles to adhere to the substrate. Again, the substrate can then be re-lowered and raised again to transfer multiple layers as necessary (Figure 1-3). A horizontal dipping technique in which a hydrophobic substrate is held parallel to the surface of the monolayer and slowly lowered until it contacts the alkyl tails and then raised is also used.

Use of Langmuir Monolayers as a Structure-Directing Element

Although Langmuir monolayers can serve as a useful tool for controlling the geometry of supramolecular assemblies by confining reactants to two dimensions, they suffer from a general lack of long-range order between the amphiphiles, even when at high pressures in the liquid-condensed phase. In order to create solid films with extended order, it is necessary to introduce further structure-directing elements.

One approach investigated by our research group for the synthesis of Langmuir monolayers with extended order is the reaction of the amphiphiles within the monolayer with dissolved subphase components to create an extended two-dimensional coordinate-covalent network. This locks the normally-disordered amphiphiles into an ordered geometry that is dictated by the geometry of the underlying coordinate-covalent network (Figure 1-4).¹⁵⁻²²

Specifically, Culp used Fe^{III}-containing amphiphiles with cyanide ligands spread over an aqueous subphase solution containing various divalent transition metal ions to generate a face-centered square grid network equivalent to a two-dimensional sheet of Prussian Blue analog (Figure 1-5).²¹

When the resulting monolayers were prepared over an aqueous subphase containing divalent transition metal ions, they had significantly different surface pressure vs. mean molecular area isotherms than when prepared over a non-coordinating NaCl subphase (Figure 1-6). The surface pressure began increasing at a much lower mean molecular area over the divalent metal subphase, and the slope of the increase was much greater. The mean molecular area at which the surface pressure began to increase is notably close to the expected mean area per amphiphile in the target centered-square network, while the sharp increase in slope is consistent with the creation of a rigid network that resists compression. Interestingly, the mean molecular area at collapse over the NaCl subphase is larger than the mean molecular area at collapse over the Ni²⁺ subphase. This indicates that the creation of the underlying cyanometallate network forces the amphiphiles closer together than they could ordinarily be packed under lateral compression.

ATR FT-IR analysis of the resulting films indicated a substantial shift in the stretching frequency of the pentacyanoferrate cyanide ligands (Figure 1-7). This blue-shift in the cyanide's stretching frequency is consistent with the formation of Fe^{3+} -CN- Ni^{2+} bonds in an extended cyanometallate network.

Final conformation of the material's structure was accomplished via grazing-incidence x-ray diffraction (GXR), which detected the diffraction peaks corresponding to the $\langle 2,0 \rangle$, $\langle 2,2 \rangle$, and $\langle 4,0 \rangle$ two-dimensional lattice planes (Figure 1-8).

The cyanometallate monolayers were found to be magnetically anisotropic, with the magnitude of the film's low-temperature ferromagnetism varying substantially depending on whether the films were oriented parallel or perpendicular to the applied field (Figure 1-9).

Characterization of Langmuir Monolayers with Underlying Cyanometallate Coordination Networks

Brewster Angle Microscopy

Brewster angle microscopy (BAM) is a well-established technique for studying the behavior of amphiphiles in Langmuir monolayers.²³⁻²⁵ When polarized light strikes the interface between materials of different refractive indices at an angle equal to the inverse tangent of the ratio of the refractive indices of the two materials, it will be completely internally refracted with no external reflection. This angle, $\theta = \tan^{-1}(n_2/n_1)$, is known as the Brewster angle. For visible light striking the interface between air and water, Brewster's angle is approximately 53° .

A typical BAM experiment involves positioning a camera and polarized light source opposite one another above the surface of the water on which the Langmuir monolayer is formed. If the polarized light source is shining onto the surface at

Brewster's angle, the camera will not detect any reflected light and the resulting image will appear black. When a Langmuir monolayer is spread over the surface of the water, the monolayer's different refractive index will mean that the incident light is no longer striking precisely at the Brewster angle, causing some portion of the incident light to be externally reflected. The result is that areas of uncovered water will appear black in a BAM image, while regions of monolayer will appear lighter.

The extent to which the monolayer's different refractive index causes reflection will depend on the density of the monolayer. Areas of high density will appear brighter, which allows the experimenter to observe the monolayer undergoing phase transitions; the monolayer will brighten as it undergoes transitions to more condensed phases. If the amphiphiles in a Langmuir monolayer are being ordered into a lattice by an underlying coordinate-covalent network, their density will be controlled by the geometry of the network rather than the weak interactions between amphiphiles and mean available area per amphiphile that usually determines a monolayer's density and phase. This makes BAM a useful technique for monitoring whether or not a coordinate-covalent network is forming under the monolayer.

BAM can also be useful for observing the fluidity of the monolayer. In a typical monolayer in the liquid-expanded/liquid-condensed coexistence region, the high-density regions will be fluid and change shape as they are compressed into each other. If the monolayer is ordered by a coordinate-covalent network, on the other hand, it will usually form rigid condensed regions that are resistant to changing shape.

Attenuated total reflectance infrared spectroscopy

The extremely small amount of amphiphile material present in a Langmuir monolayer presents a special challenge when attempting to analyze it with IR

spectroscopy. To provide a sufficiently high signal to noise ratio with such a tiny amount of sample, the monolayer can be transferred onto an attenuated total reflectance (ATR) crystal prior to analysis.

The symmetric and asymmetric methylene stretching region is usually of particular interest when analyzing Langmuir monolayers with FT-IR. Amphiphiles will typically have long alkyl tails, producing an intense CH₂ signature in the IR spectrum. The exact position of the CH₂ absorption will depend on whether the alkyl tails are in a trans or gauche configuration, with trans bonds slightly red-shifted relative to the gauche bonds. The CH₂ absorption width is affected by the extent to which the alkyl tail in the monolayer are ordered, with more ordered alkyl tails producing narrower peaks.

If the underlying coordinate-covalent network is a cyanometallate network, it can also be informative to examine the cyanide stretching region. Terminal metal-cyanides typically have lower stretching frequencies than bridging metal-cyanides, so shifts in the CN frequency can indicate whether or not an extended network is forming.

Scope of the Thesis

Herein several topics related to supramolecular assemblies and nanostructures of cyanometallate materials will be investigated. Chapter 2 will describe the use of blocking ligands to control the geometry of cyanometallate monolayers prepared at the air/water interface. In Chapter 3, the use of more complex cyanometallate oligomers as supramolecular building blocks in the creation of magnetic films at the air/water interface will be reported. Chapter 4 will investigate the use of Prussian blue nanoparticles coupled to TiO₂ for storage of photo-excited electrons. In Chapter 5, the use of thin films of PBAs as solid electrolytes in dye-sensitized solar cells will be described. General conclusions and future work will be summarized in chapter 6.

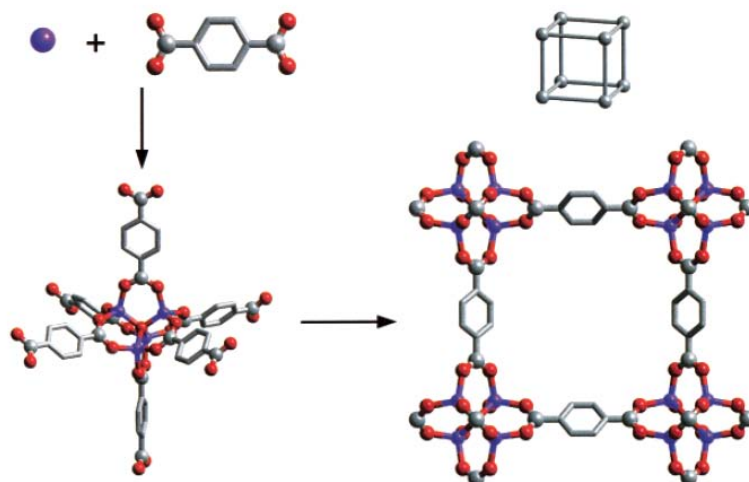


Figure 1-1. A material with a specific geometry created via the supramolecular assembly of smaller molecular building blocks that bind in a predictable way.²

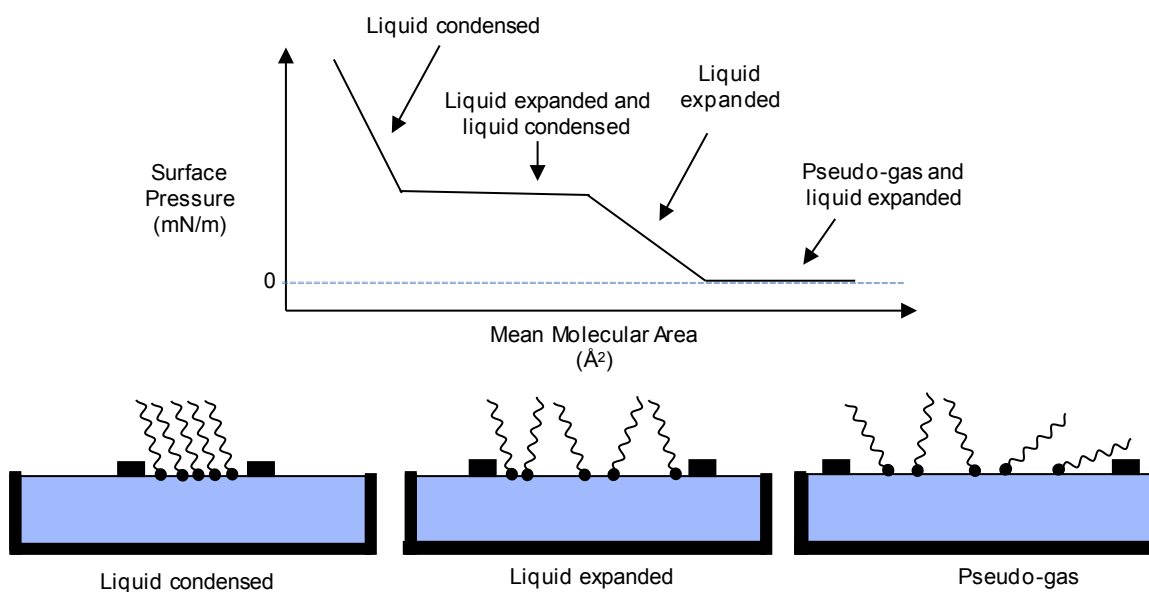


Figure 1-2. The various phase transitions of a Langmuir monolayer as it is compressed.

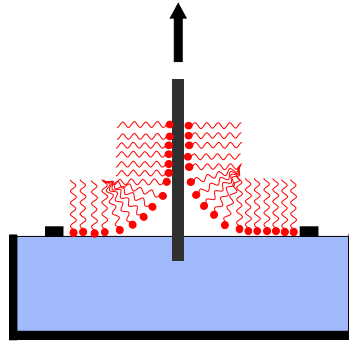


Figure 1-3. A Langmuir monolayer being transferred onto a hydrophilic substrate.

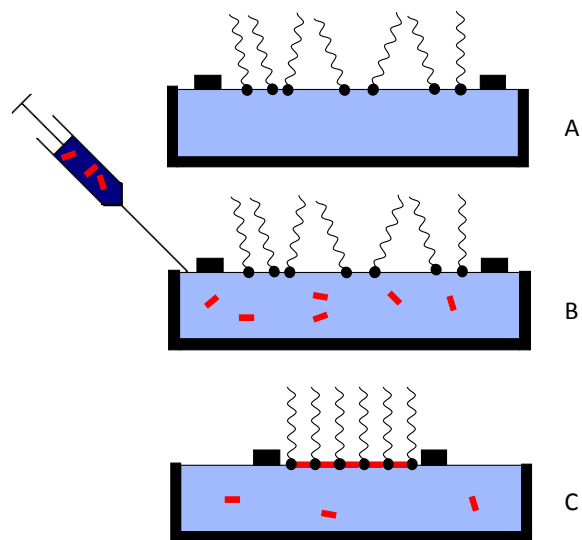


Figure 1-4. Control of a Langmuir monolayer's geometry via formation of an underlying coordination network. A) Free amphiphiles B) Amphiphiles with binding subphase component and C) Amphiphiles ordered by network formation.

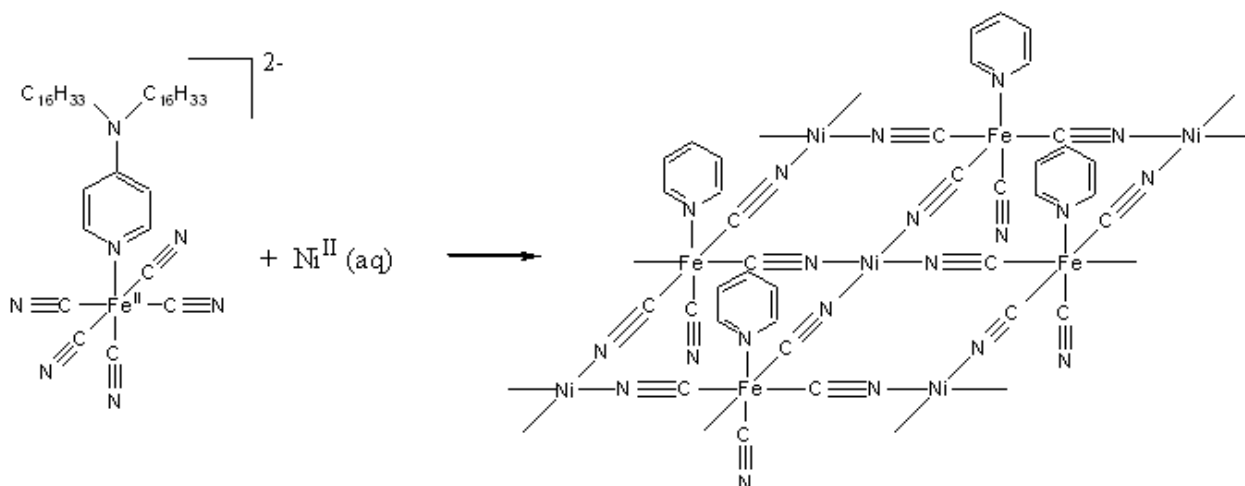


Figure 1-5. A face-centered square network created from an iron-containing amphiphile over an aqueous subphase containing Ni^{2+} ions. Alkyl tails on the amphiphiles are omitted for clarity.

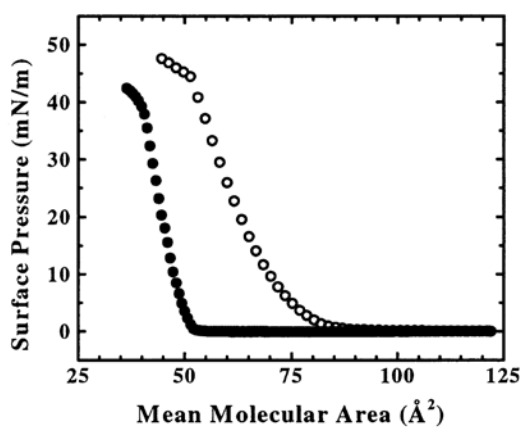


Figure 1-6. Surface pressure vs. mean molecular area isotherm of Culp's pentacyano amphiphile over a NaCl subphase (open circles) and Ni^{2+} subphase (filled circles).²¹

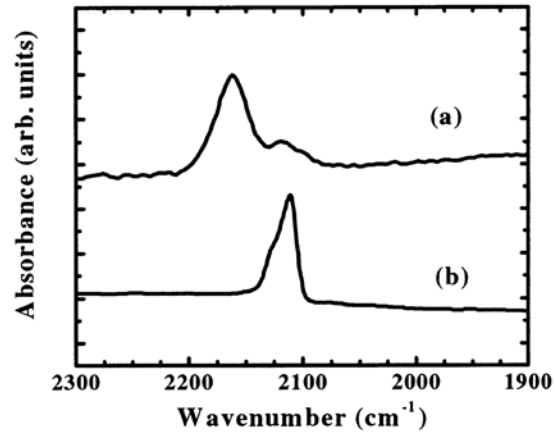


Figure 1-7. FT-IR spectra of the pentacyanoferrate amphiphile after spreading over a Ni²⁺ subphase (a) and in a KBr pellet (b).²¹

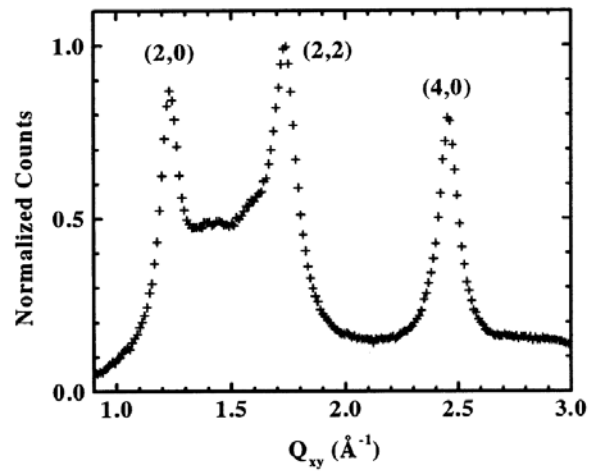


Figure 1-8. GXR D spectrum of a 30-bilayer sample of Culp's centered-square cyanometallate monolayer material.²¹

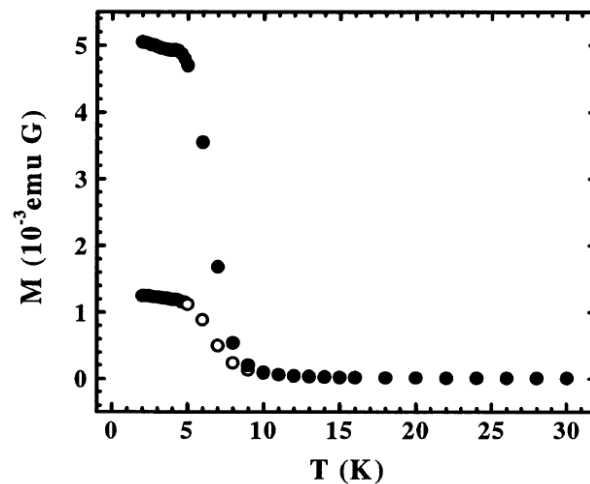


Figure 1-9. Field-cooled temperature-dependant magnetization of the centered-square film material taken at 20 G while the sample is aligned parallel to the applied field (filled circles) and perpendicular to the applied field (open circles).

CHAPTER 2 PRIMITIVE SQUARE NETWORKS AT THE AIR-WATER INTERFACE

Introduction

Although recent work by Culp et al.¹⁵⁻²² has demonstrated that the air/water interface can be used to direct the structure of cyanometallate networks by confining reactants to two dimensions, the centered-square geometry of the resulting networks was purely a property of the four-fold connectivity of the pentacyanoferrate amphiphile and the divalent transition metals to which they bonded. One of the most useful structure-directing elements at a synthetic chemist's disposal when designing supramolecular assemblies of transition metal complexes is the use of blocking ligands. By selectively blocking binding sites on transition metal-containing supramolecular building blocks, undesirable binding geometries can be eliminated and the material forced to adopt the desired geometry. In order to increase the usefulness of the interface as a structure-directing element in supramolecular chemistry, it is desirable to demonstrate that blocking ligands can be employed to control the geometry of the resulting films by directing the geometry of the underlying cyanometallate networks.

Although many fundamental three-dimensional geometries have been demonstrated in solid materials with extended structure created through the supramolecular assembly of transition metal complexes, to date only one fundamental geometry - the centered square - has been demonstrated in two-dimensional supramolecular materials with extended cyanometallate networks. The purpose of this work is to demonstrate that blocking ligands can be used in conjunction with the air/water interface to synthesize Langmuir monolayers with underlying cyanometallate networks of hexagonal and primitive square geometries (Figure 2-1).

There are two possible ways to combine a 4-coordinate center with a linear center to produce a networked Langmuir monolayer with a primitive square geometry. In the first approach, a 4-coordinate amphiphile is spread as a Langmuir monolayer over a subphase containing dissolved linearly-binding molecules. In the second approach, linearly-binding amphiphiles are spread as Langmuir monolayers over a subphase containing dissolved 4-coordinate molecules.

Our choice of 4-coordinate ligand is bis(tetramethylammonium) pentacyano(4-(didodecylamino)-pyridine) ferrate(III) (**1**), the amphiphile that has already proven useful for the creation of centered-square networks. Our 2-coordinate amphiphile will be 1-3-6-10-13 pentaazacyclotetradecane nickel (II) (**2**). **1** will be combined with an aqueous subphase of 1-4-8-11 tetraazacyclotetradecane nickel (II) (**3**) or Ru(II/III) tetracarboxylate chloride (**4**), both of which are two-coordinate linear binders (Figures 2-2 and 2-3).

Analogs of the expected two-dimensional networks have been reported in bulk materials (Figures 2-4 and 2-5).^{26,27} The ruthenium dimer **4** has been extensively used as a building block in the creation of extended cyanometallate structures,²⁷⁻³⁴ and cyclam and other equatorially-bound blocking ligands have been used to control the coordination geometry of cyanometallates.³⁵⁻⁴⁰ Amphiphile **2** will be combined with an aqueous subphase of $K_4Fe(CN)_6$ (Figure 2-6) to form a network analogous to Figure 2-4.

Experimental

Synthesis

Pentacyanoferrate amphiphile synthesis

The pentacyanoferrate amphiphile **1** was synthesized according to a previously-reported procedure.²¹ The synthesis involved three main steps, described in detail below; the alkylation of the iodide-protected aminopyridinium ligand; the deprotection of the alkylated ligand; and the attachment of the ligand to the aminopentacyanoferrate complex.

N-methyl-4-(didodecylamino)pyridinium iodide

A solution of 7.0 g of *N*-methyl-4-aminopyridinium iodide (30 mmol), 18.8 g of 1-bromodecane (85.0 mmol), and 20.0 g of Cs₂CO₃ (61.4 mmol) were combined in 150 ml of acetonitrile and refluxed for 48 hours under a nitrogen atmosphere. After cooling to room temperature the acetonitrile was removed under low pressure and the organic products dissolved in 20 ml of chloroform. The chloroform solution was filtered through a fritted funnel and 40 ml of ether added. The solution was chilled to 0 °C in an ice bath and 300 ml of pentane added, resulting in the precipitation of the *N*-methyl-4-(didodecylamino)pyridinium iodide product (15.2 g, 91.1%). The product was used without further purification for the next step.

4-(Didodecylamino)pyridine

Demethylation of the pyridinium iodide product from the previous step was accomplished by combining 15.0 grams (27.6 mmol) of *N*-methyl-4-(didodecylamino)pyridinium iodide with 40.0 grams (346 mmol) of pyridine hydrochloride. After rigorously purging the system with nitrogen, the mixture was heated until the pyridine hydrochloride melted and the *N*-methyl-4-(didodecylamino)pyridinium

iodide dissolved into it. After stirring for 24 hours the solution was cooled to room temperature and 150 ml of water was added to dissolve the remaining pyridine hydrochloride. The solid product was filtered off and dissolved in chloroform, which was then washed with aqueous ammonium hydroxide. The chloroform was dried with anhydrous MgSO_4 and then removed under reduced pressure. Acetonitrile (50 ml) was added and the solution was cooled to $0\text{ }^\circ\text{C}$ in an ice bath. The resulting solid precipitate was dissolved in 200 ml of ethyl ether and treated with 400 mg of activated carbon, after which it was filtered through a short Celite column. The filtrate was mixed with 160 ml of acetonitrile and left in the freezer overnight, resulting in a white precipitate. The solid material was collected by filtration and washed with cold acetonitrile (7.7 g, 68%). The product was used without further purification for the next step.

Bis(tetramethylammonium)pentacyano(4-(didodecylamino)-pyridine) ferrate(III)

1.9 g (4.5 mmol) of 4-(didodecylamino)pyridine and 0.40 g (1.5 mmol) of $\text{Na}_3[\text{Fe}(\text{CN})_5\text{NH}_3]$ were combined in 50 ml of methanol and heated to $40\text{ }^\circ\text{C}$. The solution was stirred for 12 hours with oxygen slowly bubbling through it. The resulting dark purple solution was concentrated to 10 ml under reduced pressure at room temperature and 40 ml of chloroform added to cause the precipitation of any remaining iron salts. The solution was filtered through a short Celite column and the solvents were removed under reduced pressure. Excess 4-(didodecylamino)pyridine was removed by dissolving the products in 50 ml of methanol and combining with an excess of AgBF_4 , causing the pentacyano(4-(didodecylamino)-pyridine) product to precipitate. The resulting solid was filtered off and washed with methanol. The silver cation was exchanged for the tetramethylammonium cation by dissolving the product in a methanol solution containing an excess of tetramethylammonium bromide, causing the

precipitation of AgBr. The mixture was stirred for 4 hours and the AgBr removed by vacuum filtration. The violet filtrate was reduced to a few ml under a stream of nitrogen at room temperature and combined with 25 ml of acetonitrile. Addition of 75 ml of acetone, followed by sitting for three days in the freezer resulted in the precipitation of the product, which was collected by vacuum filtration. (0.38 g, 32%) IR (KBr pellet, cm^{-1}): ν_{CN} 2116, 2060. CHN calculated for $\text{C}_{42}\text{H}_{90}\text{N}_9\text{O}_6\text{Fe}$: C, 57.78; H, 10.4; N, 14.44. Found: C, 56.80; H, 8.4; N, 13.3.

Ru(II/III)tetracarboxylate chloride

Ru(II/III)tetracarboxylate chloride was synthesized according to a published procedure.⁴¹ 1.16 g (5.59 mmol) of RuCl_3 and 1.86 g (43.9 mmol) of LiCl were added to a 65 ml acetic acid/15 ml acetic anhydride solution and refluxed under oxygen for 24 hours. After cooling to room temperature the resulting redish-brown crystals were washed with ethyl ether and cold ethanol, then dried under vacuum. (0.74 g, 38%) IR (KBr pellet, cm^{-1}): $\nu_{\text{CO}_2_{\text{asym}}}$ 1480, $\nu_{\text{CO}_2_{\text{sym}}}$ 1445. CHN calculated for $\text{C}_8\text{H}_{14}\text{Ru}_2\text{Cl}$: C, 20.28; H, 2.55; N, 0. Found: C, 20.3; H, 2.42; N, 0.

1,4,8,11-tetraazacyclotetradecane nickel (II) perchlorate

1,4,8,11-tetraazacyclotetradecane nickel (II) perchlorate was synthesized according to a published procedure, with slight modifications.⁴² 5.0 g (19 mmol) of $\text{Ni}(\text{ClO}_4)_2$ and 3.5 ml (20 mmol) of 1,5,8,12-tetraazadodecane were dissolved in 40 ml of deionized water. The solution was cooled to 5° C in an ice bath and 3 ml 40% glyoxal in water was added (20 mmol). The solution was stirred at room temperature for four hours, after which it was again cooled to 5° C in an ice bath and 1.0 g of sodium borohydride was slowly added. The solution was then heated to 90° C for 15 minutes and filtered while hot. A 2 ml portion of 70% perchloric acid was added to the filtrate,

causing crystallization of 1,4,8,11-tetraazacyclotetradecane nickel (II) perchlorate. The crystals were washed with small portions of cold ethanol and air dried. (3.94 g, 59.4%) IR (KBr pellet, cm^{-1}): ν_{NH} 3220, ν_{CH} 1560-800. C,H,N expected (found): C 25.8 (26.5), H 5.08 (5.28), N 11.9 (12.1).

1-octadecyl-1,3,6,10,13-pentaazacyclotetradecane nickel (II) chloride

1-octadecyl-1,3,6,10,13-pentaazacyclotetradecane nickel (II) chloride was synthesized according to a published procedure.⁴³ A solution of 1.4 g (5.9 mmol) NiCl_2 in 30 mL MeOH was added to a solution of 0.97g (6.1 mmol) N,N'-bis(2-aminoethyl)-1,3-propanediamine, 1.3g (5.4 mmol) 1-octadecylamine, and 1.3g (16 mmol) formaldehyde in 20 mL MeOH. The resulting solution was refluxed for 72 hours and filtered while hot. Upon cooling to room temperature violet crystals precipitated, which were filtered and washed with cold ethyl ether. (0.83 g, 13%) IR (KBr pellet, cm^{-1}): ν_{NH} 3275, 3262, 3205, ν_{CC} 1466, 1377. C,H,N for $\text{Ni}(\text{C}_{27}\text{H}_{60}\text{N}_5)\text{Cl}_2$: Expected (found): C 55.58 (55.78); H 10.19 (10.57) N 12.01 (11.81).

Materials

All materials were used as received from Sigma-Aldrich or Fisher-Acros or as synthesized above. Silicon wafers were purchased from Semiconductor Processing Company of Boston, MA and cleaned using the RCA cleaning procedure prior to use. Subphase solutions were prepared using 18 M Ω water from a Barnstead Nanopure filtration system.

Instrumentation

Langmuir monolayer experiments were performed using modified KSV 2000 and 5000 systems that had been adapted to use two barriers, coupled to homemade Teflon troughs. Surface pressure was monitored with a Wilhelmy balance made of filter paper

attached to a KSV microbalance. The troughs were enclosed in plastic containers to dampen motion in the surrounding air. Brewster angle microscopy experiments were performed using a Nanofilm Technology BAM2+ system with a 50 mW, 532 nm Nd:YAG laser and 572 x 768 pixel CCD camera with a 10x magnification objective. For all experiments the laser was kept at 50% power and CCD shutter time was set to 0.02 seconds. A slab of black glass was placed under the subphase to reduce reflected light from the trough's white Teflon surface. To dampen vibrations the BAM and trough were set atop an active isolation table that rested on a six-inch slab of granite supported by inflatable tire innertubes. ATR FT-IR spectra were taken with a Thermo Scientific Nicolet 6700 spectrometer and a Harrick TMP ATR stage. ATR experiments were performed on Si or Ge crystals measuring 50 mm x 10mm x 3mm. Si ATR crystals were cleaned using the RCA procedure prior to use, while Ge crystals were cleaned by boiling in ethanol and then hexane to remove debris. AFM experiments were performed with a Digital Instruments Nanoscope IIIa Multimode AFM. The AFM was suspended with bungee cords on a heavy concrete slab to dampen vibrations. Silicon AFM cantilever probes were obtained from Nanosensors of Phoenix, AZ.

Langmuir Monolayer Preparation

Langmuir monolayers of amphiphiles **1** and **2** were prepared by spreading chloroform solutions of the respective amphiphiles over an aqueous subphase containing dissolved counterions. The chloroform solutions were approximately 0.5 mg/ml concentration. Amphiphile **1**, which has four-fold binding symmetry, was spread over subphases containing 1 mM **3** and **4**, both of which have two-fold binding symmetry. Amphiphile **2**, which has two-fold binding symmetry, was spread over subphases containing 1 mM $\text{K}_4\text{Fe}(\text{CN})_6$, which has four-fold binding symmetry within the

plane of the monolayer. Because amphiphile **2** requires an aqueous subphase with a high ionic strength to spread properly, a solution of 0.5 M NaCl was used. All monolayers were allowed to equilibrate at high mean molecular areas for 15 minutes after spreading and were compressed with a barrier speed of 5 mm/min with a maximum pressure increase of 1 mN/min unless otherwise noted. The morphology and density of the monolayers were monitored with BAM throughout the experiments. Monolayers and multilayer films were transferred to substrates at 5 mm/min for analysis with AFM, XPS, and ATR FT-IR.

Results

Synthesis

Bis(tetramethylammonium)pentacyano(4-(didodecylamino)-pyridine) ferrate(III)

The pentacyanoferrate amphiphile **1** was difficult to synthesize, and satisfactory CHN results could not be obtained. A persistent problem was the presence of a CN stretching peak in the IR at 2060 cm^{-1} , indicative of the reduced ferrous form of the complex. Carrying out the synthesis with oxygen gas bubbling through the reaction mixture lessened, but did not eliminate, the amount of reduced material as indicated by IR.

Ru(II/III)tetracarboxylate chloride

The Ru(II/III) tetracarboxylate chloride dimer **4** was synthesized by refluxing RuCl_3 with glacial acetic acid in an acetic anhydride solvent. Bubbling oxygen through the reaction mixture was necessary to avoid the Ru (II/II) product.

1,4,8,11-tetraazacyclotetradecane nickel (II) perchlorate

The macrocyclic Ni complex 1,4,8,11-tetraazacyclotetradecane nickel (II) perchlorate was synthesized via a “template effect” technique in which the linear

tetraamine ligand chelates around the Ni^{II}, positioning the ends of the ligand in close proximity to each other so as to facilitate the formation of a macrocyclic complex. Once the added glyoxal has formed an imine with one end of the tetraamine ligand, it is far more likely to react with the other end of the same ligand than with a different tetraamine; this prevents polymerization.

1-octadecyl-1,3,6,10,13-pentaazacyclotetradecane nickel (II) chloride

1-octadecyl-1,3,6,10,13-pentaazacyclotetradecane nickel (II) chloride was synthesized in a templated manner similar to that used in the synthesis of the 1,4,8,11-tetraazacyclotetradecane ligand, but with the incorporation of an 18-carbon alkyl tail.

Macrocyclic Ni^{II} Amphiphile with K₄Fe(CN)₆ Subphase

Surface pressure vs. mean molecular area isotherms

When amphiphile **2** is spread over an aqueous subphase containing 0.5M NaCl it forms a well-behaved isotherm that begins to increase in surface pressure at approximately 80 Å² and collapses at approximately 60 Å² when compressed. This behavior is comparable to that reported for other 14-member macrocyclic amphiphiles of similar size.⁴⁴ When the monolayer is prepared over a subphase of equal ionic strength that contains ferrocyanide anions, the surface pressure begins to increase at approximately 100 Å², and the film collapses at 50 Å² (Figure 2-11).

BAM

BAM observations of amphiphile **2** over a 0.5M NaCl subphase show ordinary amphiphile behavior, with fluid regions at high mean molecular areas (Figure 2-12). Over a 0.42 M NaCl, 0.02M K₄Fe(CN)₆ subphase amphiphile **2** shows rigid condensed regions at high mean molecular areas. At 50 Å² the monolayer collapses along the boundaries of the rigid regions (Figure 2-13).

ATR FT-IR

Four monolayers of amphiphile **2** over a 0.02M $\text{K}_4\text{Fe}(\text{CN})_6$ subphase were transferred to a silicon ATR crystal and analyzed with FT-IR. (Figure 2-14) The resulting spectra showed a primary cyanide peak centered at 2087 cm^{-1} . (Figure 2-15) The CH_2 stretches were red-shifted and had a lower full-width-at-half-max when the monolayer was prepared over the $\text{K}_4\text{Fe}(\text{CN})_6$ subphase than when it was prepared over the NaCl subphase, indicating increased ordering of the alkyl tails in the film (Figure 2-16).

XPS

The XPS spectra of amphiphile **2** prepared over a $\text{K}_4\text{Fe}(\text{CN})_6$ subphase and transferred via a Langmuir-Blodgett dipping technique to a silicon substrate appears in Figure 2-17. Several elements are observed, including nickel and iron, consistent with the formation of the expected cyanometallate film. The relative abundances of nickel and iron were determined by multiplex scans, as seen in Figures 2-18 and 2-19. After adjusting for the relevant sensitivity factors, the relative abundance of Fe:Ni was found to be 1:2.

AFM

A single layer of the film was transferred onto an OTS-coated Si substrate for tapping mode AFM analysis. The thickness of the resulting film was approximately 3.5 nm, consistent with the expected thickness of the monolayer (Figure 2-20).

Creep observations

The mean molecular area of the network was monitored over time at a constant surface pressure of 1mN/m. The decrease was initially non-linear, but became linear after approximately 100 minutes. The linear component of the creep was approximately 0.1 \AA^2 per minute and is believed to be caused by the monolayer dissolving off the

water's surface. The non-linear portion of the creep is believed to reflect the change in mean molecular area as the monolayer anneals and packs more efficiently on the surface (Figure 2-21).

BAM observations taken over time as the monolayer is held at 1 mN/m show an apparent annealing of the rigid regions. The regions of exposed water gradually disappear over approximately 100 minutes, after which the monolayer appears continuous (Figure 2-22).

The collapse behavior of the monolayer is distinctly different after it is allowed to anneal for 100 minutes. When the monolayer is compressed continuously at 5 mm/min, the monolayer collapses along the boundaries of the rigid islands. After allowing the monolayer to equilibrate at 1 mN/m for 100 minutes, the monolayer displays more traditional collapse behavior, with long collapse lines that span the BAM viewing area (Figure 2-23).

Pentacyanoferrate Amphiphile with Macrocyclic Tetraaza Ni (II) Subphase

Surface pressure vs. mean molecular area isotherms

When amphiphile **1** is spread over an aqueous subphase containing 10 mM NaCl it forms a well-behaved isotherm that begins to increase in surface pressure at approximately 85 \AA^2 and collapses at approximately 50 \AA^2 when compressed. When the monolayer is prepared over a subphase of equal ionic strength that contains dissolved 1-4-8-11 tetraazacyclotetradecane nickel (II) perchlorate, the surface pressure began increasing at approximately 90 \AA^2 and collapses at approximately 70 \AA^2 when compressed (Figure 2-24). This is less than anticipated from the expected primitive square geometry (approximately 100 \AA^2).

BAM

BAM observations of amphiphile **1** over a 10 mM NaCl subphase show ordinary amphiphile behavior, with fluid regions at high mean molecular areas. When the monolayer was prepared over a macrocyclic tetraaza Ni(II) subphase, the film shows rigid condensed regions at high mean molecular areas. (Figure 2-25)

The rigid, condensed islands of the monolayer that appear at high mean molecular areas over the ferrocyanide subphase are consistent with the formation of an extended coordination network due to the binding of the amphiphile's nitrile groups to the nickel complexes in the subphase.

XPS

The XPS spectra of amphiphile **1** prepared over a tetraaza macrocyclic Ni(II) subphase and transferred via a Langmuir-Blodgett dipping technique to a silicon substrate appears in Figure 2-26. Several elements are observed, including nickel and iron, consistent with the formation of the expected cyanometallate film. The relative abundances of nickel and iron were determined by multiplex scans, as seen in Figures 2-27 and 2-28. After adjusting for the relevant sensitivity factors, the relative abundance of Fe:Ni was found to be 1:1.

Pentacyanoferrate Amphiphile with Ru (II/III) Tetracarboxylate Subphase

Surface pressure vs. mean molecular area isotherms

When the monolayer is prepared over a subphase of 1 mM Ru (II/III) tetracarboxylate dimer, the mean molecular area at which the film's surface pressure begins to rise over time. After 16 hours, the system forms a film that begins to increase in surface pressure at approximately 200 \AA^2 and collapses at 120 \AA^2 (Figure 2-29).

BAM

When amphiphile **1** is initially spread over an aqueous subphase of the Ru dimer **4**, it forms a monolayer that appears fluid under BAM observation. After four hours of allowing **1** to react on the surface, the film displays rigid, condensed regions consistent with the presence of an underlying cyanometallate network (Figure 2-30).

ATR FT-IR

Three layers of amphiphile **1** over a 1 mM Ru(II/III)Cl / 1 mM NaCl subphase were transferred to a germanium ATR crystal (Figure 2-31). The resulting spectra showed a primary C-N stretching frequency of 2080 wavenumbers, with a smaller shoulder peak at 2130. (Figure 2-32) Examination of the carboxylate stretching frequencies at 1445 cm^{-1} and 1480 cm^{-1} indicates that the carboxylates have maintained their paddle-wheel configuration (Figure 2-33).⁴⁵

The CH_2 region of the film transferred over the ruthenium dimer subphase displayed a symmetric CH_2 stretch with a full-width-at-half-height of 29.5 cm^{-1} at 2994 cm^{-1} , the disordered limit for an alkane CH_2 stretch (Figure 2-34).

XPS

A single monolayer of amphiphile **1** over a subphase of 1mM NaCl and 1mM Ru dimer **4** was transferred to a silicon wafer for XPS analysis. The resulting spectra confirmed the presence of iron and ruthenium in the film (Figure 2-35). Analysis of the iron 2p₃ (Figure 2-36) and ruthenium 3p₃ (Figure 2-37) peak areas and adjustment for sensitivity factors indicated that iron and ruthenium were present in a roughly 1:4 relative abundance.

Discussion

Macrocyclic Ni^{II} Amphiphile with K₄Fe(CN)₆ Subphase

The appearance of condensed, rigid regions of film at high mean molecular areas when amphiphile **1** is prepared with a K₄Fe(CN)₆ subphase as observed by BAM is consistent with the formation of an extended cyanometallate network beneath the Langmuir monolayer. BAM observations of the monolayer during compression over a ferrocyanide subphase reveal that there are still substantial areas of bare water at the onset of surface pressure increase, indicating that the monolayer is not efficiently filling all available surface area. It appears that the surface pressure begins to increase when rigid islands of monolayer begin to bump against each other and are unable to efficiently pack on the surface. Over a NaCl subphase the monolayer behaves fluidly, and these rigid islands are not observed.

The rigid, condensed islands of monolayer that appear at high mean molecular areas over the ferrocyanide subphase are consistent with the formation of an extended coordination network due to the binding of the ferrocyanide nitriles to the nickel ions in the amphiphiles. It is significant that the rigid monolayer collapses at 50 Å², rather than 60 Å² as seen with pure NaCl, as 50 Å² closely matches the area of an amphiphile in the expected primitive square network. The tendency of the rigid, condensed film regions to merge over time, combined with the change in collapse behavior after the merging of the rigid regions under pressure, is indicative of an annealing process taking place between the film regions.

The relative 2:1 abundances of Ni:Fe as indicated by XPS are also consistent with the Ni:Fe ratios of the expected primitive square geometry.

ATR FT-IR analysis confirms the presence of Fe^{II}-CN-Ni^{II} bonds in the resulting film, as evidenced by the peak at 2087 cm⁻¹. This stretching frequency is consistent with reported Fe^{II}-CN-Ni^{II} cyanide stretching values²⁶. The CH₂ peak's red-shift and decrease in width when the film is prepared over a K₄Fe(CN)₆ subphase is indicative of a higher degree of order among the amphiphiles' alkyl tails, which is consistent with the ordering of the amphiphiles by an underlying cyanometallate network.

Pentacyanoferrate Amphiphile with Macrocyclic Tetraaza Ni (II) Subphase

The appearance of rigid, condensed regions of film at high mean molecular area with amphiphile **1** is spread over an aqueous subphase containing the macrocyclic tetraaza nickel complex is consistent with the formation of an underlying coordinate-covalent network.

The mean molecular area at which the film's surface pressure begins to rise increases to 90 Å² over the macrocyclic tetraaza nickel subphase versus 80 Å² over a non-coordinating NaCl subphase, and the area at collapse increases to 70 Å² versus 60 Å² for an NaCl subphase. Although these increases are substantial, they are less than would be predicted by the expected primitive square geometry, which would have a mean amphiphile area of approximately 100 Å². The surface pressure versus mean molecular area isotherms thus indicate that although some type of cyanometallate network is probably forming, it is not producing the expected primitive-square geometry.

A failure to form the expected primitive square network is further borne out by the relative 1:1 Fe:Ni abundances as indicated by XPS, rather than the expected 1:2 abundance that would occur in a primitive square network. It is interesting to note that a 1:1 Fe:Ni ratio would result in a charge-balanced film, as each pentacyanoferrate amphiphile has a charge of 2⁻ and each nickel complex has a charge of 2⁺.

Pentacyanoferrate Amphiphile with Ru (II/III) Tetracarboxylate Subphase

The substantial increase in the area at which pressure begins to rise in the surface pressure versus mean molecular area isotherms of the pentacyanoferrate amphiphile over a subphase of Ru (II/III) tetracarboxylate dimer indicates that the underlying coordination network has a high mean area per amphiphile. This is consistent with the relatively large unit cell length of 13 \AA^2 in the expected primitive square network. Precipitation of bulk solid material when the Ru carboxylate dimer is mixed with cyanometallates in solution is relatively slow. This slow bulk precipitation process is born out by the analogous two-dimensional film, which increases in mean molecular area on the timescale of hours.

The effects of the increase in distance between amphiphiles in the resulting film is visible in the film's FT-IR spectrum, where the CH_2 stretching peaks are blue-shifted and broadened to the disordered limit. The appearance of a CN stretching peak at 2080 cm^{-1} is problematic, as this is lower in energy than the free cyanide in the ligand (2110 cm^{-1}). It is thus likely that the Fe^{III} centers in the pentacyanoferrate have been reduced during the formation of the film's network, resulting in $\text{Fe}^{\text{II}}\text{-CN-Ru}^{\text{III}}$ bonds.

The relative Fe:Ru abundances of 1:4 as indicated by XPS is consistent with the Fe:Ru ratios in the expected primitive square network.

General Discussion

Although each of the systems examined displayed evidence of network formation, only the macrocyclic Ni^{2+} amphiphile, **2**, spread on a ferrocyanide subphase (Figure 2-6) and the pentacyanoferrate amphiphile, **1**, spread over a ruthenium carboxylate dimer (Figure 2-3) presented a relative abundance of component metals and surface pressure vs. mean molecular area isotherm consistent with the expected primitive-square

cyanometallate network. Although the pentacyanoferrate amphiphile's mean molecular area vs. surface pressure isotherms showed substantial changes when the monolayer was prepared over a subphase of nickel cyclam, the mean molecular area at collapse was always substantially lower than predicted by the desired network geometry.

The failure of the pentacyanoferrate/nickel cyclam system to achieve the desired network geometry is likely due to charge balancing problems. It is likely that any ordered two-dimensional cyanometallate network to form at the air/water interface would need to be charge balanced, since a two-dimensional film lacks the interstitial lattice sites that a three-dimensional structure could use to incorporate counter ions. The pentacyanoferrate amphiphile has a charge of 2^- , and therefore requires a linearly-binding subphase component with a charge of 1^+ to achieve charge balance within the network. Charge balance thus becomes an important consideration when designing such two-dimensional supramolecular films. The ruthenium carboxylate dimer, with which the pentacyanoferrate amphiphile does achieve mean molecular areas consistent with the expected underlying cyanometallate network, has the appropriate 1^+ charge (Figure 2-3). Similarly, the ferrocyanide subphase component's charge of 4^- is appropriate for combining with the 2^+ charge of the macrocyclic nickel amphiphile (Figure 2-6).

Since the surface pressure vs. mean molecular area isotherms and constituent metal ratios for the film prepared by spreading the pentacyanoferrate amphiphile over the nickel cyclam subphase indicate that the desired primitive square network isn't forming, it is interesting to consider what geometries that film's network might be adopting. One possibility that would be consistent with charge balance is the formation

of linear chains of amphiphile and subphase component. It is also possible that the film is forming a disordered but charge-balanced structure. A final possibility would be the formation of isolated amphiphile + nickel cyclam dimers.

It is interesting to note that the surface pressure vs. mean molecular area isotherms of the films created in this work behaved somewhat differently upon network formation than those created by Culp et al.²¹ Culp observed that the surface pressure began to increase at a mean area close to the expected mean area per amphiphile in the underlying cyanometallate networks, and then increased very rapidly upon compression. Since the mean area per amphiphile in Culp's networked films was smaller than the mean molecular area at which surface pressure began to increase in the non-networked films prepared over sodium chloride, the implication is that the formation of the cyanometallate network condenses the amphiphiles in the monolayer as they are locked into their lattice positions. The rapid increase in surface pressure upon compression of Culp's films is consistent with the formation of a cyanometallate network, which would be relatively noncompressible.

Unlike Culp's systems, the film prepared by spreading the macrocyclic nickel amphiphile over a ferrocyanide-containing subphase began increasing in surface pressure at a higher area than observed when the monolayer is prepared over a sodium chloride subphase. BAM observations revealed that this was due to discrete regions of rigid networked material that did not fit together properly.

Conclusions and Future Work

Three monolayer systems, each consisting of one connector with two-fold binding symmetry and one connector of four-fold binding symmetry, were combined to create two-dimensional primitive square networks at the air-water interface. In the first two

systems, the four-fold component was a pentacyanoferrate amphiphile that was combined with a subphase component of two-fold binding symmetry, nickel cyclam or ruthenium carboxylate dimer. In the third system, the four-fold component was subphase ferrocyanide and the two-fold component was a macrocyclic nickel-containing amphiphile.

Characterization of the systems with various techniques revealed that they form rigid, condensed films at the air-water interface due to the formation of an underlying cyanometallate network. In two of the films, the mean molecular area vs. surface pressure isotherms and metal ratios were consistent with the formation of the desired primitive square network.

Although the analysis described herein provides substantial evidence that a primitive square network is probably forming, it does not conclusively prove it. In order to prove the exact network geometry it would be necessary to use a characterization technique such as GXRD or X-ray absorption fine structure analysis. Unfortunately due to the extremely thin nature of the films and relatively large unit cells in the networks, an extremely intense X-ray source such as a synchrotron source would be necessary. Even with a synchrotron source, it is unclear whether or not the unit cells would be too large for successful GXRD characterization of the networks.

It was discovered that charge balancing is an important consideration in the creation of such networks, as two-dimensional networks lack interstitial lattice sites commonly used in bulk materials for incorporation of counterions. This is an important limitation that must be kept in mind when designing similar future two-dimensional film architectures, as it has a major impact on how useful various bridging or blocking

ligands can be. Unless all of the discrete amphiphilic and subphase components involved in the network formation are neutral, the bridging ligands will likely need to be of the appropriate charge to make the network's net charge neutral. Carboxylate ligands are one attractive possibility, as they can balance charge and are amenable to aqueous coordination chemistry. Anionic equatorial blocking ligands such as salens are also an interesting possibility for achieving charge balance in future networks, as they are water-stable and can be used as blocking ligands on a wide variety of transition metals.

As discussed previously, it was demonstrated by Culp et. al that such cyanometallate films can serve as templates for the buildup of three-dimensional cyanometallate networks.¹⁹ It would be interesting to investigate whether the primitive-square systems described herein could serve a similar role as templates for the creation of three-dimensional primitive cubic networks of analogous material. Such an experiment could be performed by depositing a monolayer of the primitive-square cyanometallate material onto a substrate via a Langmuir-Blodgett dipping technique, followed by sequential dipping into alternating solutions containing different network components. Alternatively, a flow-cell technique could be used in which alternating solutions of the network's respective components are flowed over the templating layer. This sort of flow-cell technique would have the advantage of allowing the material's buildup to be monitored with ellipsometry or ATR FT-IR. The resulting thin films would likely be far easier to characterize with GXR, as the material would be thicker.

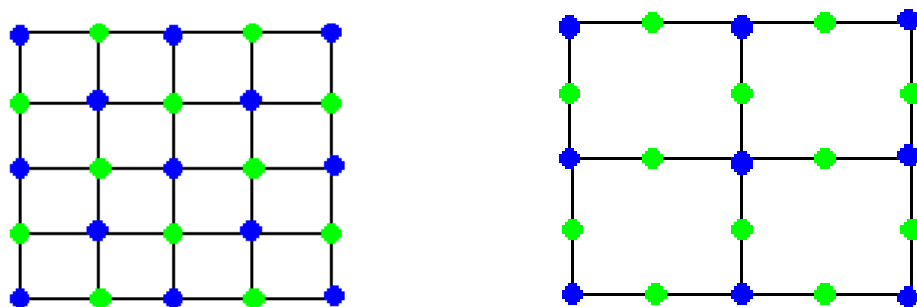


Figure 2-1. A centered square two-dimensional network formed by two four-coordinate components (left) and a primitive square two-dimensional network formed by one four-coordinate component and one two-coordinate component (right).

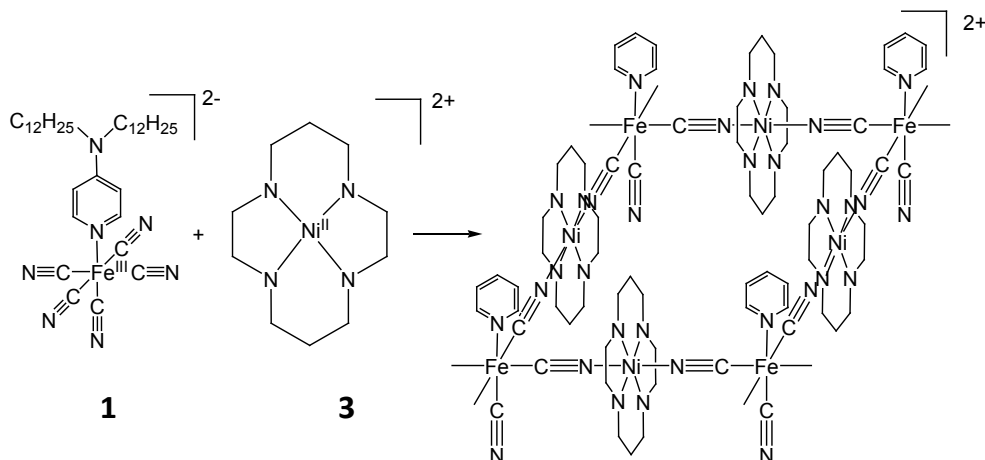


Figure 2-2. The geometry of the expected film produced by reacting a Langmuir monolayer of amphiphile 1 with subphase component 3. Alkyl tails are omitted to the right for clarity.

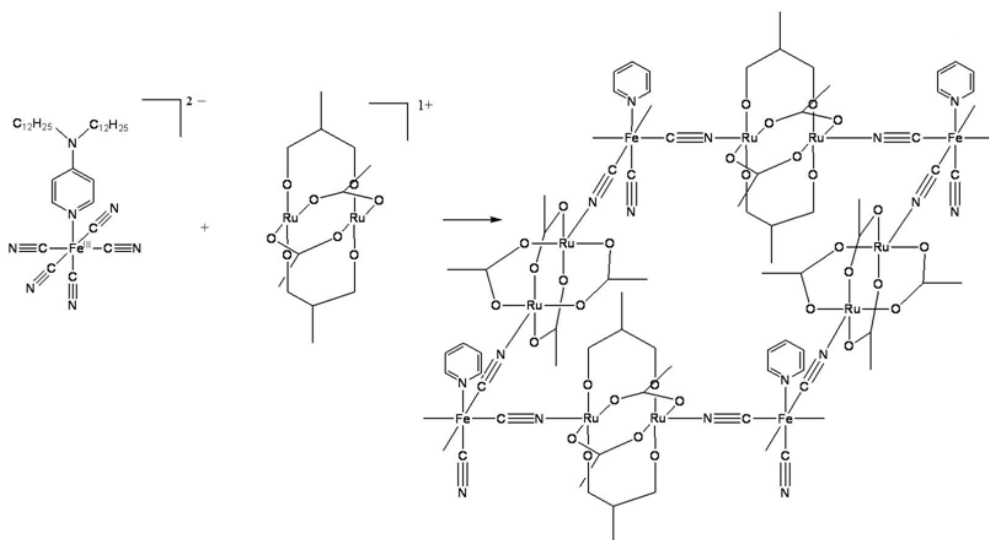


Figure 2-3. The geometry of the expected film produced by reacting a Langmuir monolayer of amphiphile **1** with subphase component **4**. Alkyl tails are omitted to the left for clarity.

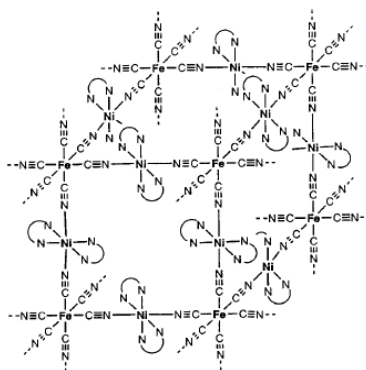


Figure 2-4. A bulk primitive-cubic cyanometallate material with an analogous structure to the network in Figure 2-2 and 2-6.²⁶

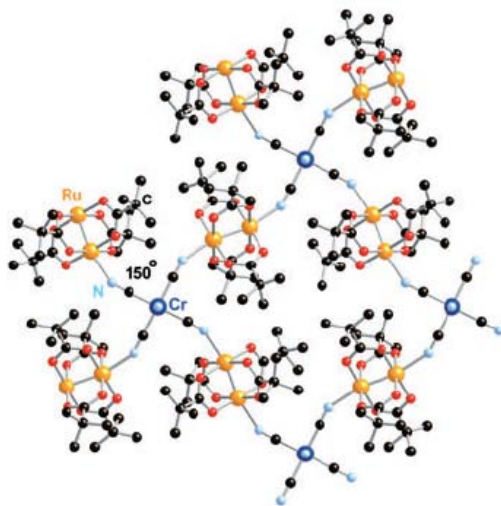


Figure 2-5. A bulk ruthenium dimer/cyanometallate material with a structure analogous to the monolayer network in Figure 2-3.²⁷

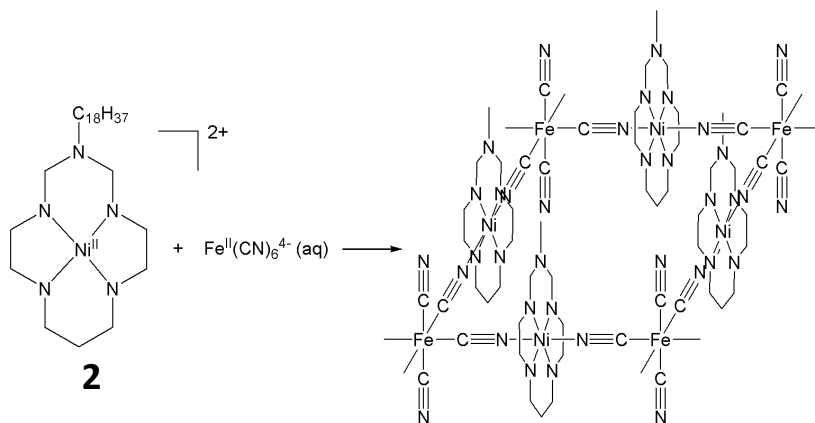


Figure 2-6. The geometry of the expected film produced by reacting a Langmuir monolayer of amphiphile 2 with $\text{Fe}(\text{CN})_6^{4-}$ in the subphase.

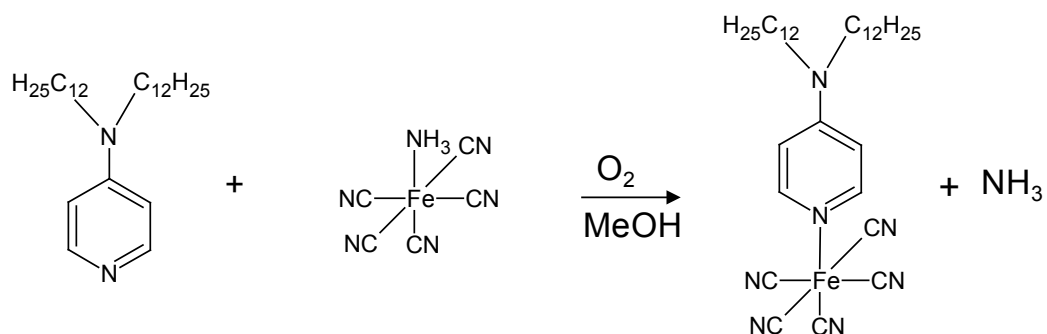


Figure 2-7. Synthesis of bis(tetramethylammonium)pentacyano(4-(didodecylamino)pyridine) ferrate(III).

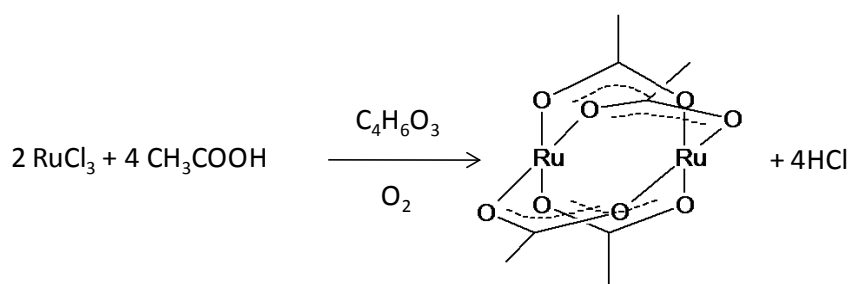


Figure 2-8 Synthesis of Ru (II/III) tetracarboxylate chloride.

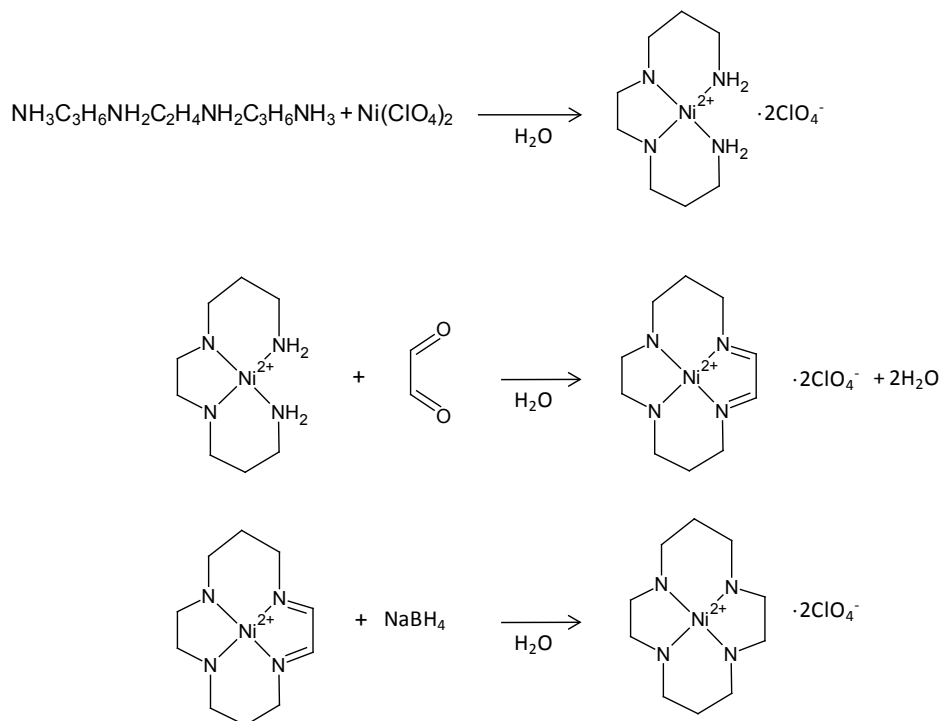


Figure 2-9. Synthesis of 1,4,8,11-tetraazacyclotetradecane nickel (II) perchlorate.

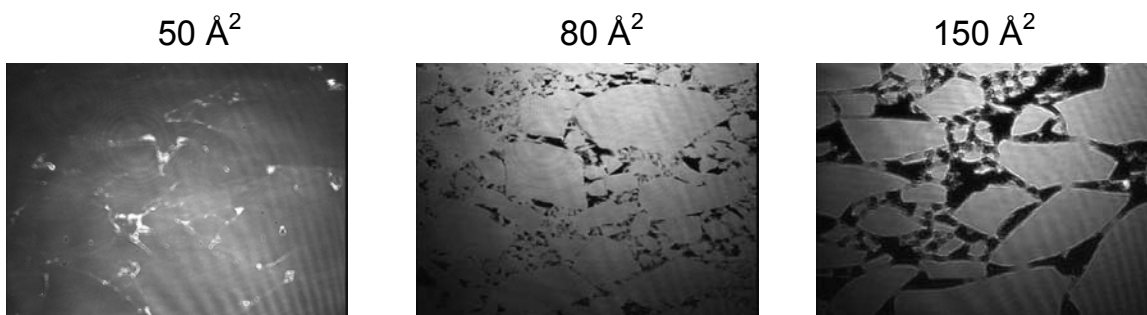


Figure 2-13. BAM images of macrocyclic Ni^{2+} amphiphile at various mean molecular areas over a 0.42 M NaCl/0.02M $\text{K}_4\text{Fe}(\text{CN})_6$ subphase.

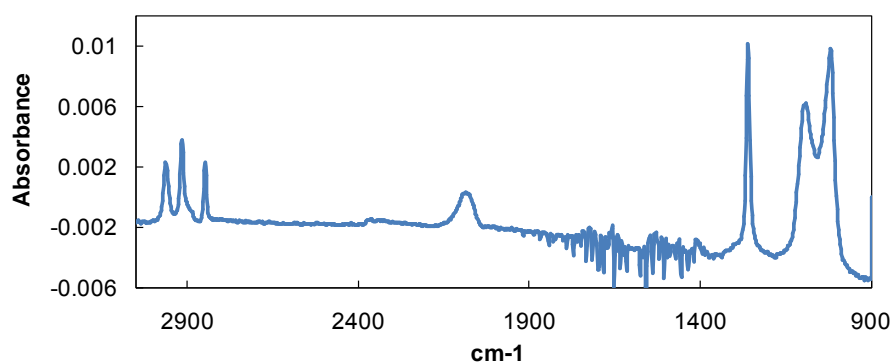


Figure 2-14. ATR FT-IR spectra of four layers of amphiphile **2** over a 0.42 M NaCl/0.02M $\text{K}_4\text{Fe}(\text{CN})_6$ subphase.

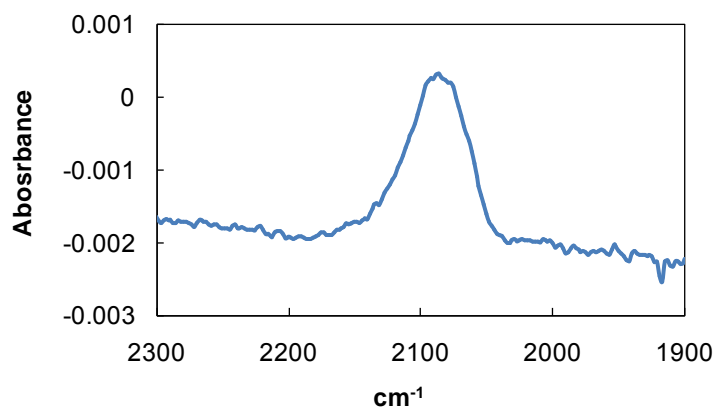


Figure 2-15. The cyanide stretching region of ATR FT-IR spectra of four layers of amphiphile **2** over a 0.42 M NaCl/0.02M $\text{K}_4\text{Fe}(\text{CN})_6$ subphase.

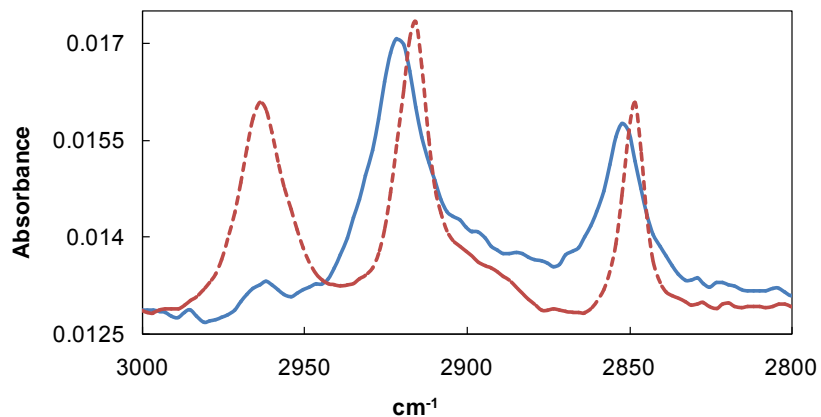


Figure 2-16. The CH₂ stretching region of ATR FT-IR spectra of four layers of amphiphile **2** over a 0.42 M NaCl/0.02M K₄Fe(CN)₆ subphase (dashed) and 0.5 M NaCl subphase (solid).

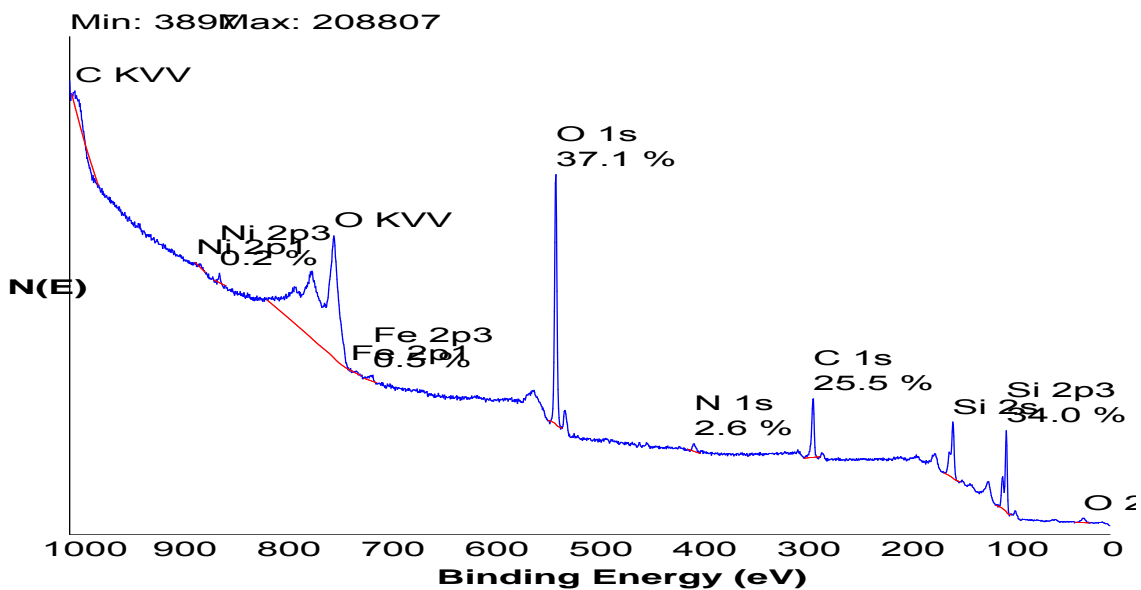


Figure 2-17. An XPS survey scan of amphiphile **2** over a subphase of K₄Fe(CN)₆ after transfer to a Si substrate.

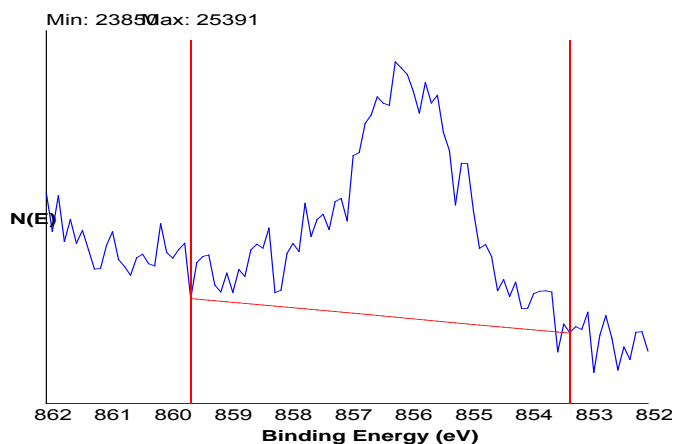


Figure 2-18. An XPS multiplex scan of the Ni 2p_{3/2} peak region of amphiphile **2** over a subphase of K₄Fe(CN)₆ after transfer to a Si substrate.

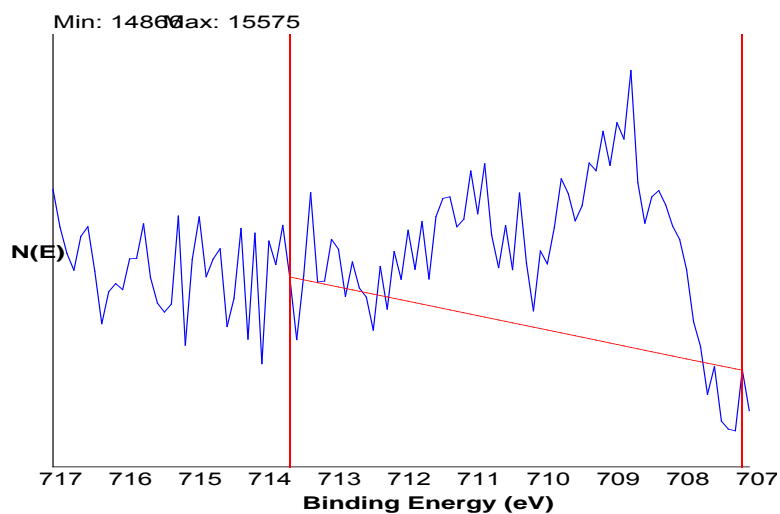


Figure 2-19. An XPS multiplex scan of the Fe 2p_{3/2} peak region of amphiphile **2** over a subphase of K₄Fe(CN)₆ after transfer to a Si substrate.

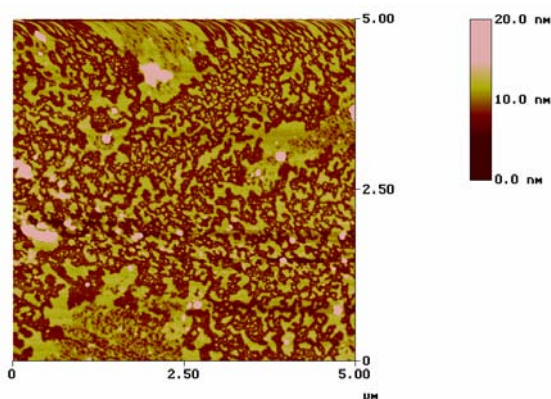


Figure 2-20. Tapping mode AFM of a monolayer of amphiphile **2** prepared over a ferrocyanide subphase after transfer to an OTS-coated Si substrate.

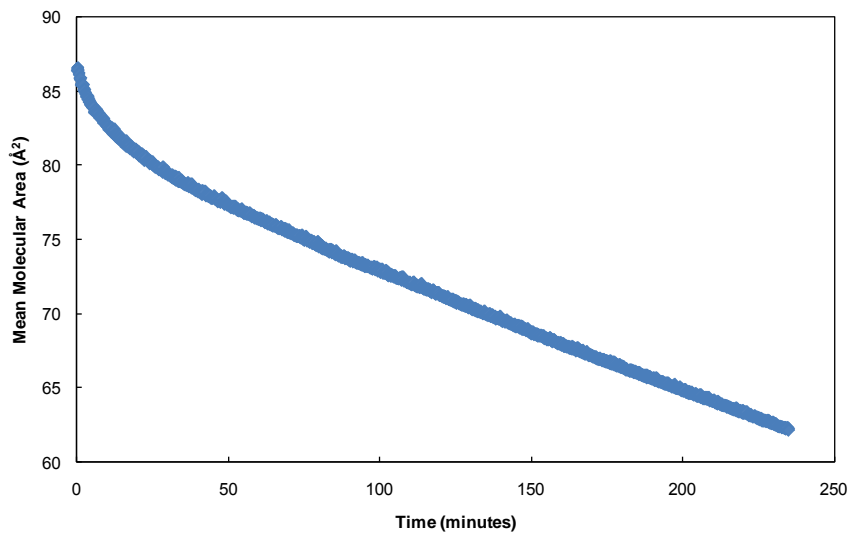


Figure 2-21. Mean molecular area vs. time of a monolayer of amphiphile **2** over a 0.42 M NaCl/0.02M $K_4Fe(CN)_6$ subphase held at a constant surface pressure of 1 mN/m.

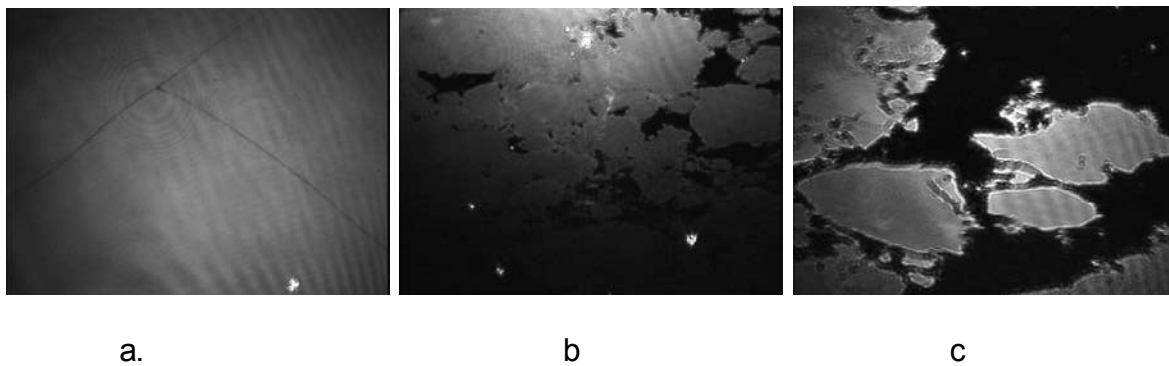


Figure 2-22. Rigid islands of macrocyclic Ni^{2+} amphiphile over a ferrocyanide subphase held at 1 mN/m. a) time=0 minutes. b) time=60 minutes. c) t=100 minutes.

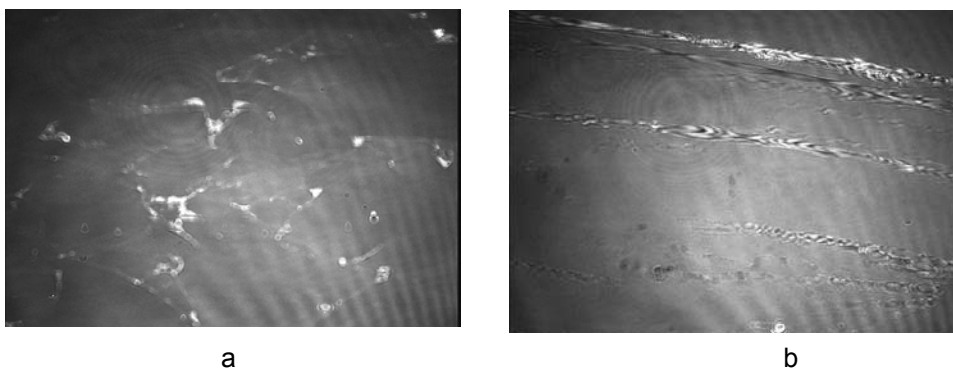


Figure 2-23. Collapse of macrocyclic Ni²⁺ amphiphile over ferrocyanide at 50 Å². a) With continuous compression. b) After equilibrating at 1 mN/m for 100 minutes

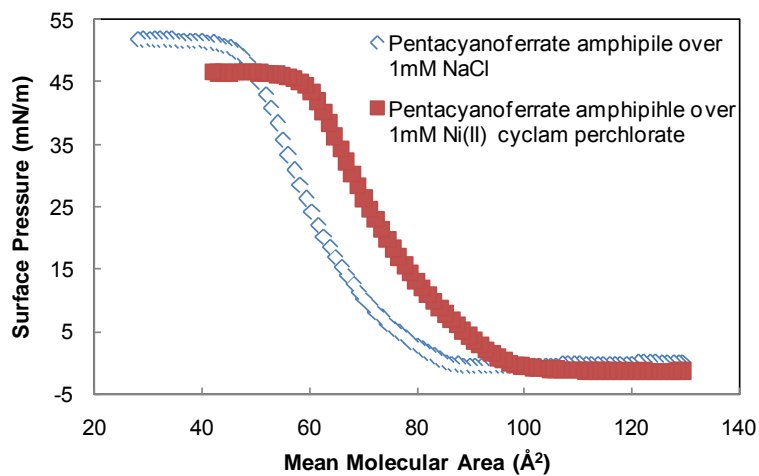


Figure 2-24. Isotherm of pentacyanoferrate amphiphile **1** over a 1mM NaCl subphase (open) and 1mM Ni(II)cyclam subphase (solid).

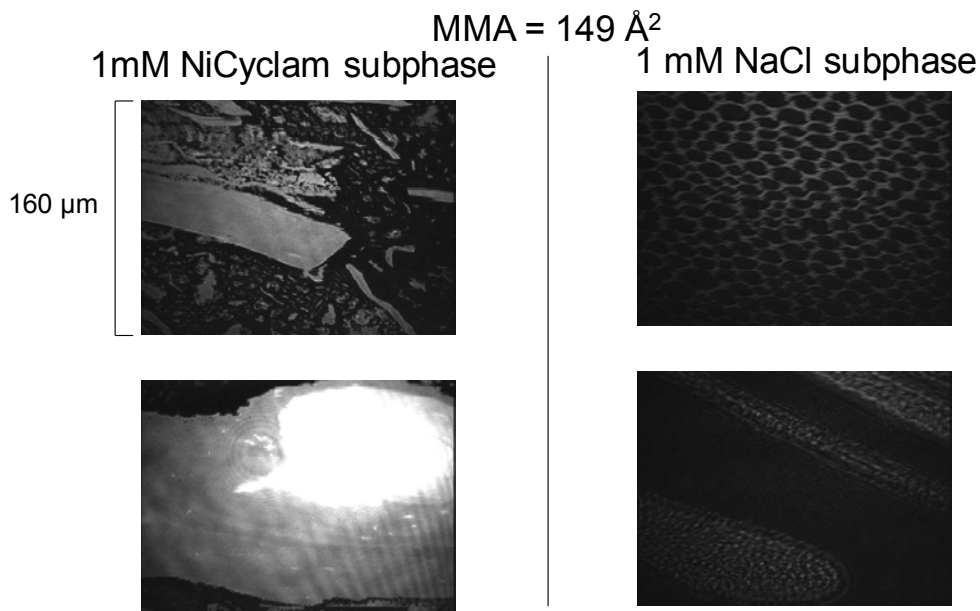


Figure 2-25. BAM observations of the pentacyanoferrate amphiphile **1** over 1 mM Ni(II)cyclam (left) and 1 mM NaCl (right)

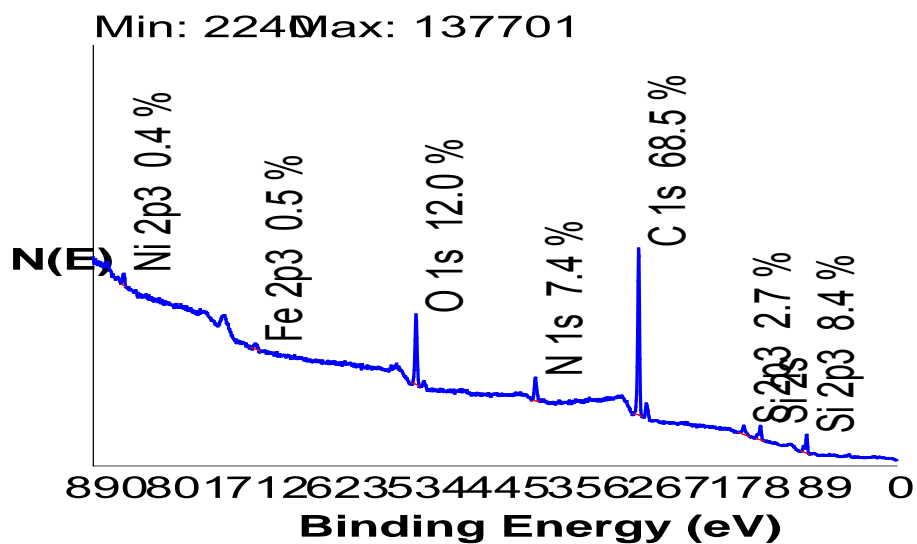


Figure 2-26. XPS scan of the pentacyanoferrate amphiphile **1** over a Ni(II) cyclam subphase after transfer to an Si substrate.

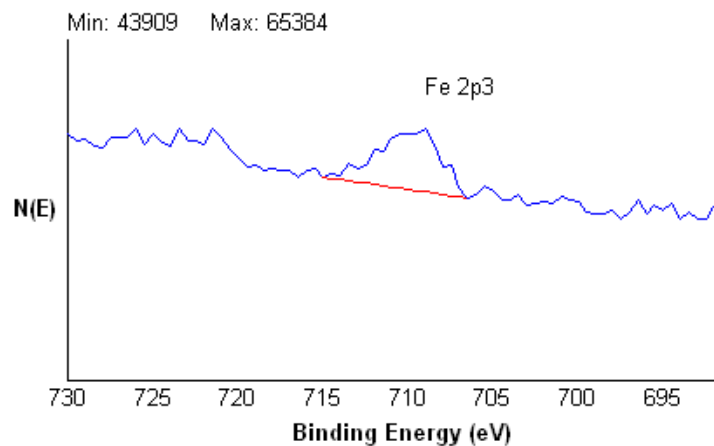


Figure 2-27. Multiplex XPS scan of the Fe region of the pentacyanoferrate amphiphile **1** over a Ni(II) cyclam subphase after transfer to a Si substrate.

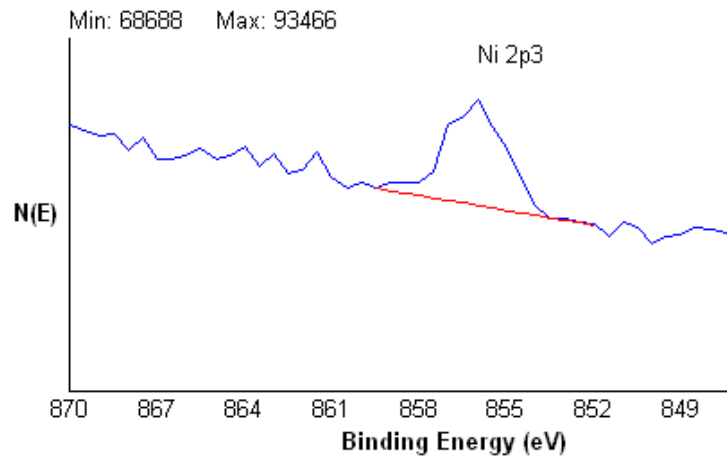


Figure 2-28. Multiplex XPS scan of the Fe region of the pentacyanoferrate amphiphile **1** over a Ni(II) cyclam subphase after transfer to a Si substrate.

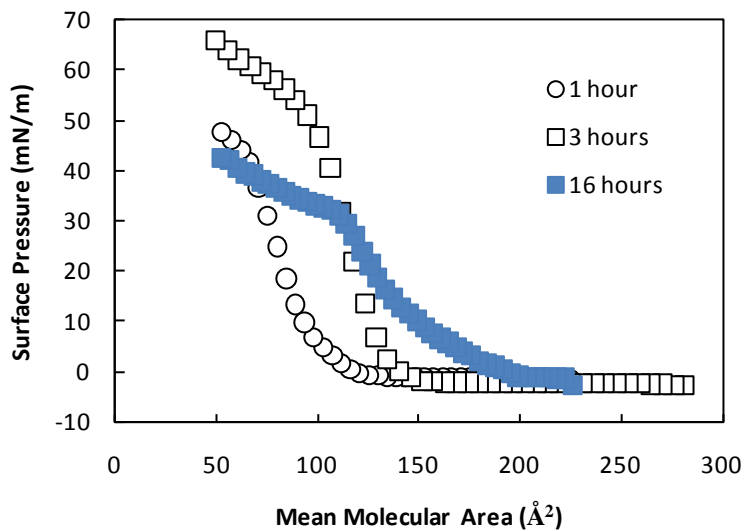


Figure 2-29. Surface pressure vs. mean molecular area isotherms of amphiphile 2 over a Ru(II/III) dimer subphase after 1, 3, and 16 hours.

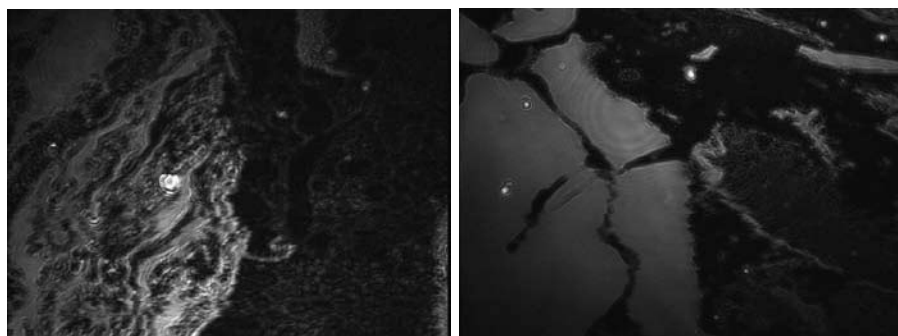


Figure 2-30. BAM images of amphiphile 1 over a 1 mM Ru(II/III)Cl / 1mM NaCl subphase immediately after spreading (left) and after four hours (right) at 200\AA^2 .

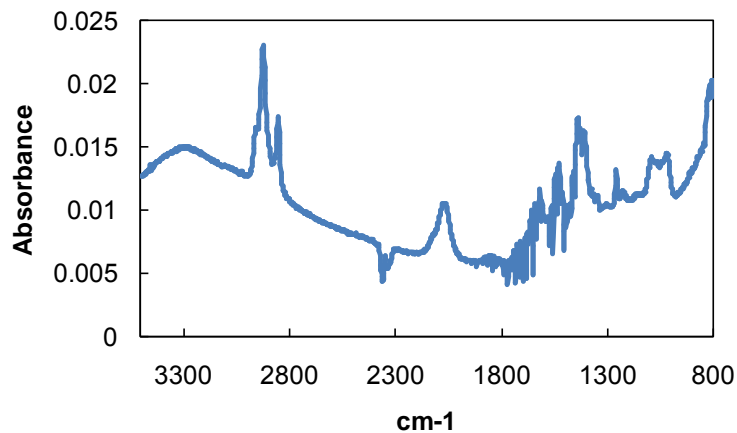


Figure 2-31. ATR FT-IR spectrum of the pentacyanoferrate amphiphile **1** over the Ru(II/III) carboxylate dimer **4**.

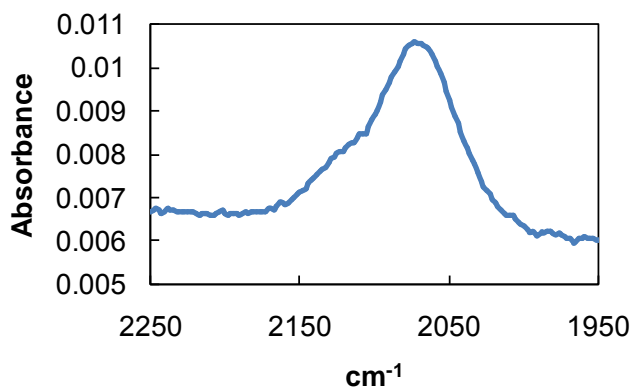


Figure 2-32. Cyanide stretching region of the ATR FT-IR spectrum of the pentacyanoferrate amphiphile **1** over the Ru(II/III) carboxylate dimer **4**.

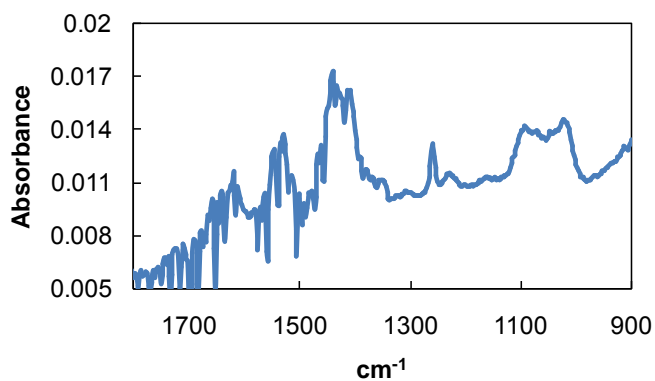


Figure 2-33. Carboxylate stretching region of the ATR FT-IR spectrum of the pentacyanoferrate amphiphile **1** over the Ru(II/III) carboxylate dimer **4**.

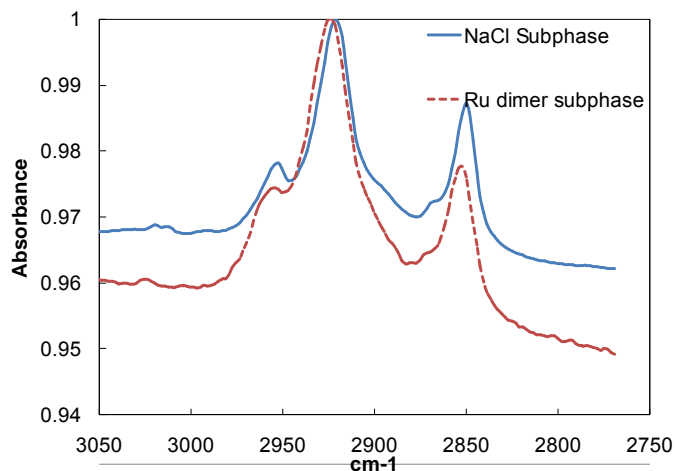


Figure 2-34. CH₂ stretching region of the ATR FT-IR spectrum of the pentacyanoferrate amphiphile **1** over the Ru(II/III) carboxylate dimer **4**.

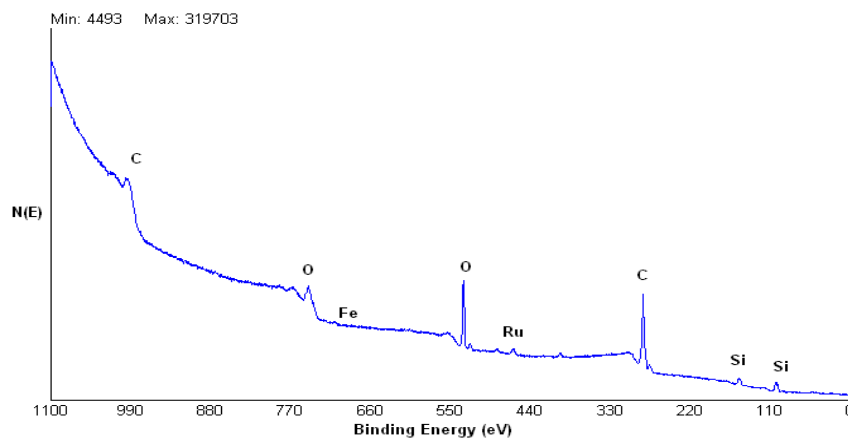


Figure 2-35. A survey scan of a monolayer of amphiphile **1** over a subphase of ruthenium carboxylate dimer.

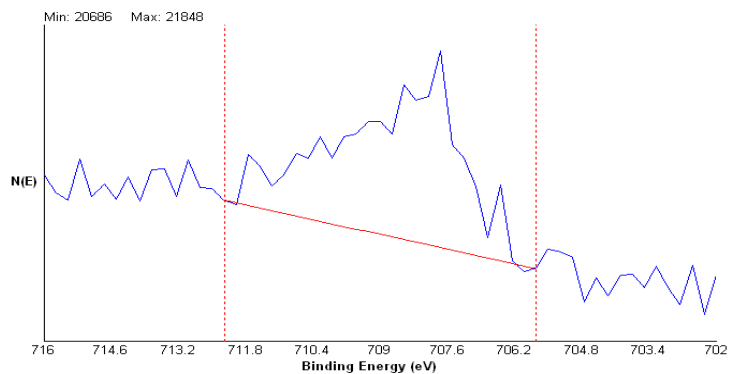


Figure 2-36. The iron 2p₃ XPS peak region of a monolayer of amphiphile **1** over a subphase of ruthenium carboxylate dimer.

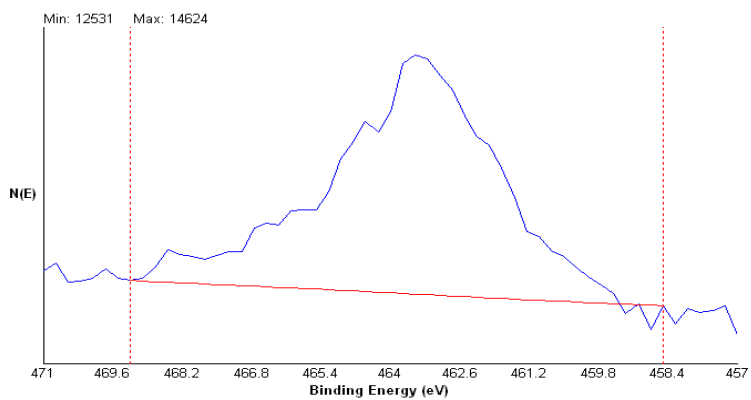


Figure 2-37. The ruthenium 3p3 XPS peak region of a monolayer of amphiphile **1** over a subphase of ruthenium carboxylate dimer.

CHAPTER 3 CYANOMETALLATE OLIGOMERS AS BUILDING UNITS IN SUPRAMOLECULAR BUILDING BLOCKS AT THE AIR/WATER INTERFACE

Introduction

As cyanometallate complexes have increased in popularity as supramolecular building blocks and served as components in supramolecular materials with a wide range of optical, magnetic, and electronic properties, interest has developed in creating larger and more elaborate cyanometallate structures.⁴⁶⁻⁴⁸ Unfortunately most demonstrated supramolecular structures created with cyanometallate subunits utilize only relatively small, simple hexacyanometallate species. This is likely due to the difficulty of preparing oligomeric species with terminal cyano groups that are available for binding other components in supramolecular architectures; attempts at synthesizing such species typically results in intractable materials with extended structures, rather than discrete molecules.

One interesting material recently reported by Baraldo et al. is a *Trans*-[(py)₄Ru[M(CN)₆]₂]⁴⁻ trimer system in which *M* is divalent Fe (the FeRuFe trimer) or Cr (the CrRuCr trimer) (Figure 3-1).^{49,50} One of the notable properties of this material is its ten terminal cyanide groups which are available for coordination to other metals. These open binding sites make it possible to use these trimers as subunits in the creation of larger supramolecular materials, making it a rare example of an oligomer cyanometallate species with the potential to be used as a supramolecular building block.

As the sodium salts of these trimer systems are water-soluble, it is hoped that they can serve as a subphase component for the creation of extended cyanometallate networks at the air-water interface when combined with the macrocyclic nickel

amphiphile described in Chapter 2. The exact geometry that will be taken on by such a networked film is difficult to predict, as there are multiple binding geometries available. It is hoped that the resulting film will display long-range magnetic ordering between the hexacyano iron and chromium groups and the divalent nickel atoms in the amphiphile. As the Ni^{II} has unpaired electrons in its e_g orbitals and the hexacyano trimer iron and chromium atoms have unpaired electrons in their t_{2g} orbitals, the coupling between the nickel and hexacyanometallate units is expected to be ferromagnetic at low temperatures.

Experimental

Synthesis

Synthesis of the *trans*-[(py)₄Ru[M(CN)₆]₂]⁴⁻ trimer species, where M = Fe and Cr, was carried out according to published procedure⁴⁹ by Justin Gardner and Luis Baraldo.

Monolayer Preparation

Langmuir monolayers were prepared with the macrocyclic nickel-containing amphiphile as described in Chapter 2.

Results

Surface Pressure vs. Mean Molecular Area Isotherms

As stated in Chapter 2, when the macrocyclic Ni^{II} amphiphile is spread over an aqueous subphase containing 0.5M NaCl it forms a well-behaved isotherm that begins to increase in surface pressure at approximately 80 Å² and collapses at approximately 60 Å² when compressed. When the monolayer is prepared over a subphase of equal ionic strength that contains 10 mM CrRuCr or FeRuFe trimer anions, the surface pressure begins to increase at 160 Å² and collapses (as indicated by BAM

observations) at 120 \AA^2 (Figure 3-2), with the FeRuFe trimer system displaying a slightly steeper slope.

BAM

BAM observations of amphiphile 1 over a 0.5M NaCl subphase show ordinary amphiphile behavior, with fluid regions at high mean molecular areas (Figure 2-12). When the monolayer is prepared over a subphase of equal ionic strength that contains 10 mM CrRuCr or FeRuFe trimer anions, the resulting films show rigid, condensed regions at high mean molecular areas (above 200 \AA^2). At 160 \AA^2 , the area at which surface pressure began to increase, large areas of bare water were still visible. The monolayer collapses along the boundaries of the rigid regions at approximately 120 \AA^2 (Figure 3-3, 3-4).

ATR FT-IR

A monolayer of the film prepared over the CrRuCr subphase and FeRuFe subphase was transferred to a silicon ATR crystal and analyzed with FT-IR. The resulting spectra for the CrRuCr film (Figure 3-5) showed a primary cyanide peak centered at 2210 cm^{-1} , with shoulder peaks at 2125 and 2070 (Figure 3-6). The FT-IR spectrum of the FeRuFe film shows a primary cyanide peak centered at 2120 cm^{-1} , with a large shoulder peak at 2060 (Figure 3-7).

XPS

XPS spectrums of the films were obtained by transferring ten layers of each system onto a silicon slide. The relative abundance of Ni, Cr, and Ru in the resulting Ni amphiphile/CrRuCr trimer film were found to be 1:2:1, indicating a trimer:amphiphile ratio of 1:1 (Figure 3-8). The relative abundances of Ni, Fe, and Ru in the Ni

amphiphile/FeRuFe trimer film were found to be 1:4:2, indicating a trimer:amphiphile ratio of 1:2 (Figure 3-9).

SQUID Magnetometry

Films of 51 layers of the CrRuCr system and 25 layers of the FeRuFe system were transferred to a Melonex substrate for magnetic characterization. The magnetic characterization was performed by Elisabeth Knowles of the UF Department of Physics. M vs. H measurements were taken from 0-7 T at 2K, while χ vs. T measurements were taken from 0-300 K at 100 G. For the Ni amphiphile/CrRuCr system the M vs. H measurements fit well to a Brillouin function for a relative 1:2 Ni:Cr abundance, although the magnitude was consistent with a film transfer ratio of 0.2 rather than the observed transfer ratio of 0.8. The χ vs. T measurements were fitted to a Curie law with a Curie constant of 1.91 ± 0.07 emuK/mol with a χ_0 of 0.203 ± 0.004 emu/mol (Figure 3-10). For the Ni amphiphile/FeRuFe system, the M vs. H measurements fit well to a Brillouin function for a relative 1:4 Ni:Fe abundance if Fe was assigned a g value of 3.2. The χ vs. T measurements were fitted to a Curie law with a Curie constant of 5.82 ± 0.09 emuK/mol with a χ_0 of 2.52 ± 0.01 emu/mol (Figure 3-11).

Discussion

The appearance of condensed, rigid regions of film at high mean molecular areas as observed by BAM when a monolayer of the Ni-containing amphiphile is prepared over a subphase containing FeRuFe or CrRuCr trimers is consistent with the formation of an extended cyanometallate network beneath the Langmuir monolayer. BAM observations of the monolayer during compression over a CrRuCr or FeRuFe subphase reveal that there are still substantial areas of bare water at the onset of surface pressure increase, indicating that the monolayer is not efficiently filling all available surface area.

It appears that the surface pressure begins to increase when rigid islands of monolayer begin to bump against each other and are unable to efficiently pack on the surface. This is similar to the behavior of the networked monolayers described in Chapter 2. Over a NaCl subphase the monolayer behaves fluidly, and these rigid islands are not observed. The large increase in the mean molecular area at which surface pressure begins to increase when the amphiphile is spread over a subphase containing the trimers is consistent with the relatively long distance between hexacyanochromate subunits in the trimer, approximately 1 nm.

The CrRuCr film's ATR FT-IR spectrum indicates that binding between the trimer's hexacyanochromate sites and the Ni amphiphile is taking place, as evidenced by the bridging cyanide stretching peak at 2210 cm^{-1} . The shoulder peaks at 2125 cm^{-1} is the result of Cr-CN-Ru cyanide bonds, while the 2070 cm^{-1} peak arises from terminal hexacyanochromate sites on the trimer. Spectroscopic evidence of amphiphile/trimer binding was less apparent for the FeRuFe system, which lacked a clear bridging cyanide peak. The FeRuFe monolayer spectrum showed a primary cyanide peak appears at 2120 cm^{-1} , which corresponds to the Fe-CN-Ru bond in the trimer, and a shoulder peak at approximately 2070 cm^{-1} from the trimer's terminal cyanides.⁴⁹

The relative 1:1:2 abundance of Ni, Ru and Cr in the CrRuCr film as indicated by XPS indicates that the film contains a 1:1 ratio of trimer subunit to amphiphile subunit. This is surprising, as charge balance considerations would predict two 2+ amphiphile units for each 4- trimer subunit. The relative 1:2:4 abundance of Ni, Ru and Fe in the FeRuFe film indicates 1:2 ratio of trimer subunit to amphiphile subunit. This is consistent

with charge balance considerations expectations, which predict two 2+ amphiphile units for each 4- trimer subunit.

It is unclear exactly what geometry, if any, the films possess. The 1:1 ratio of amphiphile to trimer in the CrRuCr film could result from linear chain geometry, isolated amphiphile+trimer dimer units, or an extended disordered structure. The FeRuFe film's 1:2 amphiphile to trimer ratio is consistent with a square geometry, isolated units of an amphiphile bound to two trimers, or a disordered structure. As previously discussed, BAM and surface pressure vs. area isotherms indicate the presence of a condensed, extended structure in the film, which seems to rule out the possibility of isolated amphiphile+trimer units. Since SQUID analysis reveals no extended long-range order in the material, the most likely geometry of the films is therefore an extended but highly disordered network.

Conclusions

Langmuir monolayers of a macrocyclic nickel-containing amphiphile were prepared over a subphase of aqueous *trans*-[(py)₄Ru[M(CN)₆]₂]⁴⁻ trimer system in which *M* is trivalent Fe or Cr in an attempt to create an extended cyanometallate network at the air/water interface. Although BAM observations and surface pressure vs. mean molecular area isotherms indicate that a rigid network is forming, SQUID magnetometry measurements disappointingly failed to find any magnetic ordering within the sample. It is likely that the networks took on a disordered geometry, with little long-range ordering.

Unfortunately any attempt to investigate the geometry of the network with GIXD would likely prove difficult given the relatively large unit cells lengths expected in any network geometry that might form. This will likely make any determination of the network's exact geometry impossible for the foreseeable future.

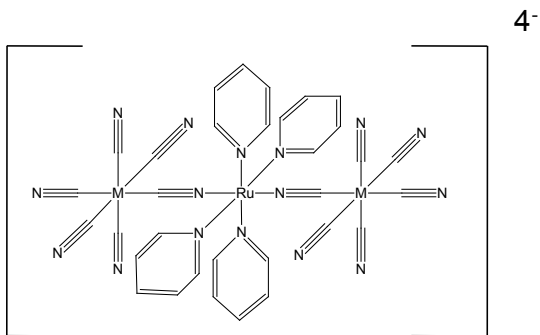


Figure 3-1. A *trans*-[(py)₄Ru[M(CN)₆]₂]⁴⁻ trimer molecule

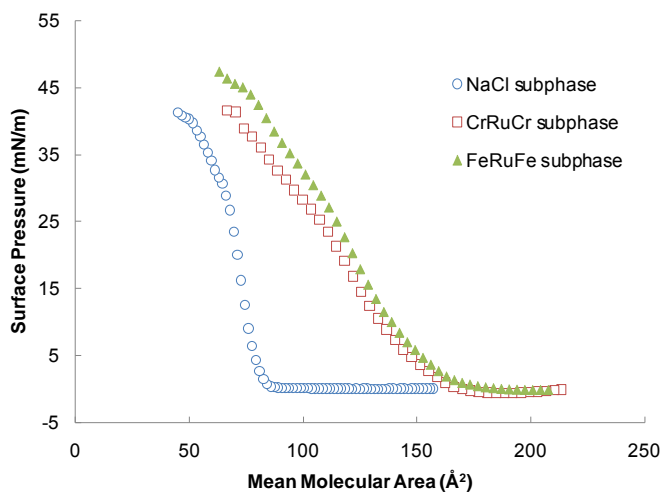


Figure 3-2. Surface pressure vs. mean molecular area isotherm of macrocyclic Ni amphiphile over NaCl subphase (circles), CrRuCr trimer subphase (square), and FeRuFe trimer (triangles).

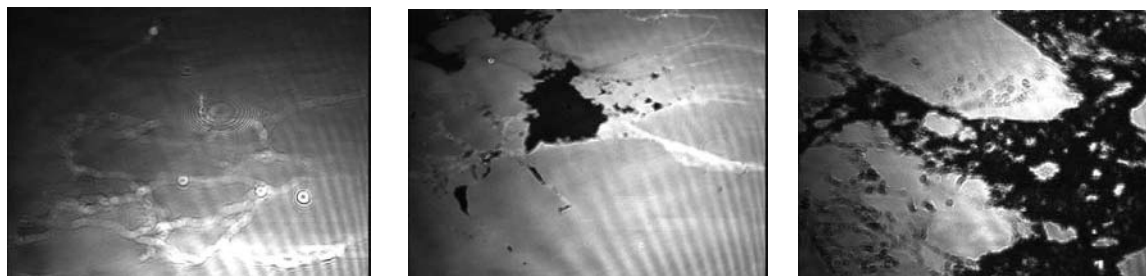


Figure 3-3. BAM of macrocyclic Ni amphiphile over CrRuCr trimer subphase at 200 Å² (right), 160 Å² (center) and 120 Å² (left).

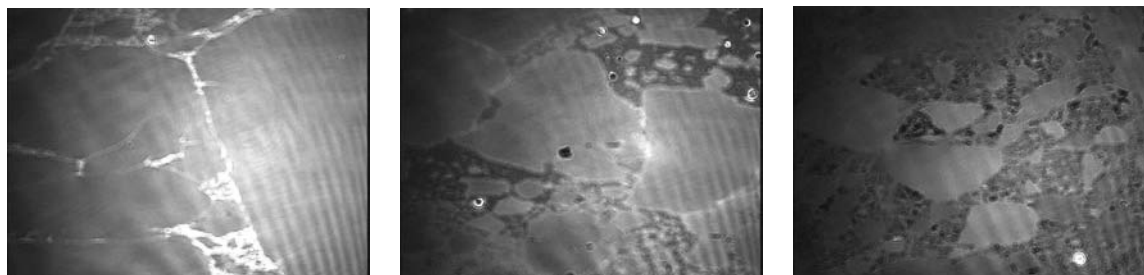


Figure 3-4. BAM of macrocyclic Ni amphiphile over FeRuFe trimer subphase at 200 Å² (right), 160 Å² (center) and 120 Å² (left).

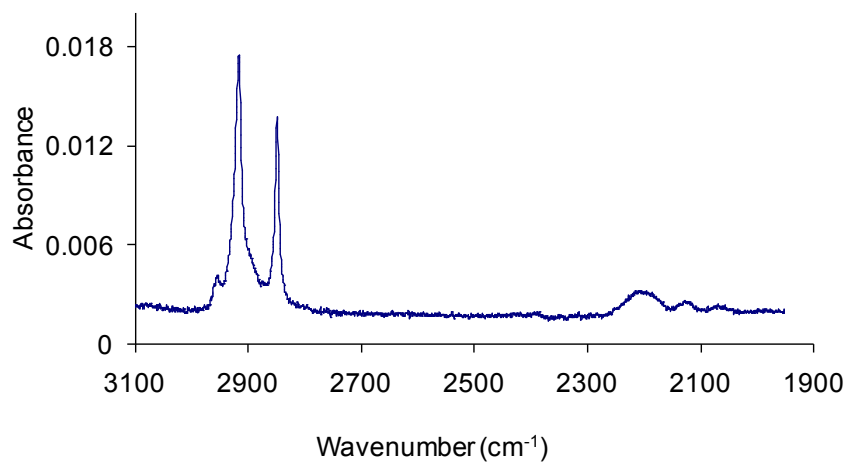


Figure 3-5. ATR FT-IR spectrum of the macrocyclic Ni amphiphile over a CrRuCr trimer subphase, transferred to a Si ATR crystal.

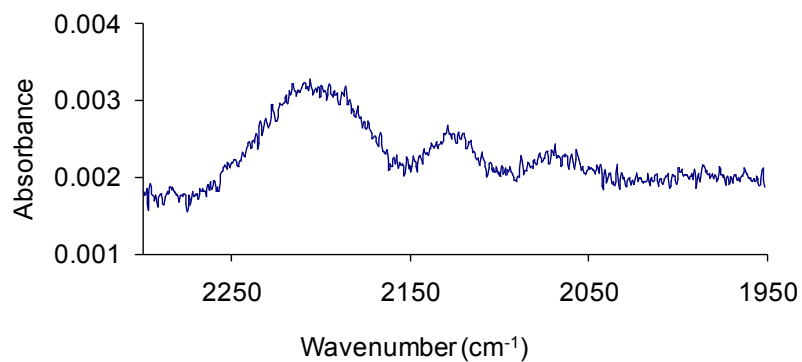


Figure 3-6. Cyanide stretching region of ATR FT-IR spectrum of the macrocyclic Ni amphiphile over a CrRuCr trimer subphase, transferred to a Si ATR crystal.

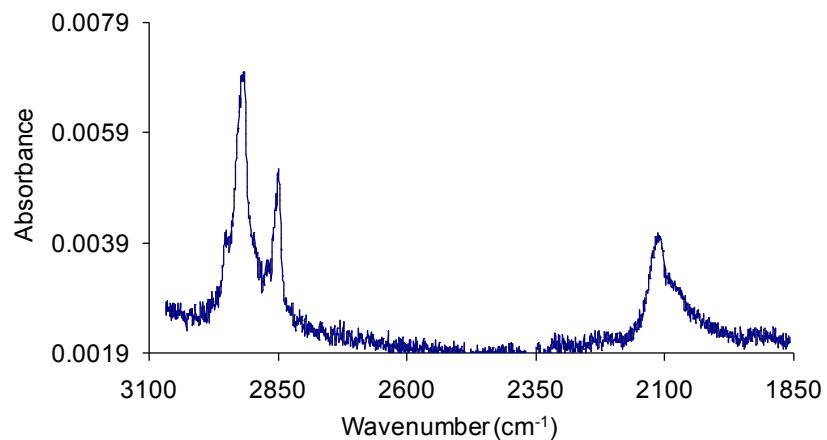


Figure 3-7. ATR FT-IR spectrum of macrocyclic Ni amphiphile over FeRuFe trimer subphase, transferred to a Si ATR crystal.

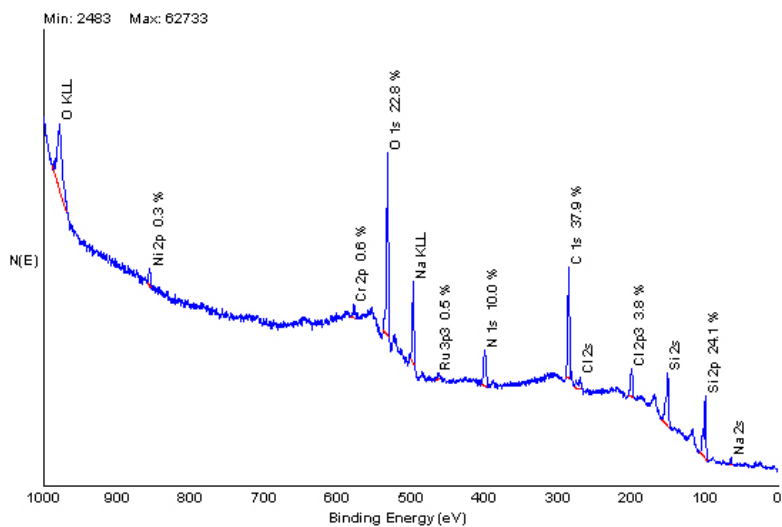


Figure 3-8. XPS spectrum of the macrocyclic Ni amphiphile over CrRuCr trimer subphase.

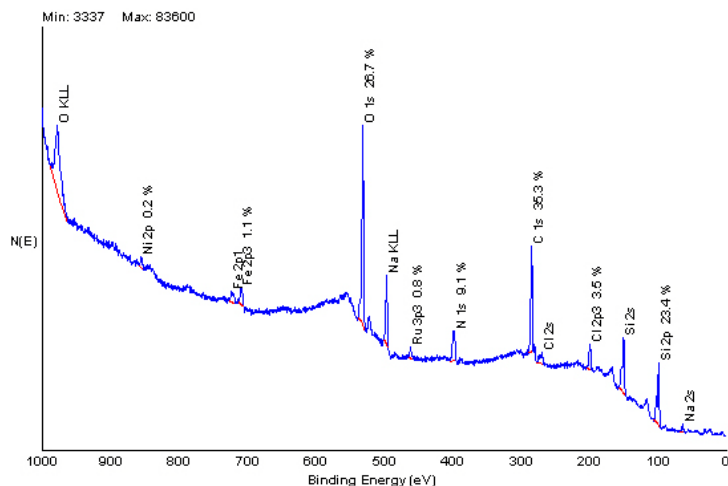


Figure 3-9. XPS spectrum of macrocyclic Ni amphiphile over FeRuFe trimer subphase.

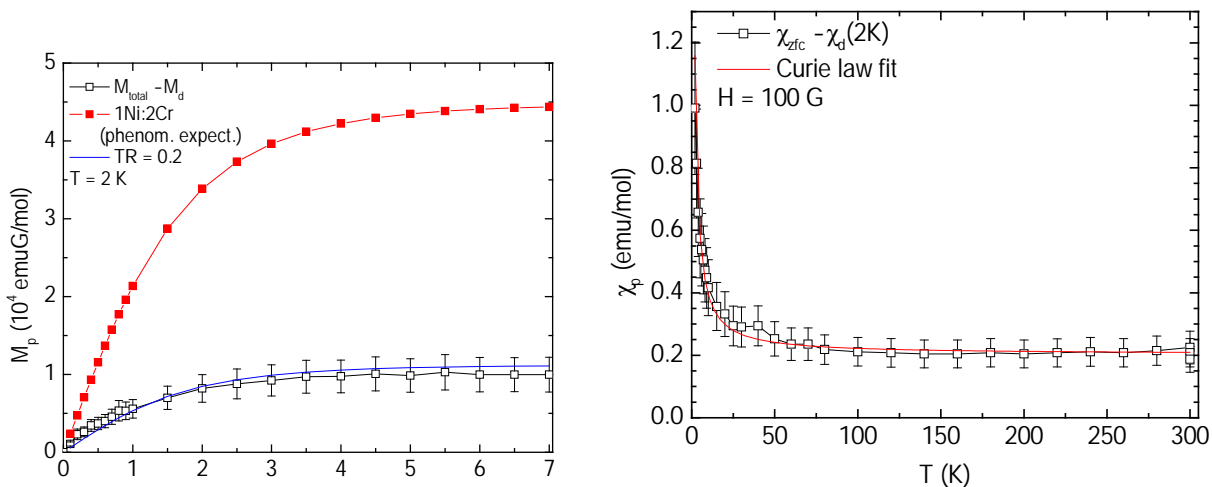


Figure 3-10. Magnetic characterization of the macrocyclic Ni amphiphile over CrRuCr trimer subphase. Paramagnetic magnetization (M_p) as a function of magnetic field (H) (left) and paramagnetic susceptibility (χ_p) as a function of temperature (T) (right).

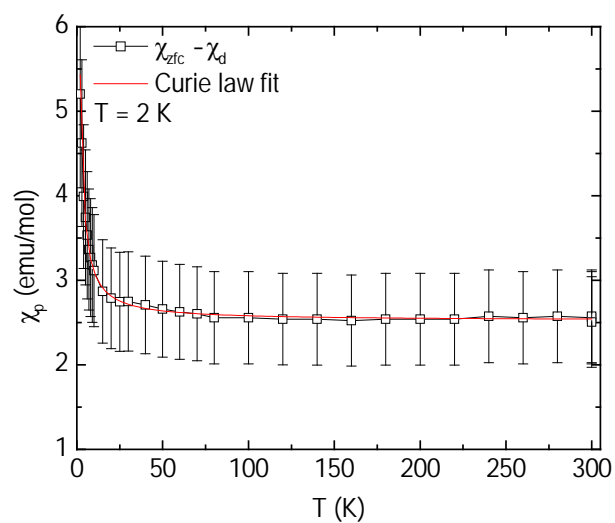
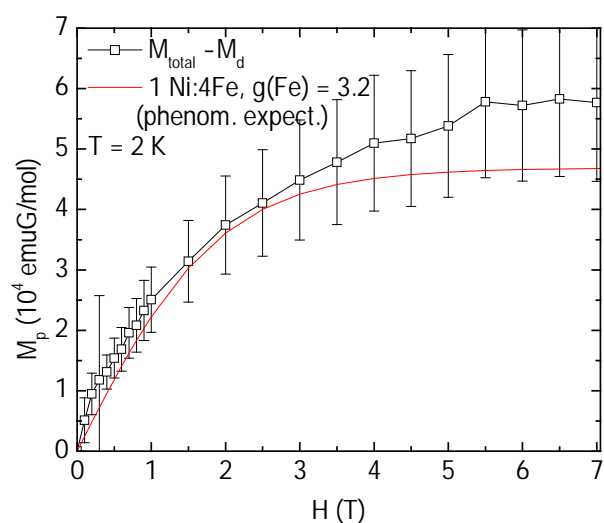


Figure 3-11. Magnetic characterization of the macrocyclic Ni amphiphile over FeRuFe trimer subphase. Paramagnetic magnetization (M_p) as a function of magnetic field (H) (left) and paramagnetic susceptibility (χ_p) as a function of temperature (T) (right).

CHAPTER 4 PRUSSIAN BLUE/TITANIUM DIOXIDE NANOCOMPOSITES

Introduction

Prussian blue analogs (PBAs) are a class of cyanometallate coordination polymer in which divalent or trivalent metal atoms are linked together by cyanide ligands, forming a cubic lattice. Most PBAs have the idealized formula $A_4M_a^{II}4[M_b^{III}(CN)_6]_4$, where A is an alkali cation that is incorporated into the lattice to balance charge and M_a and M_b are any transition metal or combination of transition metals (Figure 4-1). Most PBA structures do not correspond to their idealized formula, and balance the charge of their lattice partly through absences of cyanometallates rather than entirely with alkali cation incorporation. The resulting open coordination sites on the divalent metal species from such absences are typically filled by water molecules.

The all-iron analog where M_a is Fe^{3+} and M_b is Fe^{2+} undergoes facile inner-sphere electron transfer through the cyanide ligands, and behaves as Class II Robin-Day mixed-valence compounds. The magnetic⁵¹⁻⁶³, electrochemical⁶⁴⁻⁷⁵, electrochromic,⁷³⁻⁸² cation absorption,⁸³⁻⁸⁵ gas storage,⁸⁶⁻⁸⁹ and other properties of Prussian blue and its analogs have made it the subject of intense study.^{52,90-96}

Prussian blue's ability to store positive and negative charge by reducing M^{III} sites within its lattice to M^{II} or oxidizing M^{II} sites to M^{III} , combined with its ability to balance changes in charge by incorporating or expelling lattice cations or protons, presents the possibility of using PB as a novel material for charge storage. The purpose of this chapter is to demonstrate that Prussian blue can serve as a charge storage media for the purpose of storing photo-excited electrons from a photosensitizer.

Titanium dioxide is a wide-band gap semiconductor whose photocatalytic properties have been the subject of extensive research and many reviews.⁹⁷⁻¹⁰³ Although TiO₂ has been shown to be an effective photo-oxidizer of a wide range of molecules and a photo-reducer of a limited variety of molecules, its efficiency is hampered by its relatively short excited-state lifetime and poor ability to store multiple photo-excited electrons in its conduction band.

In order to increase TiO₂'s efficiency, it is often coupled to a second material with a LUMO or conduction band at or below the energy level of the TiO₂. This allows the TiO₂ to inject photo-excited electrons into the secondary material. (Figure 4-2)

In addition to increasing the excited-state lifetime of the system by separating the charges and so increasing the time it takes them to recombine, the second material can serve as a charge storage reservoir that accumulates high-energy electrons and saves them for later use in reduction reactions. Such electron-accumulating system typically couple TiO₂ to metallic nanoparticles with Fermi levels below TiO₂'s conduction band, like gold or silver.¹⁰⁴⁻¹⁰⁶ Although nanocomposites of TiO₂ coupled to a variety of electron-accepting semiconductors^{107,108}, metals,¹⁰⁴⁻¹⁰⁶ and molecular species^{109,110} have been demonstrated, there have been few examples of coordination polymers coupled to TiO₂.

A major potential advantage that PB has over previously-reported electron accepting materials is its ability to use cation influx to balance any increase in negative charge within its lattice from reduction of Fe^{III} sites to Fe^{II} sites. Other semiconductor or metal materials that can be coupled to TiO₂ will eventually undergo Fermi equilibration with the conduction band of the TiO₂ as more and more electrons are added to them

and the accumulated negative charge raises the material's Fermi level, which limits the number of electrons they can accept.¹⁰⁶ Since PB is able to balance changes in lattice charge by incorporating or expelling alkali cations and protons, it should not face issues with Fermi equilibration. The high density of states in PB's LUMO also helps to minimize problems with Fermi equilibration, as any excess negative charge will be highly localized. Additionally, any excess negative charge stored in conductive electron-accepting materials will typically be distributed along the surface of the material. Since the surface area/volume ratio decreases as the size of materials increases, most potential electron-accepting materials will be able to store fewer electrons per volume characteristics as the size of the material increases. PB, on the other hand, stores the electrons that it accepts upon reduction of Fe sites that are distributed throughout the internal volume of the material, allowing its charge storage per volume characteristics to remain the same regardless of the size of the material. Unlike metals, there is believed to be no significant change in the charge-storage properties of PB as particle sizes change, other than an increase in storage capacity directly proportional to the particle's volume. The number of electrons stored in metallic nanoparticles will therefore increase proportionally to the square of the material's radius, while the number of electrons stored in a PB nanoparticle will increase proportionally to the cube of the material's radius (Figure 4-3).

In order to maximize the charge transfer abilities of the TiO₂ to the PB, PB nanoparticles were synthesized via a dialysis technique and then coated with TiO₂ using sol gel deposition from a titanium oxo precursor that anchors to the surface of the PB.

After synthesizing and characterizing the PB/TiO₂ nanocomposite, its photo-induced charge transfer and photocatalytic utility were evaluated.

A number of TiO₂/PB composite materials have been reported previously. Early reported hybrid materials consisted of PB material electrodeposited onto the surface of a TiO₂ electrode from aqueous solutions of trivalent iron and ferricyanide.¹¹¹⁻¹¹⁴ More recent reports have electrode materials prepared by electrochemically reducing a solution containing aqueous trivalent iron, ferricyanide, and suspended TiO₂ nanoparticles. The resulting films consisted of bulk PB material with TiO₂ particles trapped inside.^{115,116} Others have reported the deposition of thin layers of PB onto the surface of TiO₂ nanoparticles via photo-reduction of a solution containing aqueous trivalent iron, ferricyanide, and suspended TiO₂ nanoparticles.^{117,118}

None of these reported hybrid materials attempted to investigate whether or not coupling the PB to TiO₂ enhanced the TiO₂'s photocatalytic effects by allowing the PB to act as an electron acceptor. It is unlikely that any of the reported systems would be useful for photocatalytic enhancement, since they all involve covering the TiO₂ material with PB; this would likely restrict access to the catalytically-active TiO₂ surface. It is hoped that by coating the PB particles with TiO₂, the PB will be able to serve as an electron-accepting reservoir without hampering access to the TiO₂'s photocatalytic surface.

Because TiO₂'s band gap is in the near-UV region (3.3 eV), various dye molecules that absorb in the visible region and have excited states at or above the energy of TiO₂'s conduction band are often used to sensitize it to visible light. In this work we will couple the amorphous TiO₂ coating to the dye rhodamine B, a dye that has been

demonstrated to sensitize TiO₂ to visible light. It is thus hoped that electrons from the rhodamine B will be promoted to a high-energy state by visible photons that allow the photo-excited electrons to transfer into the conduction band of the TiO₂, and from there into the BP cores (Figure 4-4). In order to prevent rapid oxidation of the material by the oxidized dye, I⁻ will be present in the solution to serve as a sacrificial electron donor for the photo-oxidized dye.

Experimental

Synthesis

Prussian blue nanoparticles

Cubic 10 nm nanoparticles of PB were synthesized by slowly dripping 10 ml of a 10 mM aqueous solution of FeSO₄ into 10 ml of 15 mM aqueous K₃Fe(CN)₆ over a period of about 15 minutes with constant vigorous stirring. The resulting solution was stirred for a further 30 minutes and then placed in a dialysis tube. The dialysis tube was placed in a 1.0 L beaker of deionized water and the solution was dialyzed for 48 hours with periodic changes of the water to remove excess K₃Fe(CN)₆. The resulting particles were analyzed by TEM, UV/Vis, and FT-IR spectroscopy.

Ni^{II}Cr^{III} PBA nanoparticles

Ni^{II}Cr^{III} PBA nanoparticles were prepared without surfactant from an aqueous solution via a technique similar to the one described by Mallah et. al.¹¹⁹ 20 ml of 5 mM aqueous K₃Cr(CN)₆ was slowly dripped into 20 ml of aqueous 5 mM NiCl₂ and CsCl with vigorous stirring. Stirring was continued for 10 minutes after the addition was complete, after which time samples of the solution were removed for TEM and FT-IR analysis, or for TiO₂ coating.

TiO₂-Coated Prussian Blue Particles

The procedure for coating the PB particles in TiO₂ is similar to the method reported by Hirakawa and Kamat¹⁰⁶ in their synthesis of TiO₂-coated gold nanoparticles. 5.0 ml of aqueous PB particles (2.2 mg/ml) were added to 70 ml of ethanol. 25 µl of titanium triethanolaminatoisopropoxide was added to the solution and stirred for 10 minutes, after which the solution was refluxed for 60 minutes to hydrolyze the TTEAIP into amorphous TiO₂ (Figure 4-5). The TiO₂-coated particles were separated by centrifugation. Excess TTEAIP was removed by re-dispersing them into ethanol and re-collecting with centrifugation three times. The resulting particles were analyzed via TEM, EDS, FT-IR, and UV/Vis. This same procedure was also used for coating the NiCr particles.

Thallium Staining for TEM Analysis

In order to improve contrast between the TiO₂ and PB components of the resulting nano-composite, the material was dispersed in 5 mL of water and 120 mg of TlCl. After stirring for two hours to allow the PB to absorb the thallium, the solution was placed in a dialysis bag and dialyzed in 1.0L of water with constant stirring for 5 hours to remove any excess thallium that had not been absorbed into the PB lattice. The 5mL of aqueous particle suspension was then diluted with 70 ml of ethanol. 25 µl of the ethanol/water suspension were dropped into a TEM grid and allowed to air dry over night.

Photo-oxidative Experiments

In order to evaluate whether or not charge transfer from the TiO₂ to the PB would enhance the photocatalytic properties of the TiO₂, 40 nM suspensions of the composite material in benzyl alcohol and isopropanol were irradiated for one hour with a 500W

mercury vapor lamp in an open quartz cuvette with constant stirring. The solutions were then analyzed via GC/MS to determine the concentrations of the respective ketone oxidation products. In both experiments an analogous composite material prepared with the Ni^{II}Cr^{III} PBA, rather than Fe^{II}Fe^{III} PB, served as a control. Since the LUMO of the Ni^{II}Cr^{III} PBA is too high in energy for photo-excited TiO₂ to reduce, any photocatalytic activity observed in the Ni^{II}Cr^{III} material should be due solely to the TiO₂.

Visible Light-Induced Charge Transfer Evaluation

The ability of rhodamine B to sensitize the PB/TiO₂ nanocomposite to visible light was evaluated by irradiating a 2 ml methanolic solution of 40 nM (by PB content) PB/TiO₂ particles, 2mM rhodamine B, and 7.8 mM sacrificial I⁻ with a 60W incandescent tungsten lamp for ten minutes. The intervalent charge transfer absorption in the PB was monitored with UV-Vis. spectroscopy to determine the extent of the photo-induced charge transfer from the rhodamine to the PB.

Materials

All materials were used as received from Sigma-Aldrich or Fisher-Acros or as synthesized above. Deionized water was filtered through an 18 MΩ Barnstead Nanopure filtration system.

Instrumentation

Photo-experiments were carried out with a 500 W Spectroline mercury vapor lamp and 60W incandescent tungsten lamp. UV-Vis spectra were acquired with a Varian Cary 50 spectrometer.

Results

Prussian Blue/TiO₂ Nanocomposite Synthesis

TEM analysis of the PB nanoparticles created via dialysis of a FeSO₄/K₃Fe(CN)₆ solution showed discrete nanoparticles with a diameter of approximately 10 nm. (Figure 4-6) After coating with TiO₂ and staining the PB material with thallium to improve contrast, darker areas of PB with distinct lattice fringes were observed surrounded by lighter areas of TiO₂. No lattice fringes were observed for the lighter-contrast TiO₂ material, which is consistent with the amorphous nature of TiO₂ prepared via the sol gel technique. EDS analysis indicated the presence of Ti (42% relative abundance), Fe (46% relative abundance), and K (12% relative abundance). When the TTEAIP was hydrolyzed without PB nanoparticles present in the solution, it produced multi-hundred nanometers agglomerates of TiO₂ as seen in Figure 4-6. The lacy carbon grid of the TEM slide is visible in the background.

NiCr PBA/TiO₂ Nanocomposite Synthesis

TEM analysis of the NiCr PBA nanoparticles created by combining aqueous solutions of K₃Cr(CN)₆ and NiCl₂ showed 10 nm particles. After TiO₂ coating the particles formed aggregates bound together by TiO₂. As with the PB/TiO₂ material, darker regions with lattice fringes are believed to be PBA, while the lighter regions without fringes are the amorphous TiO₂ coating (Figure 4-7). EDS analysis indicated the presence of Ti (48% relative abundance), Ni (16% relative abundance), Cr (17% relative abundance), and Cs (19% relative abundance).

UV Photo-Induced Charge Transfer Evaluation

The ability of the PB/TiO₂ nanocomposite to store photo-excited electrons by transferring them from the conduction band of the TiO₂ to the LUMO of the PB was

evaluated by dispersing the particles in methanol in an air-tight quartz cuvette and irradiating them with UV light. PB has an intense absorption at ~700 nm due to an intervalence electron transfer from the carbon-coordinated Fe^{II} sites to the nitrogen-coordinated Fe^{III} sites. (Figure 4-8)

Since the LUMO of the PB is centered on the Fe^{III} lattice sites and reduction of the PB involves the reduction the Fe^{III} sites to Fe^{II}, the transfer of electrons from the conduction band of the TiO₂ to the PB should shut down the 700 nm intervalence charge transfer band and cause the PB to become colorless. The colorless, all-Fe^{II} form of PB is known as “Prussian white.” This change in visible absorption upon reduction of the PB makes it convenient to follow the electron transfer process via UV-Vis spectroscopy.

A solution of separately-prepared BP and TiO₂ nanoparticles was evaluated using the same procedure to determine the effects of directly coupling the TiO₂ to the PB. It is hoped that the intimate, high-surface-area contact between the PB and TiO₂ will increase charge transfer efficiency.

The intervalence charge transfer band in the nanocomposite gradually disappeared upon irradiation of the particles in methanol, indicating the transfer of photo-excited electrons from the TiO₂ portion of the nanocomposite to the PB portion (Figure 4-9).

Upon opening the cuvette and exposing the particles to air, the intervalence charge transfer absorption band gradually reappeared, indicating that the Prussian white was oxidized back to PB by atmospheric oxygen. Re-sealing the cuvette and re-irradiating the particles results in re-reduction of the PB to Prussian white. The system

can be cycled multiple times, with a slight reduction in the intensity of the returned signal upon each re-oxidation (Figure 4-10).

Although separately-prepared TiO₂ and PB nanoparticles displayed a similar decrease in the intervalence charge transfer band upon irradiation with UV light in methanol, the rate of decrease was substantially slower (Figure 4-11).

Photocatalysis

The GC/MS peak areas of the benzyl aldehyde and acetone oxidation products were normalized to the peak areas of their respective benzyl alcohol and isopropanol starting materials. It was hoped that the TiO₂ would photocatalytically oxidize the alcohols according to the equation:



Comparisons of the relative amounts of the oxidation products of benzyl alcohol and isopropanol revealed no catalytic advantage to the TiO₂/PB nanocomposite; in fact, the control NiCr PBA/TiO₂ particles performed better all trials. Both the NiCr/TiO₂ control particles and the PB/TiO₂ particles performed significantly better than the controls with no particles, indicating that the TiO₂ on both sets of particles is photocatalytic (Figures 4-12 and 4-13).

Visible Light Sensitization with Rhodamine B.

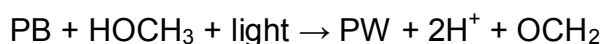
The intervalence charge transfer band in the PB portion of the nanocomposite showed no change upon irradiation with visible light in methanol in the presence of rhodamine B alone. Upon addition of 7.8 mM I⁻ as a sacrificial electron donor, the intervalent charge transfer band rapidly disappeared (Figure 4-14).

Discussion

After the TiO₂ coating procedure the intervalence charge transfer band in the PB that normally appears at 680 nm was found to be shifted to 750 nm. This behavior has been reported before in systems in which TiO₂ is closely coupled to PB, and is likely due to a stabilization of the Fe^{III} centers in the PB, which lowers the energy required to transfer an electron from a Fe^{II} site to a Fe^{III} site.^{111,116,120}

The disappearance of the intervalent charge transfer band in the PB portion of the nanocomposite upon UV irradiation in methanol indicates that the TiO₂ is able to transfer photo-excited electrons into the PB lattice, reducing the Fe^{III} sites to Fe^{II} sites and creating Prussian white. This demonstrates that PB can serve as an electron-storage medium when coupled to a material capable of generating photo-excited electrons.

The conduction band of amorphous TiO₂ lies at +2.6 V vs. SCE, giving it more than enough oxidizing power to oxidize methanol to formaldehyde, formic acid, or carbon dioxide. Given the relatively large ratio of methanol to nanocomposite in the solution, it is unlikely that the solvent would be reduced more than once. It is therefore most likely that the photo-excited TiO₂ is oxidizing the methanol to formaldehyde to replace the low-energy hole in its conduction band. This releases an H⁺ cation, which can then be incorporated into the PB lattice to balance the negative charge of the electron that the TiO₂ injected into the PB. The overall reaction, then, can be described as:



The return of the intervalent charge transfer peak in the material's UV spectrum upon exposure to atmospheric air proves that the loss of the peak during UV irradiation

was not merely due to the destruction of the PB material by the photocatalyst. During the initial photoreduction/oxidation cycle the intervalent charge transfer peak only grows back to approximately 75% of its initial value. In subsequent photoreduction/oxidation cycles, the intervalent charge transfer peak grows back to near its starting value. There are two possible explanations for this behavior. The first possibility is that a significant portion of the PB material is being destroyed during the initial photoreduction. Although it is certainly plausible that the photo-excited TiO_2 could oxidatively damage the PB, especially given their close contact with each other, there is no clear reason why more PB material would be damaged by the irradiation process during the first irradiation than by subsequent irradiations. The second, more plausible explanation is that approximately 25% of the PB nanoparticles are so thoroughly coated with TiO_2 that they are not accessible to atmospheric oxygen, and are thus protected from oxidation.

The rate of photoreduction of the PB in the PB/ TiO_2 nanocomposite is found to be faster than the rate of a mixture of separately-prepared TiO_2 and PB of equal concentration; this indicates that the close contact between the BP and TiO_2 helps improve the efficiency of the photo-induced charge transfer, and that systems with TiO_2 directly deposited onto the surface of the electron-accepting cyanometallate are therefore superior to separately-prepared mixtures of TiO_2 and cyanometallate for charge-storage applications.

It is not surprising that irradiation of the nanocomposite with visible light in the presence of rhodamine B resulted in no photoreduction of the PB when iodide was not present, as the relatively high oxidizing potential of the rhodamine would probably allow it to quickly recover its lost electrons by oxidizing the any Prussian white that was

generated. Once iodide was added as a sacrificial reductant, however, the photo-oxidized rhodamine was able to oxidize the iodide, leaving the photo-reduced PB stable.

Unfortunately there was no apparent photocatalytic advantage to coupling the TiO₂ to PB when attempting to oxidize benzyl alcohol or isopropanol. It is possible that this is due to relatively low electron mobility in the TiO₂. Photoexcited electrons in the conduction band of TiO₂ tend to become trapped on Ti⁴⁺ sites, and charge recombination usually occurs when mobile “holes” in the valence band collide with stationary conduction band electrons.¹²¹ It is therefore possible that the photochromism of the particles arises from the TiO₂ carrying out an oxidation of the methanol solvent while in a photoexcited state followed by the transfer of an electron to the PB. If that is the case, the electron transfer would be of little catalytic utility, since it would only occur after an oxidation has already occurred.

Conclusions and Future Work

A nanocomposite of PB nanoparticles coated in TiO₂ was prepared by a sol-gel technique in which a TTEAIP titanium-oxo precursor with an affinity for the PB nanoparticle's surface was hydrolyzed. The resulting nanocomposite was photochromic in methanol due to the transfer of photo-excited electrons from the conduction band of the TiO₂ to the LUMO of the PB. Although electron transfer from the TiO₂ to the PB is clearly taking place, no increase in oxidative photocatalytic activity of the TiO₂ toward benzyl alcohol or isopropanol was found. The material could be sensitized to visible light by rhodamine-B, which is able to inject electrons into the conduction band of the TiO₂ upon irradiation with visible light.

Although the nanocomposite failed to show an increase in photocatalytic activity, it demonstrated that PB can serve as a charge-accumulation medium for the collection of

photoexcited electrons from TiO_2 . It was further demonstrated that coupling the TiO_2 directly to the PB provided superior charge-transfer characteristics compared to separately-prepared TiO_2 and PB.

A potentially interesting avenue of research that was not explored in this work is the possibility of using the high-energy electrons stored in the PB material to carry out reduction reactions. There are several advantages that the PB/ TiO_2 nanocomposite could have over TiO_2 alone. First, as explained earlier in the chapter, the PB material is able to store far more electrons for future use in reduction reactions than TiO_2 . As the Prussian white material was stable indefinitely so long as it wasn't exposed to any oxidizing agents, the possibility exists to store large numbers of high-energy electrons for long periods. One could thus potentially decouple the irradiation of the composite material from any reduction reactions that might be carried out later; UV light could be shined on the composite material until all of the PB had been reduced to Prussian white, after which time the light could be turned off and the material that one wished to reduce could be added. Separate irradiation and reduction steps could be especially useful in situations where UV irradiation of the composite particles in the presence of the reactant would result in undesired side products.

A second major advantage that the nanocomposite system could have over TiO_2 when carrying out reduction reactions is the ability to carry out multi-electron reactions. As previously discussed, the electrons in the conduction band of TiO_2 have low mobility, and because of this TiO_2 has very poor performance when carrying out multi-electron reductions. It is possible that the Prussian white material could deliver multiple electrons to reactants quickly, facilitating multi-electron processes. This process might allow the

nanocomposites to reduce common small halogenated pollutants like trichloroethene or methylene chloride.

Even if Prussian white itself is not found to be a good material for carrying out multi-electron reductions, it is possible that the portion of PB that is not covered by TiO_2 could be modified with either a molecular catalyst or a third material that acted as a catalytic surface. This additional molecule or material could then serve as the catalytic site at which the reduction reaction takes place, with the Prussian blue simply acting an electron-storage medium in which the photoexcited electrons from the TiO_2 are accumulated before being transferred to the catalytic species.

If molecular catalytic species are used in such a scheme, the catalyst molecules would need to have a HOMO that was low enough in energy to accept electrons from the HOMO of the Prussian white when the catalyst is in its resting state, so that the Prussian white can transfer electrons to the catalyst to replace the electrons lost when it carries out reduction reactions. If a catalytic material such as gold is used, the material would need to have a conduction band lower in energy than the HOMO of Prussian white for the same reason. Gold is one such potential material, as it has a Fermi level below the HOMO of Prussian white. The exposed surfaces of the PB could be modified with short thiol-containing ligands such as cysteamine to promote bonding of gold nanoparticles to the PB, although it is not known to what extent the presence of such connecting ligands would interfere with electron transfer from the PB to the gold. Since the surface plasmon band of gold nanoparticles changes significantly as charge is added, the transfer of electrons from the Prussian white to the gold nanoparticles could be easily monitored with UV/Vis spectroscopy.

Although the use of these PB/TiO₂ nanocomposites for carrying out reduction reactions is promising, there are several potential drawbacks that should be kept in mind. First, it is worth noting that such schemes would result in a significant loss of reducing power when the electrons migrate into the PB, as the PB LUMO is 0.75 eV lower in energy than the TiO₂'s conduction band. Second, much of the PB's surface is coated with TiO₂, which could limit the surface area of Prussian white available for carrying out reduction reactions.

It would likely be necessary to optimize the amount of TiO₂ present so as to balance the rate at which electrons accumulate with the amount of catalytically-active surface available. The ideal balance between TiO₂ coating and catalytic surface area would likely depend on many factors, including the speed of the reduction reactions, the intensity of the light source, and whether or not the UV irradiation damaged the catalytic materials or caused any undesirable side-reactions to occur. If the catalytic material is sensitive to UV degradation or if the UV irradiation of the system causes undesired side-reactions, larger proportions of TiO₂ might be necessary to absorb more UV and protect the rest of the system. On the other hand, if the catalytic reductions are slow compared to the rate of electron injection from the TiO₂ into the PB, then less TiO₂ might be desired to increase the catalytically-active surface.

Another possibility for future research is the investigation of sensitizing the material to visible light with a wider variety of sensitizing dyes, and especially with dyes that could be anchored to the surface through carboxylate or phosphonate linkages. Although it was demonstrated that the materials could be sensitized with rhodamine B, the experiments were performed with the rhodamine dye in solution with the PB/TiO₂

dispersion rather than anchored to the TiO₂ material. As will be discussed further in the next chapter, there are a wide variety of dyes that can inject electrons into the conduction band of TiO₂ and that can be anchored to its surface. It is likely that anchoring the dye to the TiO₂ in such a manner would greatly enhance the efficiency of the visible sensitization. It should be noted, however, that such visible sensitization will likely always necessitate the use of a sacrificial electron donor, as the photo-oxidized dyes will never have the oxidizing potential of the TiO₂'s valence band. Sensitization to visible light is therefore much more practical when carrying out the sort of reduction reactions described above, rather than oxidation reactions.

A final possibility for future work could involve investigation of the composite material's photooxidative properties toward a wider variety of organics. The benzyl alcohol and isopropanol experimented upon in this work were chosen primarily for their ease of analysis, and it is possible that photocatalytic oxidation of other materials might prove more successful.

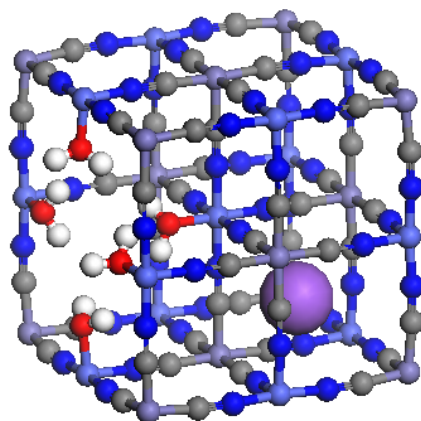


Figure 4-1. A cubic unit cell of Prussian blue lattice

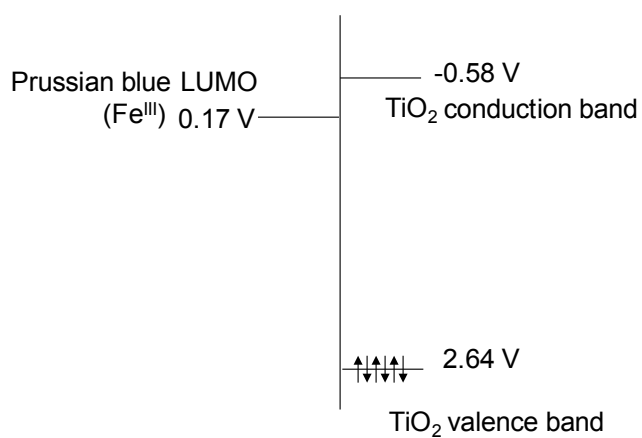


Figure 4-2. Relative orbital energy levels of Prussian blue and TiO₂ vs. Ag/AgCl

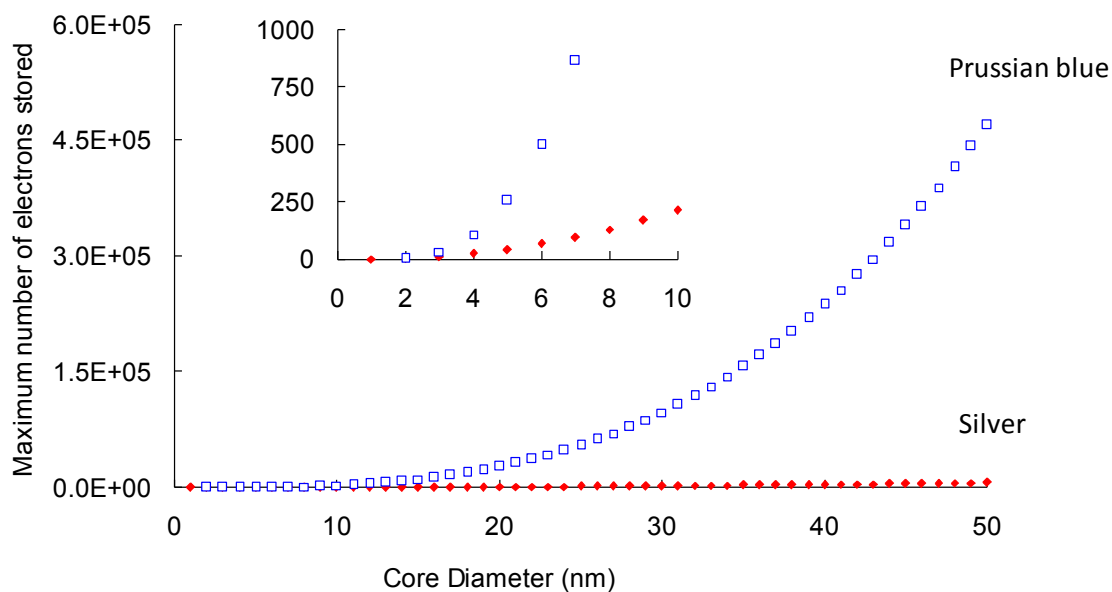


Figure 4-3. Number of electrons that a Prussian blue (open) and silver (filled) nanoparticle can store vs. size. The number of electrons that Prussian blue can store increases linearly with volume, while the number of electrons that silver can store increases linearly with surface area.

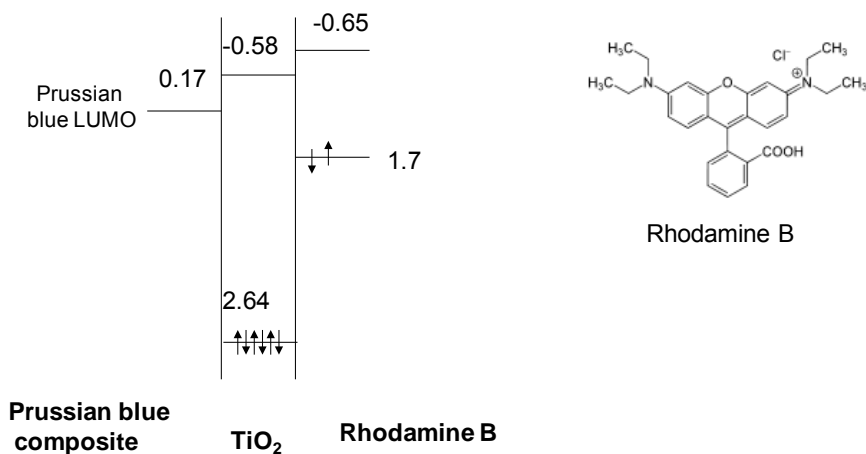


Figure 4-4. Relative orbital energy levels of Prussian blue, TiO₂, and rhodamine B

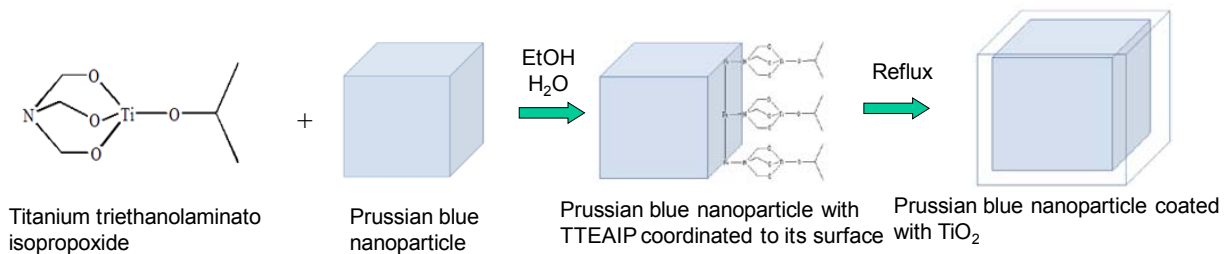


Figure 4-5. Synthesis of TiO_2 coated Prussian blue nanoparticles

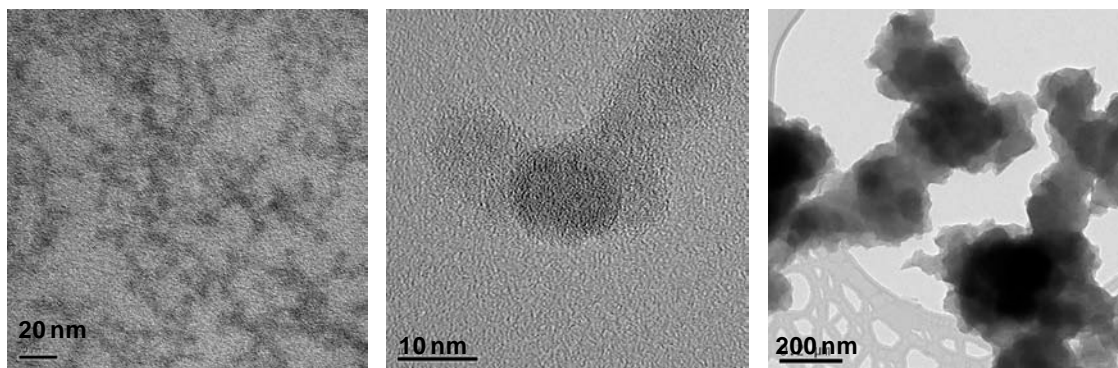


Figure 4-6. TEM of Prussian blue nanoparticles before TiO_2 coating (left), TiO_2 -coated Prussian blue particles after TI staining (center). TEM of TiO_2 product prepared without PB nanoparticles in suspension, with lacy carbon grid visible (right).

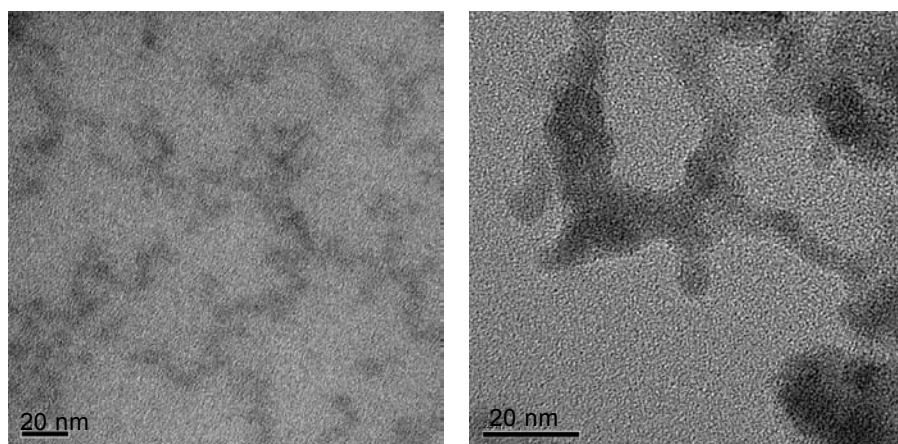


Figure 4-7 TEM of NiCr PBA before TiO_2 coating (left), TiO_2 -coated NiCr PBA particles (right).

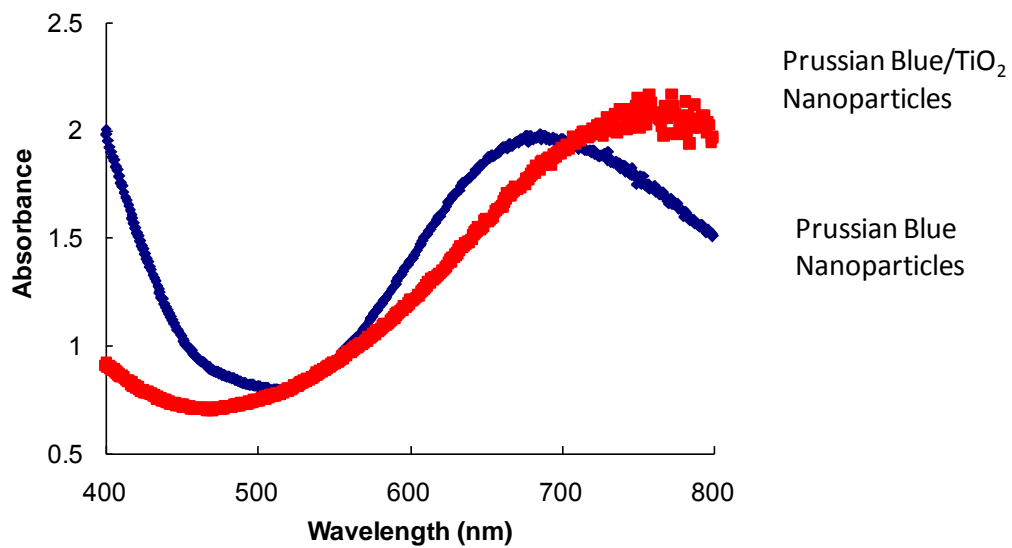


Figure 4-8. UV-Vis spectra of Prussian blue nanoparticles before and after TiO_2 coating.

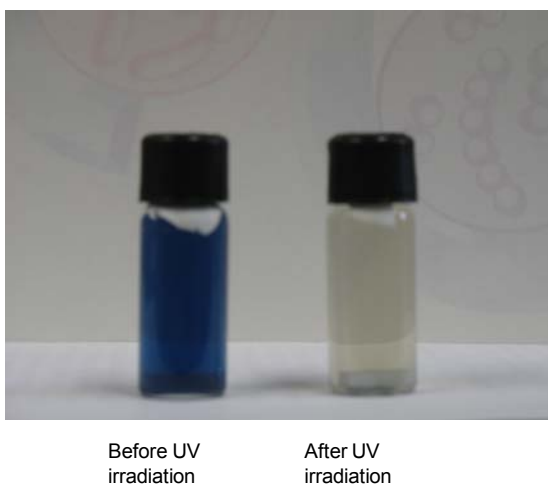


Figure 4-9. Prussian blue/ TiO_2 nanocomposite before and after irradiation.

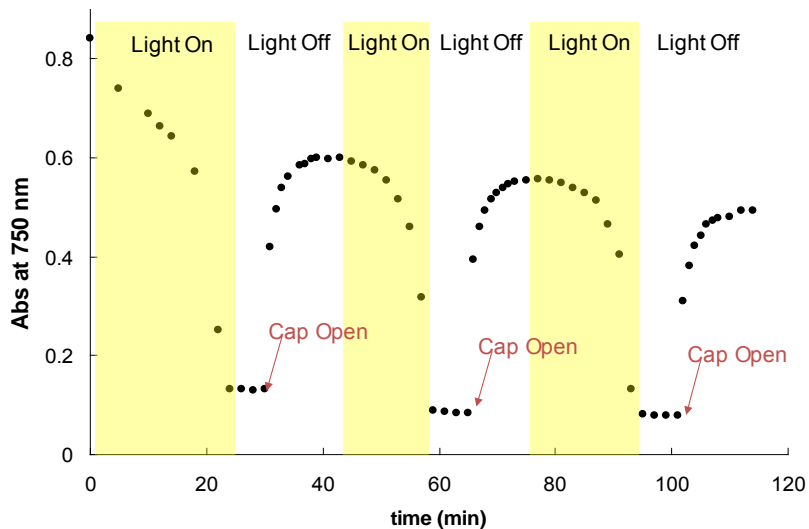


Figure 4-10 Absorption of the Prussian blue/TiO₂ nanocomposite vs. time as the UV lamp it turned on and off.

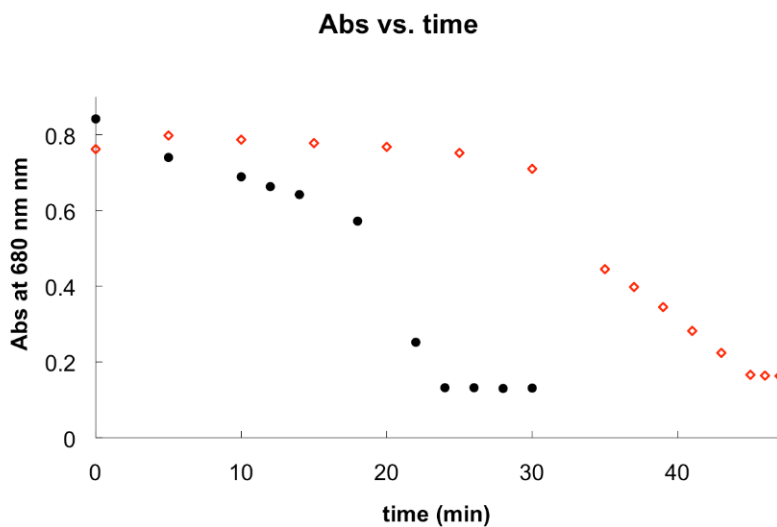


Figure 4-11. Comparison of decrease in intervalence charge transfer absorption vs. UV irradiation time in Prussian blue/TiO₂ nanocomposite (open circles) and separately prepared TiO₂ and Prussian blue (filled circles).

NiCr/TiO ₂ Particles	Sample 1	Sample 2	Sample 3	
Alcohol GC Peak Area	2.85E9	3.93E9	9.35E9	
Aldehyde GC Peak Area	4.51E7	7.19E7	1.53E8	Mean
Normalized Aldehyde Area	0.0156	0.0180	0.0240	0.0192 +/-0.0043
FeFe/TiO ₂ Particles				
Alcohol GC Peak Area	4.92E9	6.11E9	6.94E9	
Aldehyde GC Peak Area	7.26E7	1.08E8	1.29E8	
Normalized Aldehyde Area	0.0145	0.0174	0.0183	0.0167 +/-0.0020
No Nanoparticles				
Alcohol GC Peak Area	4.15E9	4.68E9	5.01E9	
Aldehyde GC Peak Area	5.25E6	5.29E6	4.94E6	
Normalized Aldehyde Area	0.00126	.00113	0.000996	0.0011 +/-0.0001

Figure 4-12. Comparisons of the amount of benzyl aldehyde oxidation product produced upon irradiation of benzyl alcohol with PB/TiO₂ nanoparticles, NiCr BPA control nanoparticles, and no nanoparticles.

NiCr/TiO ₂ Particles	Sample 1	Sample 2	Sample 3	
Alcohol GC Peak Area	4.67E9	2.67E9	5.00E9	
Ketone GC Peak Area	2.63E7	1.32E7	2.61E7	Mean
Normalized Ketone Area	.00561	.00491	.00519	0.00524 +/-0.00035

FeFe/TiO ₂ Particles				
Alcohol GC Peak Area	3.66E9	4.46E9	3.91E9	
Ketone GC Peak Area	5.28E6	6.63E6	5.89E6	
Normalized Ketone Area	.00144	.00149	.00151	0.00148 +/-0.00036

No Nanoparticles

Alcohol GC Peak Area	3.71E9	3.99E9	5.52E9	
Ketone GC Peak Area	6.92E5	6.27E5	5.52E5	
Normalized Ketone Area	0.00019	0.00016	0.00013	0.000157 +/-0.0003

Figure 4-13. Comparisons of the amount of acetone oxidation product produced upon irradiation of isopropanol with PB/TiO₂ nanoparticles, NiCr BPA control nanoparticles, and no nanoparticles.

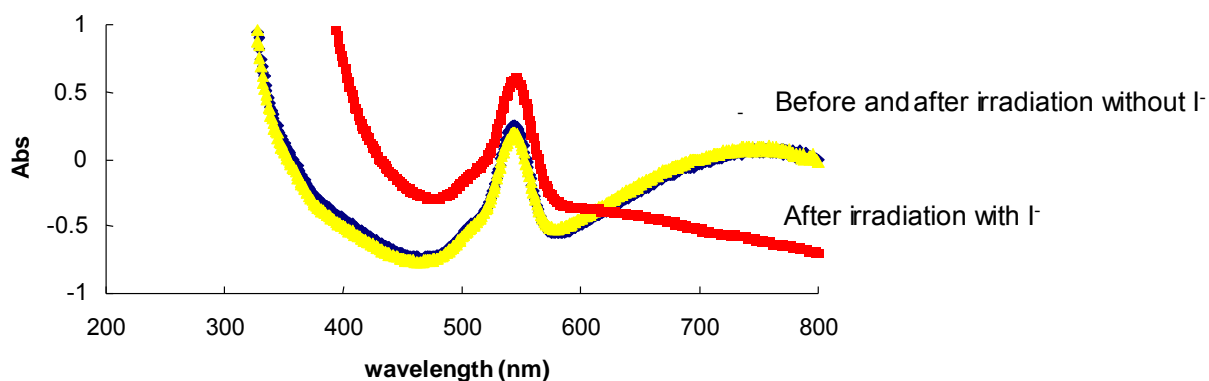


Figure 4-14. UV-Vis spectra of Prussian blue/TiO₂ nanocomposite in the presence of rhodamine B before irradiation (blue), after irradiation (yellow), and after irradiation in the presence of I⁻

CHAPTER 5
PRUSSIAN BLUE ANALOGS AS SOLID ELECTROLYTES FOR DYE-SENSITIZED
SOLAR CELLS

Introduction

Dye-Sensitized Solar Cells

Dye-sensitized solar cells (DSSCs) are a class of low-cost solar cell invented by Gratzel in 1991.¹²² Unlike conventional solar cells, in which electrons are promoted across the band gap of a semiconductor material, DSSCs work by injecting photo-excited electrons from a dye into the conduction band of a semiconductor. Because such a cell's spectral sensitivity is determined by the wavelength of the dye rather than by the band gap of the semiconductor, dye-sensitized cells that respond to visible light can be made from semiconductors whose band gaps are too large to be useful in conventional cells.

After absorbing a photon and transferring an electron into the conduction band of the semiconductor, the dye in a DSSC replaces its lost electron by oxidizing an electrolyte (usually an I^-/I_3^- redox couple). The electrolyte in turn carries charge to an opaque "back" electrode, resulting in an excess negative charge on one side of the cell and an excess positive charge on the other. If connected to a load, work can then be extracted from the charges as they recombine (Figure 5-1).¹²³

The chief advantage of DSSCs compared to conventional solar cells is their low cost to manufacture. Conventional cells require highly pure and highly crystalline semiconductors, which are difficult and expensive to manufacture. Although a wide range of semiconductors, and particularly metal oxide semiconductors, have been used in the fabrication of DSSCs, TiO_2 is by far the most preferred and widely investigated due to TiO_2 's low cost, environmental benignness, and ease of manufacturing. The

semiconductor layers in DSSCs are typically highly nano-porous, or otherwise nano-structured in a way that gives the semiconductor film a high surface area with which the dye and electrolyte can interact.¹²⁴

Many different dyes have been demonstrated as effective sensitizers of TiO₂ in DSSCs. The dyes with the highest reported incident photon-to-current efficiency, the ratio of the total electrical power delivered by the cell to the total optical power striking the cell, thus far are ruthenium pyridine and bipyridine-based dyes. These dyes typically incorporate one or more carboxylate groups on the pyridine moieties to anchor the dye to the TiO₂. Any coordination sites on the ruthenium not taken up by pyridines can coordinate other ligands as necessary to modify the electronic or spectral properties of the dye. Most ruthenium-based dyes in DSSCs have cyanide or thiocyanide ligands coordinated to any excess ruthenium coordination sites, as these ligands red-shift the absorption of the dye, allowing it to harvest a larger fraction of sunlight. A wide variety of non-ruthenium-based dyes have been demonstrated as well, including porphyrins,¹²⁵⁻¹²⁸ organic dyes such as rhodamines^{129,130} or anthrocyanins¹³¹, and even metal nanoparticles that are able to sensitize TiO₂ with surface plasmon effects.^{132,133}

DSSC Electrolytes

By far the most successful and widely-used electrolyte in DSSCs is a liquid solution of I⁻/I₃⁻ redox couple in ethylene glycol, glycerin, or other organic solvent. The liquid nature of the electrolyte allows it to easily fill the pores of the TiO₂/dye film, resulting in a high contact area between the electrolyte and dye. As I⁻ is oxidized to I₃⁻ by the photo-oxidized dye, the I₃⁻ migrates toward the cell's back electrode, where it is reduced back to I⁻. The back electrode in such cells is typically graphite or platinum, which catalyze the reduction of I₃⁻.

Although DSSCs with liquid electrolytes are inexpensive to manufacture and have achieved efficiencies as high as 11%,¹³⁴ they present a number of problems. Liquid cells are difficult to keep sealed under real-world conditions, and often suffer from evaporation or leaking of the electrolyte over time. Liquid cells also have problems with outside contaminants entering the cell, which can poison the cell and decrease its efficiency over time. Finally, there is a great interest in creating low-cost solar cells on flexible substrates. The use of flexible materials only serves to amplify the cell's problems with leaking and contamination.

Because of the limitations of liquid electrolytes, many alternatives have been explored. Ionic liquids, which are electrically conductive and have negligible vapor pressures, can serve as DCC electrolytes that do not appreciably evaporate.¹³⁵⁻¹³⁸ Polymer gels have also been demonstrated, which also help to slow solvent evaporation.¹³⁹⁻¹⁴² Conducting organic polymers have probably received the greatest attention, with some poly(3,4-ethylenedioxythiophene)-based designs achieving efficiencies of nearly 7%.^{143,144}

Although many alternatives to liquid electrolytes have been demonstrated, very little attention has been paid to inorganic materials as solid-state electrolytes for DSSCs. Vapor-deposited layers of CuI,¹⁴⁵⁻¹⁴⁷ CuBr,¹⁴⁸ and CuSCN¹⁴⁹ were demonstrated to be effective electrolytes with efficiencies as high as 2%, but their long-term stability was low due to gradual oxidation of the copper.

Prussian Blue Analogs as Solid DSSC Electrolytes

Given the large amount of attention DSSC electrolyte systems have received, it is remarkable that so little research has been devoted to the use of inorganic materials as

solid electrolytes. Prussian blue analogs (PBAs), in particular, are an attractive potential option for solid-state DSSC electrolytes that are deserving of further study.

PBAs can conduct due to a “charge hopping” intervalent charge transfer mechanism in which electrons rapidly move from divalent to trivalent metal sites via inner-sphere electron transfer across the bridging cyanide ligands.^{150,151} The HOMO and LUMO energy levels of PBAs can be tuned by varying the divalent and hexacyanometallate species, allowing PBAs to be made compatible with the electronic levels of various dyes.

When selecting a PBA and sensitizing dye, the primary concerns will be ensuring that 1) the LUMO of the PBA is too high in energy to be reduced by the photo-excited dye, so as to prevent injection of electrons in the wrong direction; 2) the HOMO of the PBA is as low in energy as possible (but not so low in energy that the oxidized dye cannot oxidize the PBA), so as to maximize the resulting voltage; 3) the dye must be able to bind the cyanide ligands that will connect it to the PBA layer (Figure 5-2). With those criteria in mind, an attractive dye/PBA combination would be (4,4'-dcbpy)₂(CN)₂Ru(II) (**1**) coupled to a Fe^{II}[Cr^{III}(CN)₆] or Co^{II}[Fe^{II}(CN)₆] PBA.¹⁵² (Figure 5-3)

Dye molecule **1** has been shown to be an effective sensitizer in TiO₂-based DSSCs with liquid I⁻/I₃⁻ electrolyte solutions.¹⁵³ Although the ¹MLCT excited state of **1** is energetic enough to reduce the Fe^{II}Cr^{III} PBA, the singlet excited state is extremely short-lived (on the order of femtoseconds).¹⁵⁴ This short lifetime, combined with the ligand-centered nature of the excited state, will hopefully prevent significant electron injection into the PBA electrolyte. The inner-sphere electron transport mechanism responsible for the PBA's conductivity results in an extremely high density of states in

the “valence” and “conduction” bands, which should minimize quenching of the dye’s $^3\text{MLCT}$ state by the PBA.

The $\text{Co}^{\text{II}}\text{Fe}^{\text{II}}$ PBA, unlike the $\text{Fe}^{\text{II}}\text{Cr}^{\text{III}}$ PBA, does not possess a LUMO low enough in energy for the photo-excited dye to reduce the electrolyte material. Unfortunately the HOMO of the $\text{Co}^{\text{II}}\text{Fe}^{\text{II}}$ PBA is only 0.45 V vs. SCE, higher in energy than the 0.7 V HOMO of the $\text{Fe}^{\text{II}}\text{Cr}^{\text{III}}$ PBA. This means that the $\text{Co}^{\text{II}}\text{Fe}^{\text{II}}$ PBA will be less susceptible to electron injection in the wrong direction, but will also have a low maximum open-circuit voltage.

Only one published instance of a cyanometallate network being used as an electrolyte for a dye-sensitized photovoltaic device was found, published in 2006 by Yagi et al.¹⁵⁵ Their system consisted of a Prussian white layer that was electrodeposited from an aqueous $\text{Fe}(\text{CN})_6^{3-}/\text{Fe}^{3+}$ solution onto a WO_3 film sensitized with $\text{Ru}(\text{bpy})_3^{2+}$ dye. The film produces a photoanodic current in the low microamp range upon irradiation with a 500 W Xe lamp. The low photoanodic current was attributed to slow transfer of electrons from the Prussian blue layer to the sensitizing dye and relatively rapid back-transfer of electrons from the WO_3 ’s conduction band to the oxidized dye. Such slow transfer is not surprising, since the Ru^{III} centers in the dye would have been relatively inaccessible to the Prussian blue layer. It was hypothesized that we could resolve the issue of slow PBA-to-dye electron transfer by covalently linking the Ru center in the dye to the Prussian blue layer via a bridging cyanide ligand.

Experimental

Dye Synthesis

The dye $(4,4'\text{-dcbpy})_2(\text{CN})_2\text{Ru}(\text{II})$ was synthesized according to a published procedure,¹⁵³ with modifications to scale and solvent amounts. 200 mg (1 mmol) of

RuCl_3 and 476 mg (1.93 mmol) of 4,4'-dcbpy were combined in 40 ml of DMF and refluxed in the dark under a nitrogen atmosphere for 8 hours. After cooling to room temperature 30 ml of acetone was added, causing $(4,4'\text{-dcbpy})_2\text{RuCl}_2$ to precipitate as a dark green powder. 100 mg (0.15 mmol) of $(4,4'\text{-dcbpy})_2\text{RuCl}_2$ was then combined with 40 mg (0.62 mmol) KCN in 20 ml of a 50% water, 50% methanol solution and refluxed in the dark for 3 hours under a nitrogen atmosphere. Upon cooling 1 M HCl was slowly added with vigorous stirring in a well-ventilated hood, causing the neutral $(4,4'\text{-dcbpy})_2(\text{CN})_2\text{Ru}(\text{II})$ acid product to precipitate as a dark red powder. Care should be taken when working with acidic cyanide solutions as highly-toxic HCN can be generated, although the amounts described herein are below the likely threshold of danger. The product was collected by vacuum filtration and washed with a small portion of ethyl ether. It was then recrystallized in a minimum of ethanol, collected by vacuum filtration, and dried under vacuum (Figure 5-4). (67 mg, 11% by ruthenium) Anal. Calcd for $\text{RuC}_{26}\text{N}_6\text{O}_8\text{H}_{16}$: C, 48.7; H, 2.5; N, 13.1. Found: C, 48.2; H, 2.5; N, 13.3.

Dyed TiO_2 Electrode Fabrication

The first step in the fabrication of the cell was the preparation of a TiO_2 film on the surface of a transparent conductive electrode. Our choice of transparent electrode is fluorine-doped tin oxide (FTO) on borosilicate glass, a conducting substrate that is commonly used in DSSCs due to its relatively low cost and high thermal stability. The FTO glass is first cleaned by sonicating it in aqueous dodecyl sulfonate, water, isopropanol, and finally hexane for 10 minutes each. A mold approximately 20 microns thick is prepared on the conducting side of the FTO glass with 3M scotch tape. A TiO_2 paste is made by combining 5.0 grams of 25 nm anatase TiO_2 particles with 5 ml of deionized water acidified to a $\text{pH} < 2$ with nitric acid and grinding until homogenous. A

few drops of the paste was then placed in the mold and scraped level with a glass rod. This “doctor blade” technique is commonly used in TiO₂ film preparation for DSSCs. After allowing the film to dry for approximately one hour, the tape is removed and the film is sintered in an oven for 30 minutes at 500 C to anneal the nanoparticles to each other and to the FTO surface, as is standard in the fabrication of this type of cell.¹⁵³

After cooling the film was soaked in a 10 mM ethanol solution of the dye for 12 hours to allow the dye to bind to the TiO₂ surface, then washed with ethanol to remove any excess dye. Prior to addition of the PBA layer, exposed FTO areas on the slide were masked with an acrylic polymer to ensure that the PBA was only deposited onto the dyed TiO₂ surface.

PBA electrolyte deposition

Deposition of the FeCr PBA layer onto the dye-modified TiO₂ substrate was accomplished by sequentially dipping into aqueous solutions of the PBA precursors. This technique has been reported previously as a technique for creating thin films of PBA on Melonex surfaces.^{62,63} The cleaned FTO electrode was sequentially dipped into 10 mM aqueous solutions of FeCl₂, deionized water, and K₃Cr(CN)₆ or 10 mM methanolic solutions of FeCl₂ and (PPh₄)₃Cr(CN)₆. During each dipping cycle the slide was submerged in each of the metal solutions for 30 seconds to allow sufficient time for the PBA film to form. The buildup of the PBA layer was monitored by SEM and AFM. A total of 45 dipping cycles were carried out to ensure complete coverage of the surface. Deposition of the CoFe PBA was accomplished using a similar procedure, but with aqueous solution of CoCl₂ and K₄Fe(CN)₆.

Back electrode deposition

After allowing the PBA layer to dry, 100 nm of gold was deposited onto the PBA layer using vacuum physical vapor deposition to serve as an electrical contact. The deposition was monitored with a QCM and performed at pressures below 10^{-6} mmHg.

Efficiency measurements

After fabrication the cell's efficiency was tested using a 160 W Xe lamp fitted with filters to allow it to simulate AM1.5 sunlight. AM1.5 sunlight is artificial sunlight with an intensity similar to that of natural sunlight passing through 1.5 Earth atmosphere equivalents, and is the light source for measuring the efficiency and power output of solar cells. The cell's incident photon to current conversion efficiency is calculated as:

$$E = \frac{P_i}{P_o}$$

where P_i is the total power of the incident light striking cell and P_o is the total electrical power outputted by the cell. The cell's power output was monitored with a digital multimeter.

Results

(4,4'-dcbpy)₂(CN)₂Ru(II) Dye Synthesis

The (4,4'-dcbpy)₂(CN)₂Ru(II) dye was synthesized via a two-step reaction in which the bis-4,4'-dcbpy Ru(II) species was prepared by refluxing RuCl₃ with two molar equivalents of the 4,4'-dcbpy ligand, followed by the replacement of two water ligands with cyanides. The synthesis was based on a previously-reported procedure,¹⁵³ but the scale was changed to minimize the amount of cyanide used in the synthesis. Although the CHN analysis was within acceptable limits and the IR spectra of the product matched the literature, the presence of two apparent cyanide peaks leaves some doubt

as to the purity of the final product. Only one cyanide stretching peak is predicted in the structure, and the 2079 cm^{-1} IR peak is exactly consistent with that of unbound KCN. Never the less, the as-synthesized product has been shown to be an effective sensitizing dye for TiO_2 solar cells. It is likely that any free cyanide impurity in the dye product would be of little consequence, as it would not be expected to anchor to the TiO_2 substrate and would therefore be easily rinsed off at the end of the TiO_2 modification step.

Finished Cell

The finished cell consisted of a layer of sintered TiO_2 nanoparticles deposited onto an FTO-coated glass electrode and modified with the $(4,4'\text{-dcbpy})_2(\text{CN})_2\text{Ru(II)}$ dye. The modified TiO_2 layer was covered with a thin film of PBA electrolyte, which was in turn covered with a vacuum-deposited layer of gold that served as a back electrode (Figure 5-5).

PBA Deposition

SEM and AFM of the TiO_2 substrate during sequential dipping in the FeCl_2 , deionized water, and $\text{K}_3\text{Cr}(\text{CN})_6$ solutions showed cubic crystals of the FeCr PBA approximately 200-300 nm in size that gradually grew and merged as more material was deposited (Figure 5-6, 5-7, 5-8, 5-9, 5-10, 5-11). No regions of exposed TiO_2 were visible after 45 depositions. Cracks appeared in the film after 15 dipping cycles that remained present throughout the dipping process, often splitting regions of the cubic PBA material.

Deposition of the FeCr PBA material from a methanol solution resulted in a less crystalline film that conformed more closely to the morphology of the TiO_2 substrate.

Throughout the dipping process no visible cracks appeared in the PBA layer. (Figures 5-12, 5-13,5-14,5-15)

The CoFe PBA material deposited from an aqueous solution was substantially less crystalline than the FeCr PBA produced via aqueous deposition, but did not conform to the TiO₂ substrate as thoroughly as the FeCr PBA deposited from methanol. (Figures 5-16, 5-17, 5-18. 5-19)

CoFe PBA Penetration into TiO₂ Film

In order to determine whether or not the PBA electrolyte layer was penetrating deeply into the porous TiO₂ film, an EDS analysis was performed on a region of PBA-coated TiO₂ that had been lightly scraped with a metal spatula to break off the PBA and outermost layer of TiO₂. The resulting EDS spectrum showed no iron or cobalt, indicating that the PBA was primarily depositing onto the surface of the TiO₂ film rather than penetrating deeply into it (Figure 5-20).

Cell Efficiency Under Simulated Sunlight

Under simulated AM1.5 sunlight the FeCr cell created via aqueous deposition produced an open circuit voltage of 0.32 V, a short circuit current of 2.5 $\mu\text{A cm}^{-2}$, a total power of $2 \times 10^{-7} \text{ W cm}^{-2}$, a fill factor of 0.3, and overall incident-photon-to-current efficiency was $1.33 \times 10^{-4} \%$ (Figure 5-21). The FeCr cell deposited from methanol produced no photocurrent or other photo-response whatsoever.

The CoFe cell produced an open circuit voltage of 0.52 V, a short circuit current of 9.0 $\mu\text{A cm}^{-2}$, a total power of $7.8 \times 10^{-7} \text{ W cm}^{-2}$, a fill factor of 0.15, and overall incident-photon-to-current efficiency was $5.2 \times 10^{-4} \%$ (Figure 5-22).

Discussion

The photocurrent and overall efficiency of the DSSCs were quite low, and the low fill factors indicated that they were not rectifying properly. There are several possible reasons for the cell's poor efficiency. The most likely problem is lack of contact between the surface of the porous TiO₂ film and the PBA electrolyte. SEM data indicates that the FeCr PBA electrolyte is depositing as large, multi-hundred nanometer crystals on the film's surface. This is likely due to constant dissolving and re-precipitation of the PBA, facilitating crystal growth. Unfortunately this prevents the PBA material from penetrating deeply into the surface of the TiO₂ film as a liquid electrolyte would. Although the conductivity of the PBA is low – on the order of 10⁻³ S/m¹⁵⁶ – the extremely thin nature of the PBA electrolyte layer means that any resistance from the electrolyte will be minimal, and so this is probably not a major contributing factor to cell inefficiency.

The methanolic deposition produced a substantially less crystalline FeCr PBA material, probably due to the negligible solubility of the PBA in methanol. Unfortunately these cells produced no photo-response of any kind. This is likely due to a lack of conductivity in the methanol-deposited FeCr PBA, which was deposited from the tetraphenylphosphonium salt of the cyanometallate and therefore lacks the interstitial cations needed to facilitate charge transfer within the lattice.

Aqueous deposition of CoFe PBA produced a less crystalline film that was still able to conduct electricity. Although the maximum potential open circuit of the CoFe PBA was predicted to be lower than that of the FeCr PBA, in fact the CoFe had the highest open circuit voltage and highest overall efficiency. This is attributed primarily to the lower crystallinity of the CoFe PBA, which allows it to better conform to the surface of the TiO₂ film and thus achieve a higher contact area. Another possible explanation for

the CoFe PBA outperforming the FeCr PBA is possibility of electron transfer from the dye into the FeCr PBA during the dye's short-lived $^1\text{MLCT}$ excited state.

It is currently unknown whether the cracks in the film that are observed in SEM after PBA deposition are the result of mechanical stress on the slide as they were cut into multiple SEM samples, or desiccation cracks. Since desiccation cracks have been observed in other films of PBA deposited with a similar layer-by-layer technique, they seem the most likely explanation.

Unfortunately roughly 75% of the cells that are fabricated as described herein experience problems with shorting between the front and back electrode after the final vapor deposition step. This indicates that the gold vapor is permeating through the PBA electrolyte and TiO_2 layers to make contact with the FTO. It is possible that this problem could be reduced by using a sputter deposition technique rather than vapor deposition.

Conclusions and Future Work

DSSCs with solid-state PBA electrolyte were synthesized, but their performance under simulated sunlight was very poor. This is most likely due to the PBA electrolyte not filling the pores of the TiO_2 material, resulting in very low contact area between the TiO_2 and the PBA. If PBA is ever to serve as an efficient solid-state electrolyte for TiO_2 DSSCs, a deposition technique must be found that will ensure a high contact area. This might be accomplished via a different PBA deposition technique, use of a different geometry in the TiO_2 film, or both.

It is possible that the sequential deposition technique described in this work is a fundamentally flawed method for depositing PBA into a nanoporous substrate, as the first layers to be deposited block subsequent layers of the material from penetrating into the film. One deposition technique that might be more successful is electrochemical

deposition of the PBA material from a solution containing a $[M(CN)_6]^{3-}$ and Fe^{3+} , Ru^{3+} , or another substitutionally-inert metal species. If the TiO_2 film is soaked in such a solution and then used as an electrode for the electrochemical reduction of the trivalent metal species to induce precipitation of the PBA material, it is possible that the PBA layer could be built up from within the film rather than deposited onto its surface. The trivalent metal in the deposited PBA material could then be further reduced to a divalent state if necessary to create the desired analog. The $K_4Fe_4[Cr(CN)_6]_4$ PBA discussed previously in the chapter might be a viable target for such a synthesis.

It is also possible that the type of nanoporous film commonly used in DSSCs with liquid electrolytes is not appropriate for DSSCs with solid PBA electrolytes. There are various other possible geometries of TiO_2 films that could be prepared, such as nanopillars or flat surfaces.¹⁵⁷⁻¹⁵⁹ One of these alternate geometries might be more successful at achieving a high contact area with the PBA. Unfortunately they are all also somewhat more labor-intensive to prepare.

An additional challenge that would need to be overcome in future work is the frequent fabrication of shorted cells. This occurs when the final layer of vapor-deposited gold permeates the PBA and TiO_2 layers to contact the front FTO electrode. It is likely that the desiccation cracks discussed previously are to blame for this phenomenon, so finding a way to eliminate the desiccation cracks would probably significantly alleviate the shorting problem. One possible way to reduce the impact of the desiccation cracks when depositing the PBA layer is to carry out a small number of sequential dips, allow the film to dry completely, and repeat. Although desiccation cracks would likely still develop upon each drying, it is speculated that the cracks from each deposition and

drying cycle would not overlap and therefore not short the cell. It is also possible that the cracks that develop in one deposition and drying cycle would be filled in by PBA in subsequent deposition cycles.

In addition to alleviating the desiccation cracks, it is possible that the shorting problem could be improved by use of a different back-electrode preparation technique that was less prone to permeating the PBA and TiO_2 films. One obvious alternative technique would be sputtering deposition, as the multi-nm metal droplets deposited by sputtering techniques would probably be less penetrating than metallic vapor. Sputtering would also be an attractive deposition technique due to its relative speed, ease, and low cost compared to the vacuum vapor deposition techniques used in this work.

Another improvement that could be made to future cells is the use of a fabrication technique that ensured the PBA would not be in direct contact with the TiO_2 , as contact between the two creates an opportunity for undesired electron/hole recombination. This might be accomplished by modifying the surface of the TiO_2 with a small carboxylate or phosphonate-containing molecule such as acetic or butyric acid. This passivating layer could insulate the TiO_2 from the PBA and ensure that the PBA was primarily in contact with the dye rather than the TiO_2 . Such insulating surface modification of the TiO_2 could be carried out either before or after the TiO_2 was modified with dye. It is likely that the insulating surface modification will interfere with the adsorption of the dye to some extent. This might be minimized by using a dye that forms more robust linkages to the TiO_2 than those of the insulator. For example, a dye with phosphonate binding groups could be used in conjunction with a carboxylate insulator.

As previously discussed, there are a wide variety of dyes that have been demonstrated to be effective sensitizers of TiO_2 for the creation of DSSCs. This work explored only one bipyridine-based dye, leaving a tremendous variety of porphyrins,¹²⁵⁻¹²⁸ organic dyes,^{129,130} and even metal nanoparticle surface sensitizers that could be explored.^{132,133} Porphyrin-based dyes are a particularly attractive possibility, as the PBA electrolyte layer could potentially interact directly with the dye's metal center via a bridging cyanide. It would, of course, be necessary to consider how the presence of such a bridging cyanide ligand would affect the dye's visible absorption spectrum.

A final potential problem with the devices described herein is the possibility that any carboxylate groups on the dye's pyridine moieties that are not anchored to the TiO_2 could bind divalent metal atoms during the initial dipping cycle of PBA buildup. This would be undesirable, as it would result in photoexcited electrons moving toward the PBA electrolyte rather than the TiO_2 . It could also hamper electron transfer from the PBA to the photo-oxidized dye by disrupting the desired inner-sphere electron transfer process through the cyanide ligands. There are two ways this problem could potentially be avoided. One possibility is to use dye molecules with fewer (or only one) carboxylate or phosphonate binding sites, which would presumably be anchored to the TiO_2 's surface and therefore unavailable for binding divalent metals from the PBA deposition solutions. Another possibility is to perform the PBA deposition from slightly acidic solutions. While this would lower the carboxylate or phosphonate's propensity for binding divalent metal ions, it could also interfere with the dye's attachment to the TiO_2 surface.

Although the cells demonstrated thus far have not been very successful, there are still many different cell designs and other parameters to be explored. It is hoped that this work will inspire further investigation of the use of PBAs as solid electrolytes in DSSCs, and perhaps other types of electronic or electrochemical devices.

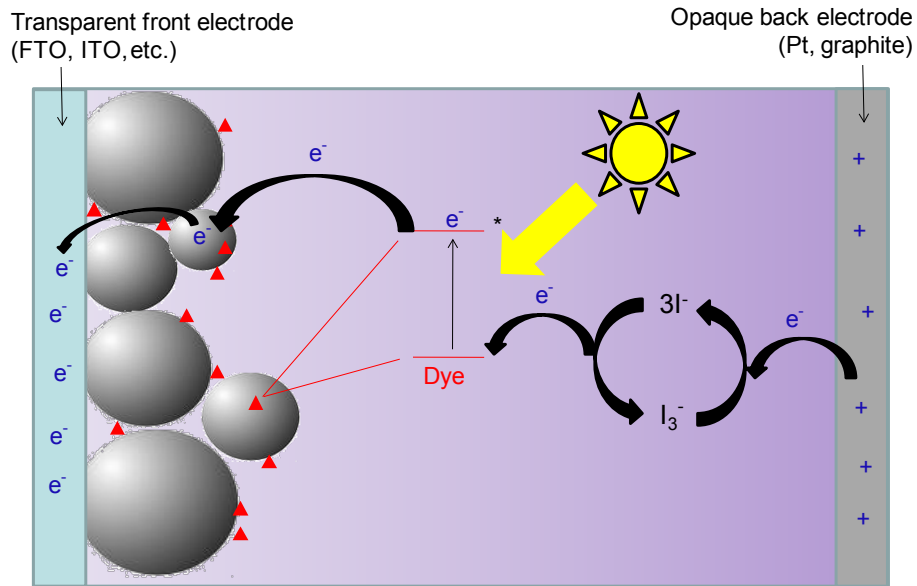


Figure 5-1. Mechanism of a Gratzel cell

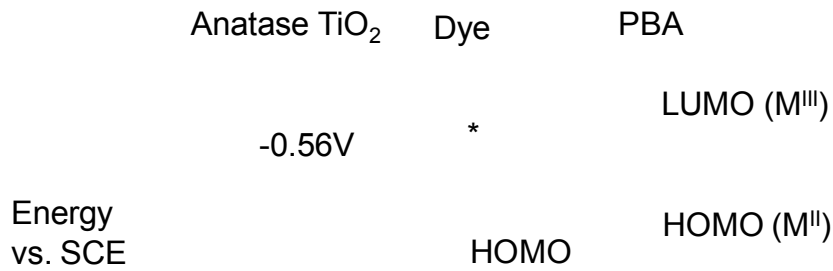


Figure 5-2. Relative energy levels of TiO₂, sensitizing dye, and Prussian blue analog necessary for a DSSC to function with a solid PBA electrolyte

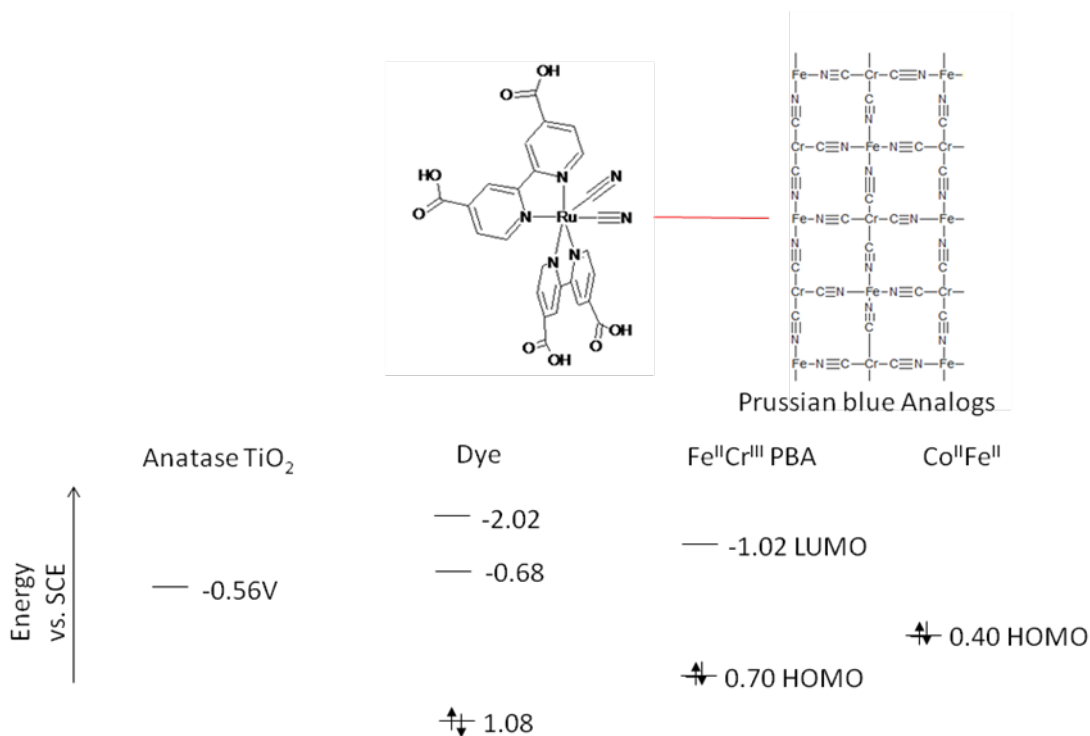


Figure 5-3. Relative orbital energy levels of the (4,4'-dcbpy)₂(CN)₂Ru(II) dye, Fe^{II}/Cr^{III} PBA, and Co^{II}/Fe^{II} PBA. The FeCr lattice is depicted linked to the dye via a bridging cyanide.

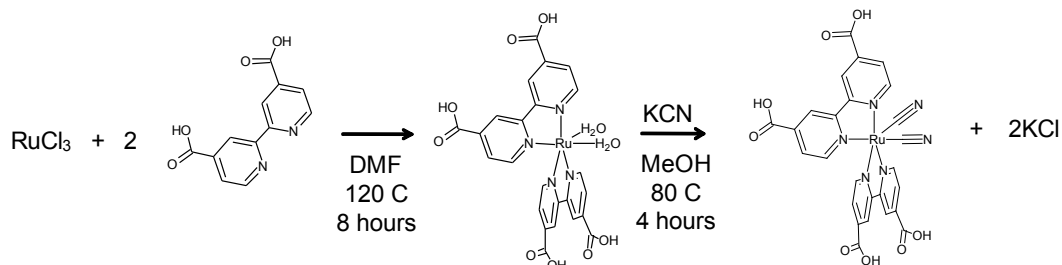


Figure 5-4. Synthesis of the (4,4'-dcbpy)₂(CN)₂Ru(II) dye

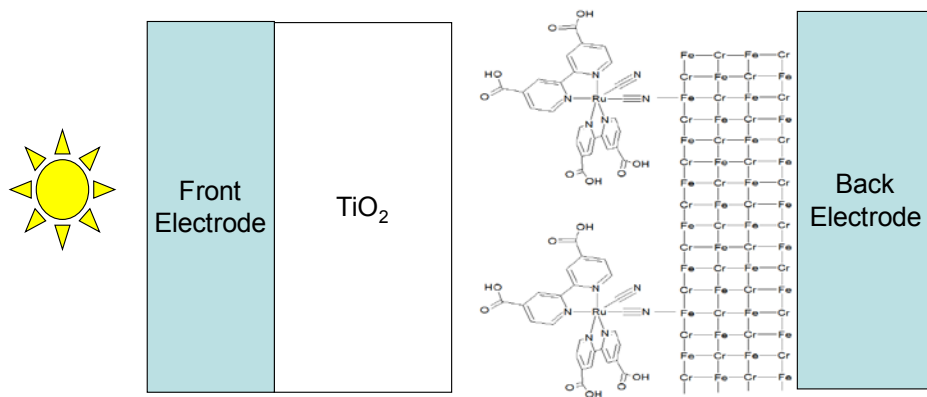


Figure 5-5. Schematic of finished cell

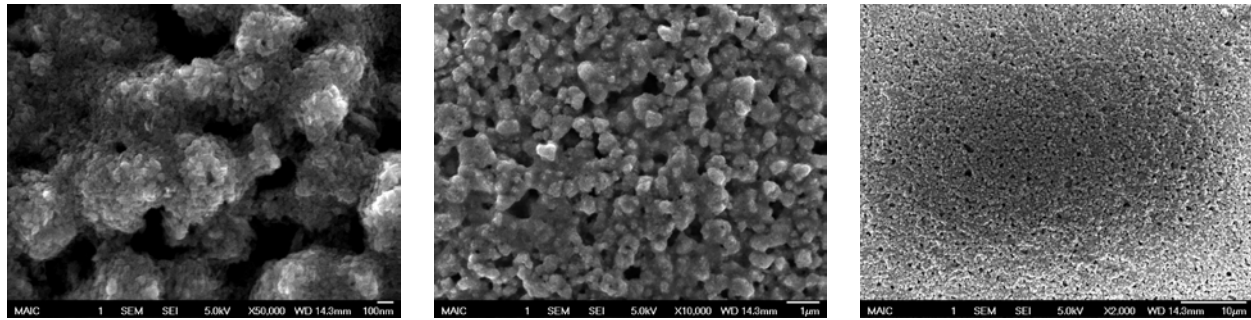


Figure 5-6. SEM of the TiO_2 film at various magnifications.

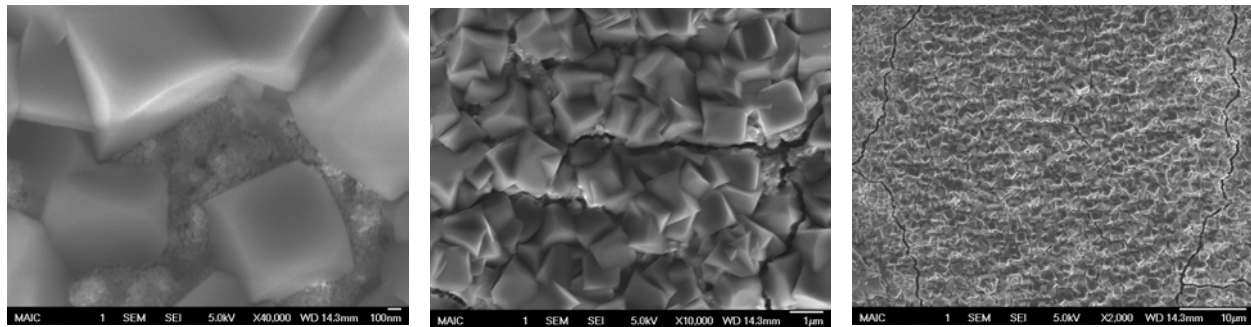


Figure 5-7. SEM of the TiO_2 film at various magnifications after 15 deposition cycles of the FeCr PBA from water. Desiccation cracks are visible in the center and right images.

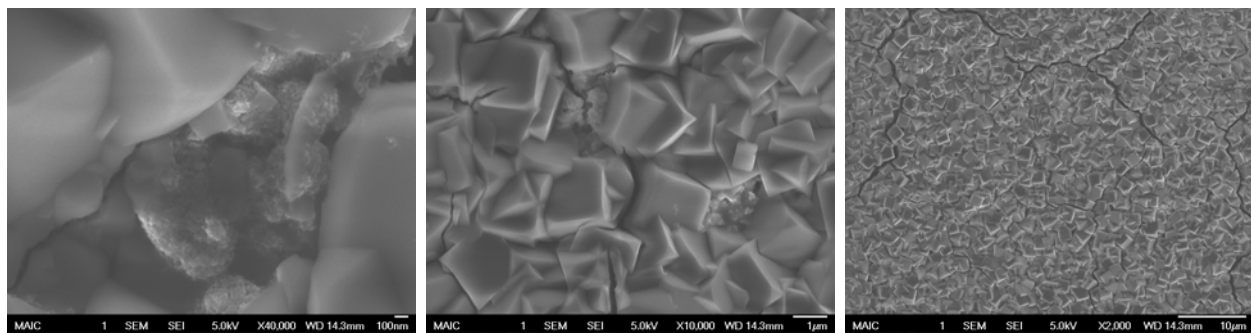


Figure 5-8. SEM of the TiO_2 film at various magnifications after 30 deposition cycles of the FeCr PBA from water. Desiccation cracks are visible in the center and right images.

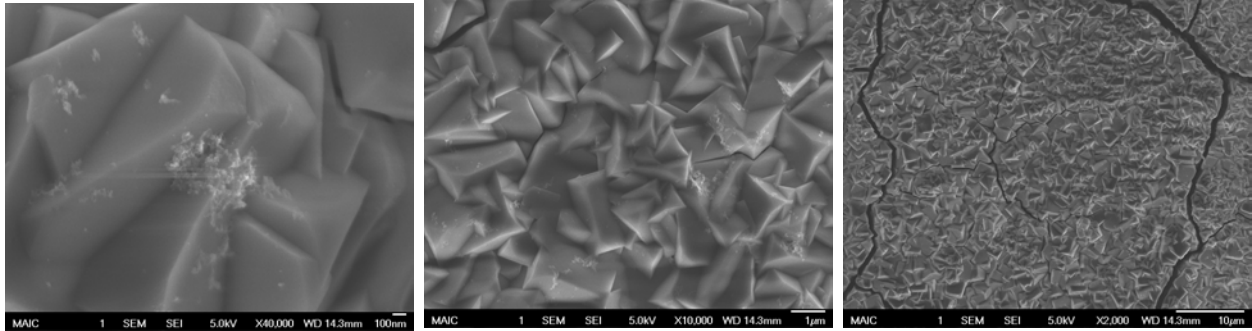


Figure 5-9. SEM of the TiO₂ film at various magnifications after 45 deposition cycles of the FeCr PBA from water. Desiccation cracks are visible in the center and right images.

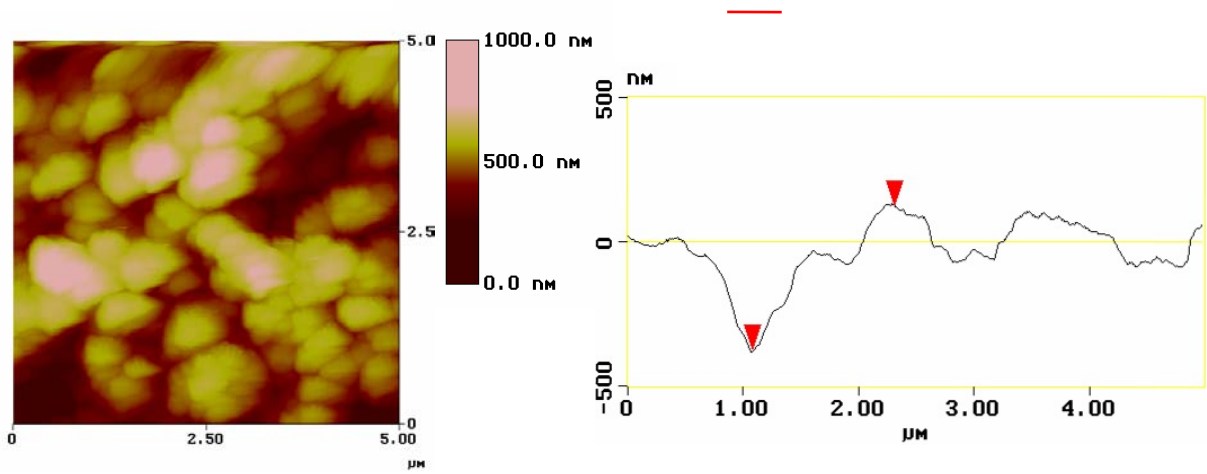


Figure 5-10. Tapping mode AFM image of the TiO₂ film before PBA deposition (left). AFM Depth profile of the TiO₂ film before PBA deposition (right).

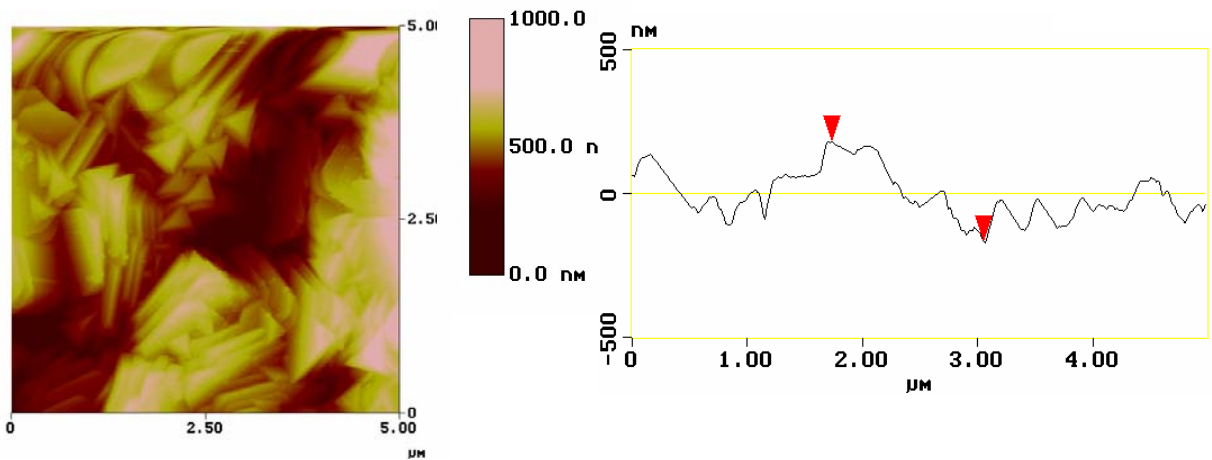


Figure 5-11. Tapping mode AFM of the TiO₂ film after 45 FeCr PBA deposition cycles(left). AFM Depth profile of the TiO₂ film after PBA deposition (right).

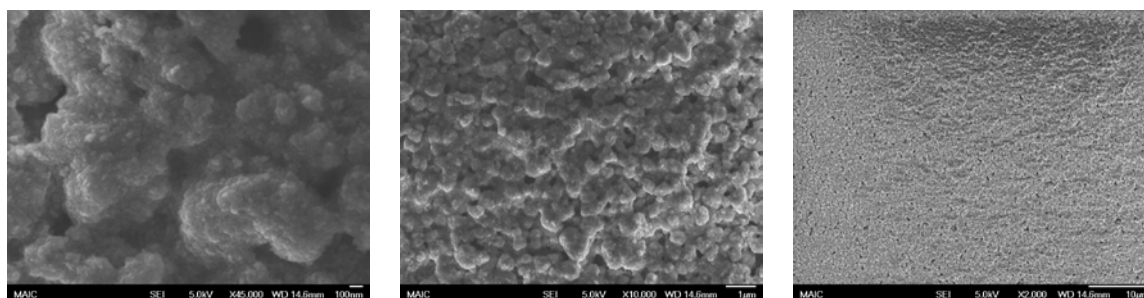


Figure 5-12. SEM of the TiO₂ film at various magnifications after 10 deposition cycles of the FeCr PBA from methanol.

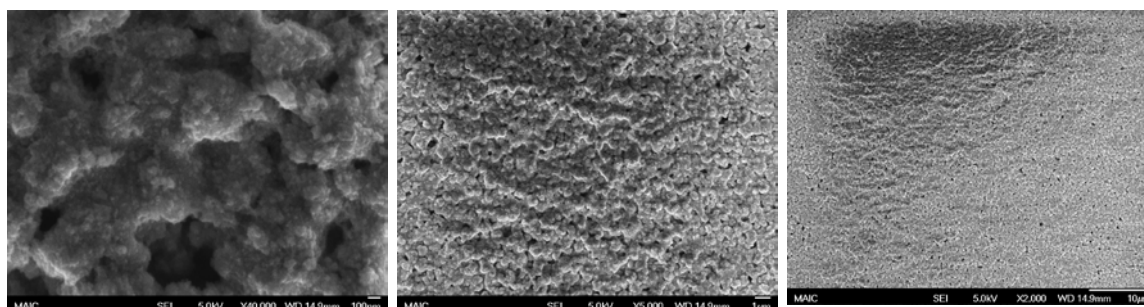


Figure 5-13. SEM of the TiO₂ film at various magnification after 20 deposition cycles of the FeCr PBA from methanol.

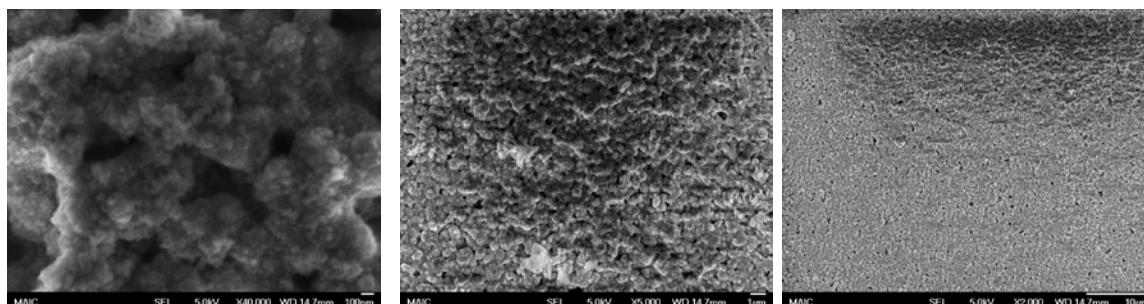


Figure 5-14. SEM of the TiO₂ film at various magnifications after 30 deposition cycles of the FeCr PBA from methanol.

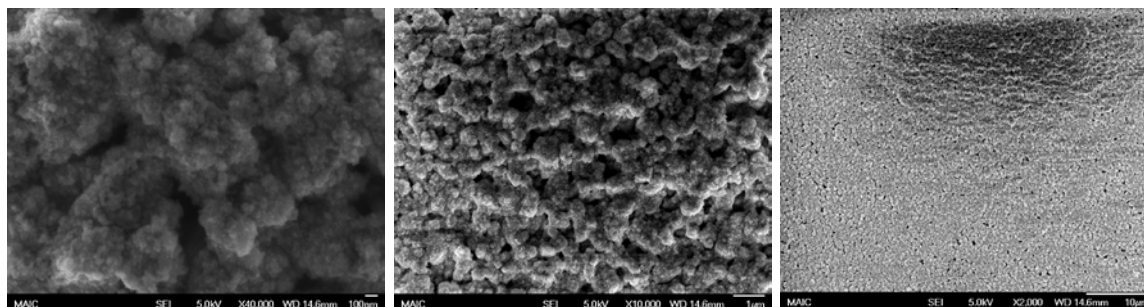


Figure 5-15. SEM of the TiO_2 film at various magnifications after 40 deposition cycles of the FeCr PBA from methanol.

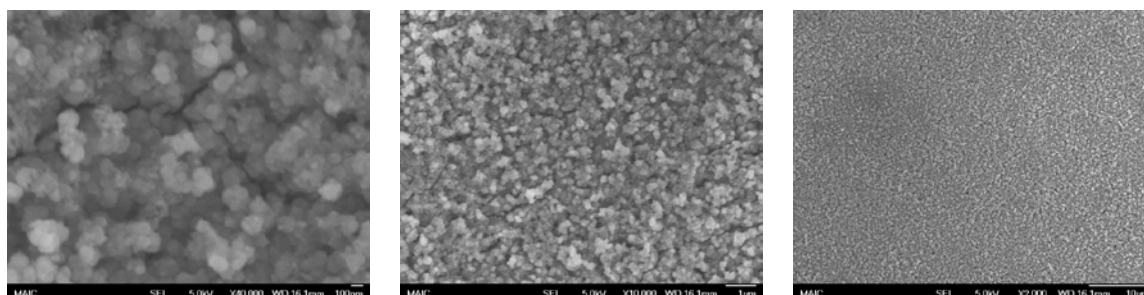


Figure 5-16. SEM of the TiO_2 film at various magnifications after 5 deposition cycles of the CoFe PBA from water.

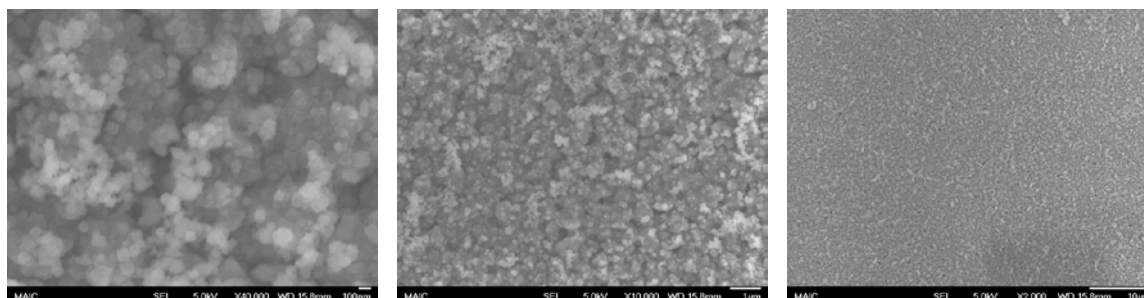


Figure 5-17. SEM of the TiO_2 film at various magnifications after 15 deposition cycles of the CoFe PBA from water.

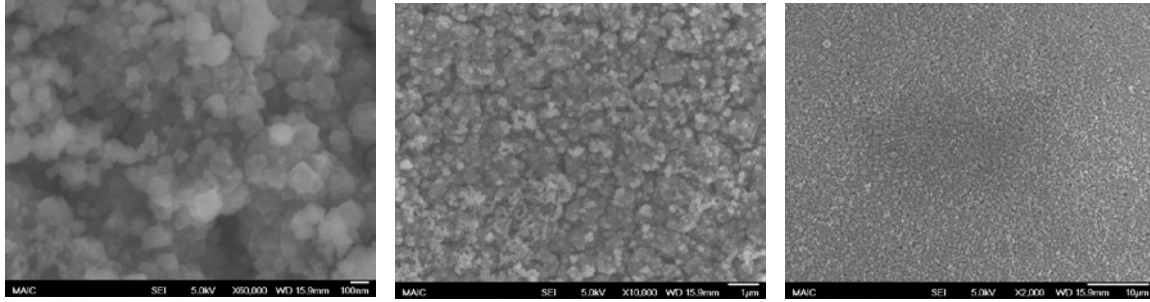


Figure 5-18. SEM of the TiO₂ film at various magnifications after 30 deposition cycles of the CoFe PBA from water.

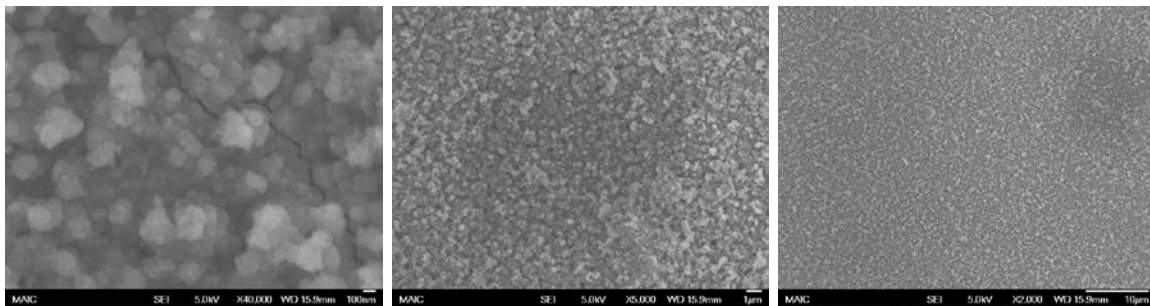


Figure 5-19. SEM of the TiO₂ film at various magnifications after 70 deposition cycles of the CoFe PBA from water. A desiccation crack is visible in the left image.

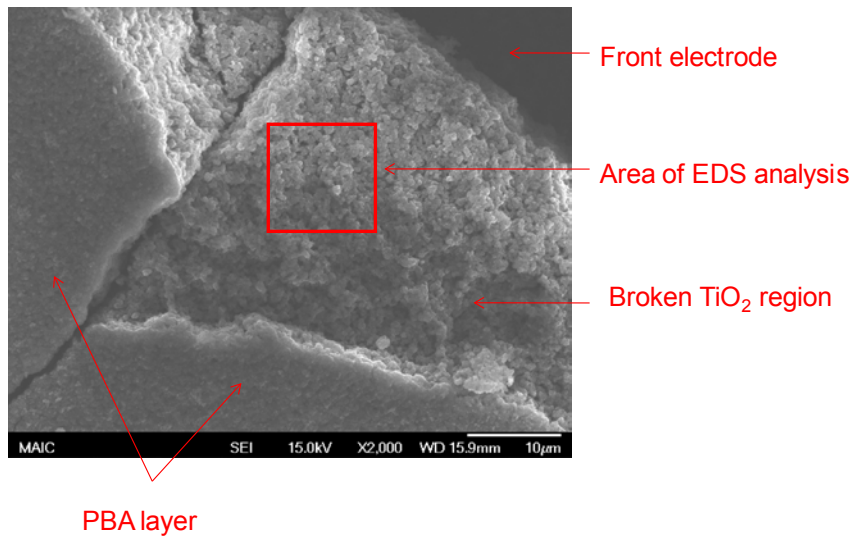


Figure 5-20. Area of EDS analysis on broken PBA-coated TiO₂ film.

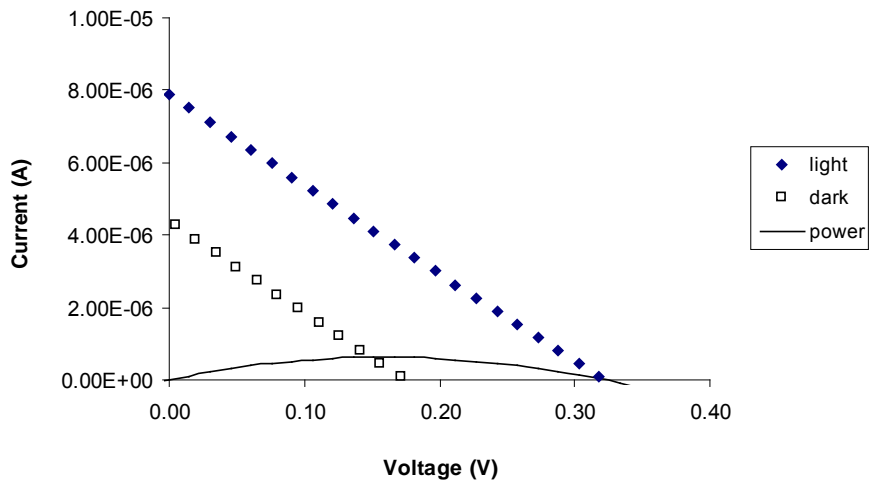


Figure 5-21. Photocurrent vs. voltage curve for the FeCr PBA cell

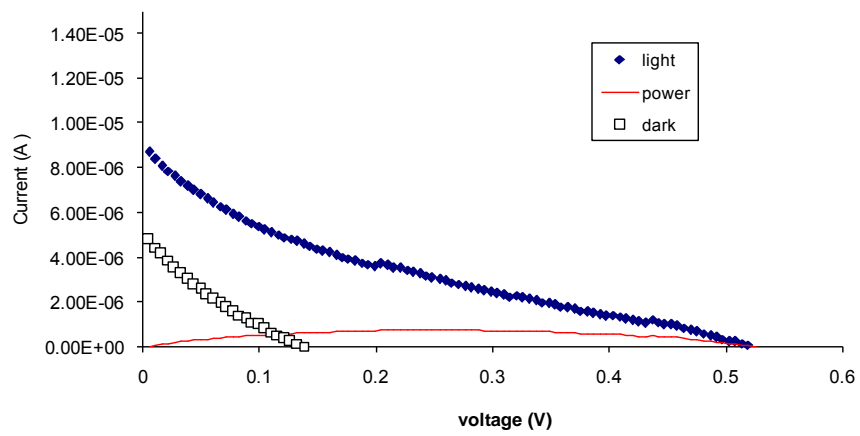


Figure 5-22. Photocurrent vs. voltage curve for the CoFe PBA cell

CHAPTER 6 CONCLUSION

Prussian blue analogs are a fascinating class of inorganic coordination polymer with diverse applications in the areas of supramolecular chemistry, charge storage, photocatalysis, and solid-state electrolytics. By varying the component metals in a PBA material, chemists can tailor electronic properties of the PBA such as HOMO and LUMO levels to suit specific applications. Various nanostructures of PBAs can be synthesized, such as nanoparticles, self-assembled monolayers, and thin films, providing a wide range of synthetic options and material geometries when incorporating them into devices. Applications of PBA that take advantage of their structural and electronic properties and that depend on the nano-scale nature of the materials were demonstrated.

The geometries of networked monolayers prepared at the air-water interface were controlled by rationally designing the geometry of the monolayer's underlying cyanometallate network. The films were characterized by ATR FT-IR, XPS, BAM, and surface pressure vs. mean molecular area isotherms. The resulting characterization of two of the three investigated systems was consistent with the formation of the desired primitive square networks. In the third system, improper charge balance was believed to be responsible for the system's failure to form the desired network. GXR D with a synchrotron X-ray source would be necessary to conclusively prove the geometry of the films. An attempt was made to synthesize magnetic films using more complex cyanometallate trimer units in the subphase, but these were unsuccessful.

Prussian blue was also used as a nano-scale charge storage medium for the creation of PB/TiO₂ nanocomposite materials in which photo-excited electrons are

transferred from the TiO_2 to the PB. The composite nanoparticles were photochromic, changing from blue to white upon UV irradiation. The PB material maintained charge balance during the electron accumulation by absorbing cations into its lattice.

Rhodamine B was able to sensitize the system to visible light, although a sacrificial iodide electron donor was necessary. It was hoped that the photocatalytic oxidizing activity of the TiO_2 would be enhanced by coupling it to the PB, but in trials the composite material did not show any enhanced ability to oxidize benzyl alcohol or isopropanol.

There are many potential future avenues to be explored with the PB/ TiO_2 composite material. These include directly coupling sensitizing dyes to the surface of the TiO_2 , investigation of the material's ability to carry out multi-electron reduction reactions, and modification of the PB's exposed surface with catalytic molecules or materials.

The feasibility of using thin films of PBAs as solid-state electrolytes in dye-sensitized solar cells was investigated. The efficiency of the resulting cells was low, most likely due to a low contact area between the PBA and the cell's TiO_2 substrate. The development of a technique for fabricating TiO_2 /PB film interfaces with a high surface contact area is a substantial challenge, but one that is worthwhile given the current intense interest in solid-state DSSCs and the relative neglect that solid inorganic electrolytic materials have received in DSSC research. Achieving a high surface area of interaction could be accomplished by varying the PBA deposition technique, the TiO_2 film geometry, or both.

In addition to optimization of the TiO₂/PBA interface, there are many other parameters to explore in the creation of DSSCs with PBA electrolytes. A nearly-limitless variety of dyes are available, and there are many alternate PBAs that could be investigated. There are also many possibilities for improvement in the fabrication process of the device, such as the incorporation of an insulating layer to separate the TiO₂ from the PBA.

There is great potential for varying the electronic properties of PBAs to suit desired applications, and recent advances have provided a wide variety of techniques for preparing nanoparticles and other nanostructures of PBA. It is hoped that this work will inspire others to further investigate the uses of PB and PBA nanostructures in photochemistry, photovoltaics, and other fields.

APPENDIX A
FT-IR SPECTRA OF SYNTHESIZED COMPOUNDS

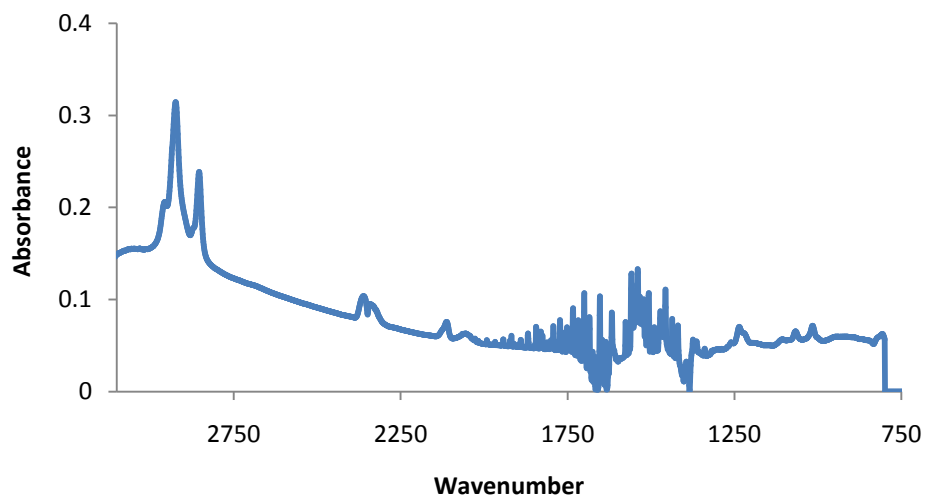


Figure A-1. FT-IR spectrum of Bis(tetramethylammonium)pentacyano(4-(didodecylamino)-pyridine) ferrate(III)

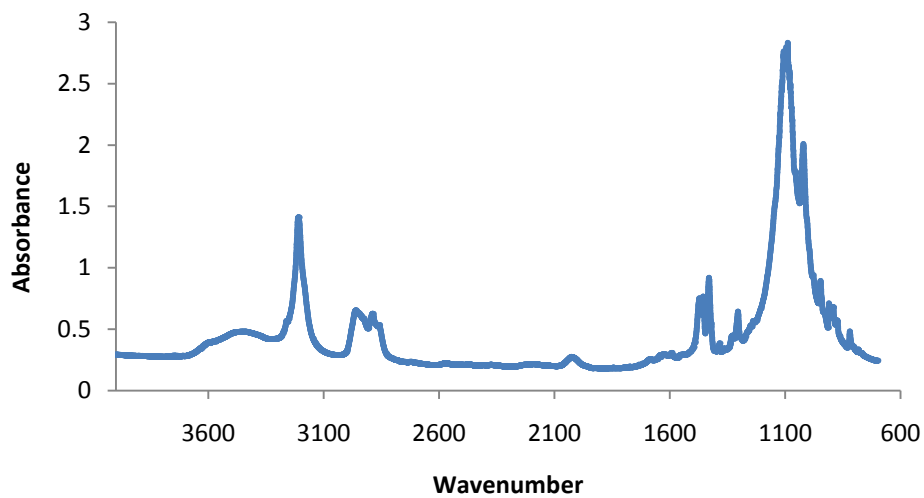


Figure A-2. FT-IR spectrum of 1-4-8-11 tetraazacyclotetradecane nickel (II) perchlorate

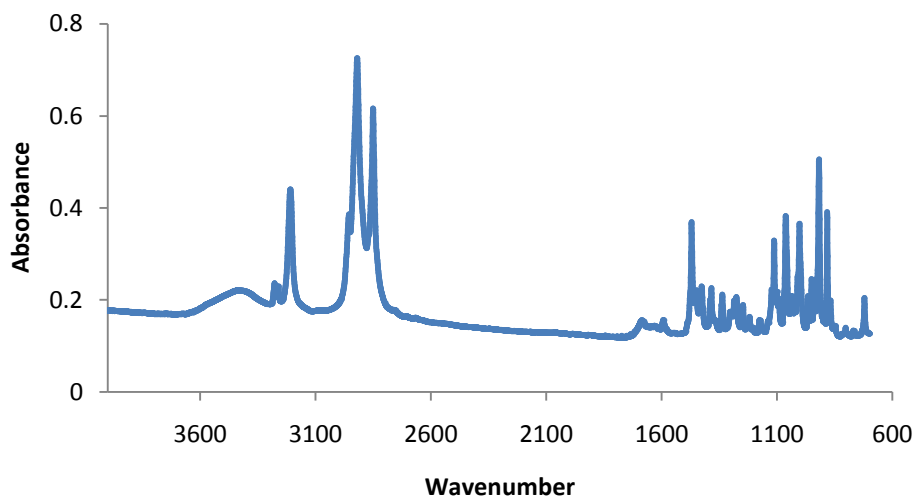


Figure A-3. FT-IR spectrum of 1-octadecyl-1-3-6-10-13 pentaazacyclotetradecane nickel (II) chloride

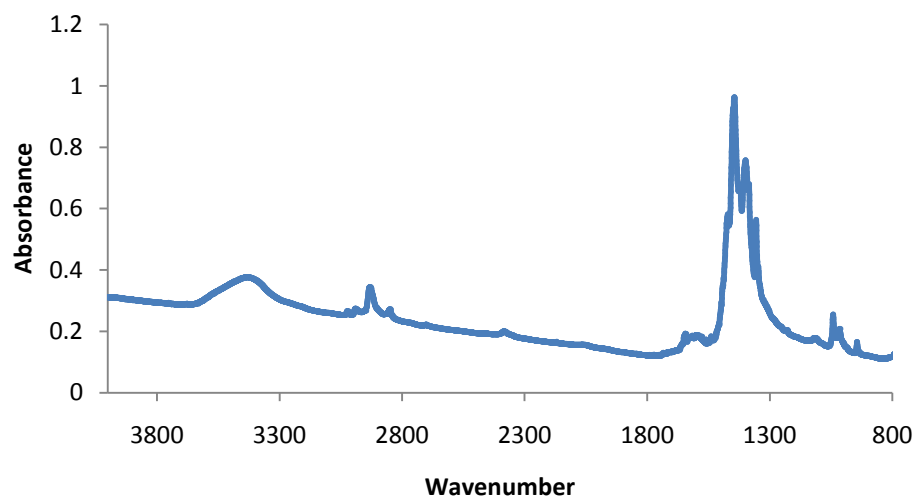


Figure A-4. FT-IR spectrum of Ru(II/III)tetracarboxylate chloride

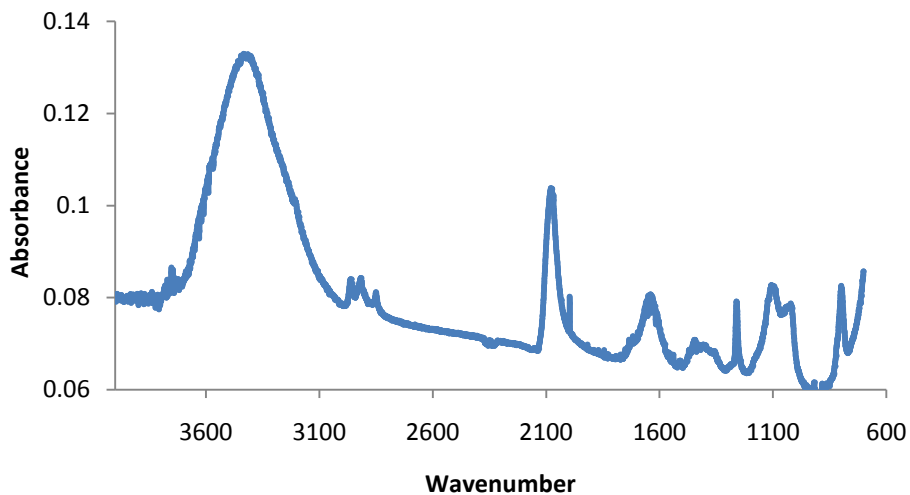


Figure A-5. FT-IR spectrum of Prussian blue nanoparticles

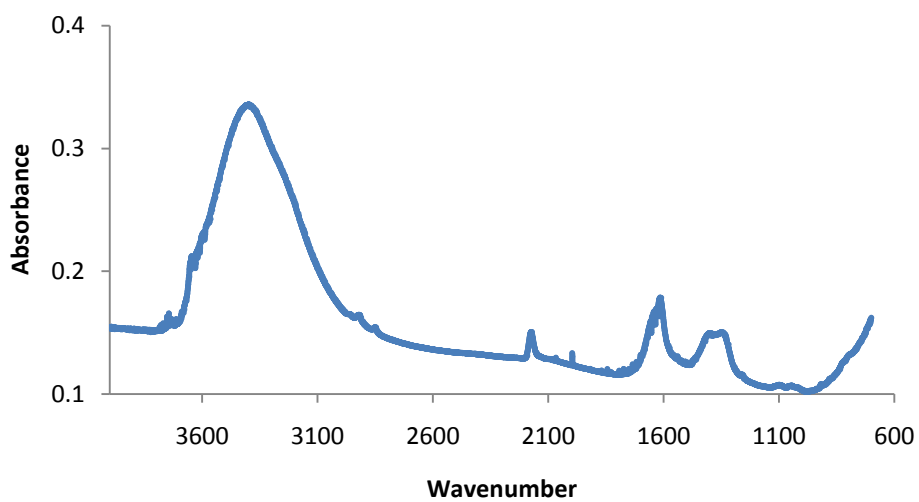


Figure A-6. FT-IR spectrum of NiCR Prussian blue analog nanoparticles

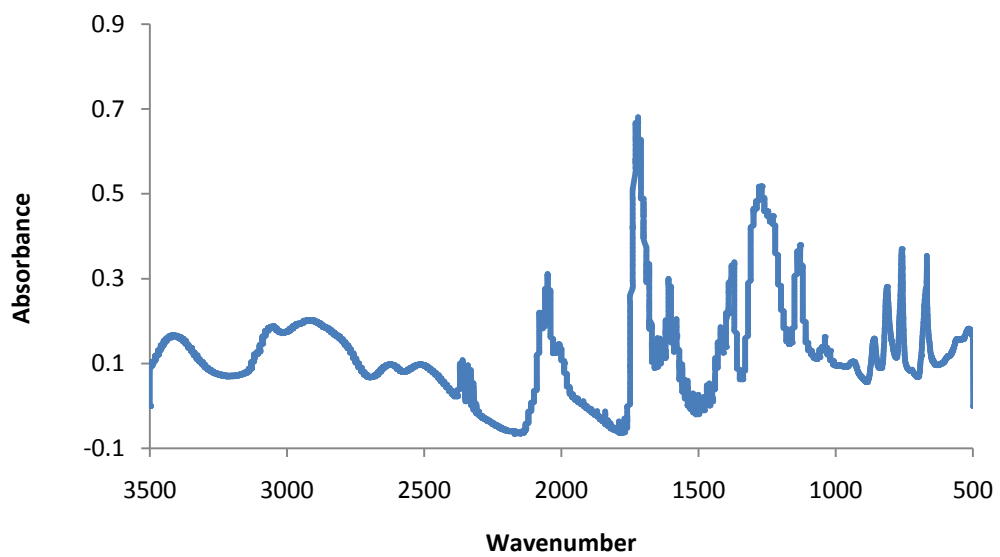


Figure A-7. FT-IR spectrum of (4,4'-dcbpy)₂(CN)₂Ru(II)

LIST OF REFERENCES

- (1) Xia, Y. N.; Rogers, J. A.; Paul, K. E.; Whitesides, G. M. *Chem Rev* **1999**, *99*, 1823-1848.
- (2) Eddaoudi, M.; Moler, D. B.; Li, H. L.; Chen, B. L.; Reineke, T. M.; O'Keeffe, M.; Yaghi, O. M. *Accounts Chem Res* **2001**, *34*, 319-330.
- (3) Philp, D.; Stoddart, J. F. *Angew Chem Int Edit* **1996**, *35*, 1155-1196.
- (4) Eddaoudi, M.; Kim, J.; Vodak, D.; Sudik, A.; Wachter, J.; O'Keeffe, M.; Yaghi, O. M. *Proceedings of the National Academy of Sciences of the United States of America* **2002**, *99*, 4900-4904.
- (5) Plevert, J.; Gentz, T. M.; Laine, A.; Li, H. L.; Young, V. G.; Yaghi, O. M.; O'Keeffe, M. *Journal of the American Chemical Society* **2001**, *123*, 12706-12707.
- (6) Yaghi, O. M.; O'Keeffe, M.; Ockwig, N. W.; Chae, H. K.; Eddaoudi, M.; Kim, J. *Nature* **2003**, *423*, 705-714.
- (7) Chae, H. K.; Eddaoudi, M.; Kim, J.; Hauck, S. I.; Hartwig, J. F.; O'Keeffe, M.; Yaghi, O. M. *Journal of the American Chemical Society* **2001**, *123*, 11482-11483.
- (8) Kim, J.; Chen, B. L.; Reineke, T. M.; Li, H. L.; Eddaoudi, M.; Moler, D. B.; O'Keeffe, M.; Yaghi, O. M. *Journal of the American Chemical Society* **2001**, *123*, 8239-8247.
- (9) Sudik, A. C.; Cote, A. P.; Yaghi, O. M. *Inorganic Chemistry* **2005**, *44*, 2998-3000.
- (10) Rosi, N. L.; Kim, J.; Eddaoudi, M.; Chen, B. L.; O'Keeffe, M.; Yaghi, O. M. *Journal of the American Chemical Society* **2005**, *127*, 1504-1518.
- (11) Rosi, N. L.; Eckert, J.; Eddaoudi, M.; Vodak, D. T.; Kim, J.; O'Keeffe, M.; Yaghi, O. M. *Science* **2003**, *300*, 1127-1129.
- (12) Rowsell, J. L. C.; Yaghi, O. M. *Angewandte Chemie-International Edition* **2005**, *44*, 4670-4679.
- (13) Banerjee, R.; Phan, A.; Wang, B.; Knobler, C.; Furukawa, H.; O'Keeffe, M.; Yaghi, O. M. *Science* **2008**, *319*, 939-943.
- (14) Schmittel, M.; Kalsani, V.; Mal, P.; Bats, J. W. *Inorganic Chemistry* **2006**, *45*, 6370-6377.
- (15) Culp, J. T.; Park, J. H.; Frye, F.; Huh, Y. D.; Meisel, M. W.; Talham, D. R. *Coordin Chem Rev* **2005**, *249*, 2642-2648.
- (16) Culp, J. T.; Park, J. H.; Meisel, M. W.; Talham, D. R. *Polyhedron* **2003**, *22*, 3059-3064.

- (17) Culp, J. T.; Park, J. H.; Benitez, I. O.; Huh, Y. D.; Meisel, M. W.; Talham, D. R. *Chem Mater* **2003**, *15*, 3431-3436.
- (18) Park, J. H.; Culp, J. T.; Hall, D. W.; Talham, D. R.; Meisel, M. W. *Physica B* **2003**, *329*, 1152-1153.
- (19) Culp, J. T.; Park, J. H.; Meisel, M. W.; Talham, D. R. *Inorg Chem* **2003**, *42*, 2842-2848.
- (20) Culp, J.; Davidson, M.; Duran, R. S.; Talham, D. R. *Langmuir* **2002**, *18*, 8260-8262.
- (21) Culp, J. T.; Park, J. H.; Stratakis, D.; Meisel, M. W.; Talham, D. R. *Journal of the American Chemical Society* **2002**, *124*, 10083-10090.
- (22) Culp, J. T.; Morgan, A. N.; Meisel, M. W.; Talham, D. R. *Mol Cryst Liq Cryst* **2002**, *376*, 383-388.
- (23) Vollhardt, D. *Materials Science & Engineering C-Biomimetic and Supramolecular Systems* **2002**, *22*, 121-127.
- (24) Knobler, C. M. *Molecular Crystals and Liquid Crystals* **2001**, *364*, 133-140.
- (25) Vollhardt, D. *Advances in Colloid and Interface Science* **1996**, *64*, 143-171.
- (26) Fukita, N.; Ohba, M.; Okawa, H.; Matsuda, K.; Iwamura, H. *Inorg Chem* **1998**, *37*, 842-848.
- (27) Vos, T. E.; Miller, J. S. *Angewandte Chemie-International Edition* **2005**, *44*, 2416-2419.
- (28) Vos, T. E.; Liao, Y.; Shum, W. W.; Her, J. H.; Stephens, P. W.; Reiff, W. M.; Miller, J. S. *Journal of the American Chemical Society* **2004**, *126*, 11630-11639.
- (29) Shum, W. W.; Liao, Y.; Miller, J. S. *Journal of Physical Chemistry A* **2004**, *108*, 7460-7462.
- (30) Liao, Y.; Shum, W. W.; Miller, J. S. *Journal of the American Chemical Society* **2002**, *124*, 9336-9337.
- (31) Shum, W. W.; Schaller, J. N.; Miller, J. S. *Journal of Physical Chemistry C* **2008**, *112*, 7936-7938.
- (32) Fishman, R. S.; Okamoto, S.; Shum, W. W.; Miller, J. S. *Physical Review B* **2009**, *80*, 64401-64406.
- (33) Shum, W. W.; Her, J. H.; Stephens, P. W.; Lee, Y. J.; Miller, J. S. *Advanced Materials* **2007**, *19*, 2910-2913.

- (34) Miller, J. S.; Vos, T. E.; Shum, W. W. *Advanced Materials* **2005**, *17*, 2251-2254.
- (35) Nowicka, B.; Rams, M.; Stadnicka, K.; Sieklucka, B. *Inorganic Chemistry* **2007**, *46*, 8123-8125.
- (36) Colacio, E.; Ghazi, M.; Stoeckli-Evans, H.; Lloret, F.; Moreno, J. M.; Perez, C. *Inorganic Chemistry* **2001**, *40*, 4876-4883.
- (37) Clemente-Leon, M.; Coronado, E.; Galan-Mascaros, J. R.; Gomez-Garcia, C. J.; Woike, T.; Clemente-Juan, J. M. *Inorganic Chemistry* **2001**, *40*, 87-94.
- (38) Shen, Z.; Zuo, J. L.; Shi, F. N.; Xu, Y.; Song, Y.; You, X. Z.; Raj, S. S. S.; Fun, H. K.; Zhou, Z. Y.; Che, C. M. *Transition Metal Chemistry* **2001**, *26*, 345-350.
- (39) Colacio, E.; Dominguez-Vera, J. M.; Ghazi, M.; Kivekas, R.; Lloret, F.; Moreno, J. M.; Stoeckli-Evans, H. *Chemical Communications* **1999**, 987-988.
- (40) Long, J.; Chamoreau, L. M.; Mathoniere, C.; Marvaud, V. *Inorganic Chemistry* **2009**, *48*, 22-24.
- (41) Mitchell, R. W.; Spencer, A.; Wilkinso.G *Journal of the Chemical Society-Dalton Transactions* **1973**, 846-854.
- (42) Ferreira, K. Q.; Doro, F. G.; Tfouni, E. *Inorganica Chimica Acta* **2003**, *355*, 205-212.
- (43) Choi, H. J.; Suh, M. P. *Inorganic Chemistry* **2003**, *42*, 1151-1157.
- (44) Otoole, T. R.; Sullivan, B. P.; Bruce, M. R. M.; Margerum, L. D.; Murray, R. W.; Meyer, T. J. *Journal of Electroanalytical Chemistry* **1989**, *259*, 217-239.
- (45) Lindsay, A. J.; Wilkinson, G.; Motevalli, M.; Hursthouse, M. B. *Journal of the Chemical Society-Dalton Transactions* **1985**, 2321-2326.
- (46) Mallah, T.; Thiebaut, S.; Verdaguer, M.; Veillet, P. *Science* **1993**, *262*, 1554-1557.
- (47) Entley, W. R.; Girolami, G. S. *Science* **1995**, *268*, 397-400.
- (48) Bignozzi, C. A.; Argazzi, R.; Bortolini, O.; Scandola, F.; Harriman, A. *New Journal of Chemistry* **1996**, *20*, 731-738.
- (49) Albores, P.; Slep, L. D.; Weyhermuller, T.; Baraldo, L. M. *Inorganic Chemistry* **2004**, *43*, 6762-6773.
- (50) Albores, P.; Rossi, M. B.; Baraldo, L. M.; Slep, L. D. *Inorganic Chemistry* **2006**, *45*, 10595-10604.

- (51) Ring, J.; Rothenberger, K. H.; Clauss, W. *International Archives of Allergy and Applied Immunology* **1985**, *78*, 9-14.
- (52) Ito, A.; Suenaga, M.; Ono, K. *Journal of Chemical Physics* **1968**, *48*, 3597-3599.
- (53) Verdaguer, M. *Polyhedron* **2001**, *20*, 1115-1128.
- (54) Verdaguer, M.; Bleuzen, A.; Marvaud, V.; Vaissermann, J.; Seuleiman, M.; Desplanches, C.; Scullier, A.; Train, C.; Garde, R.; Gelly, G.; Lomenech, C.; Rosenman, I.; Veillet, P.; Cartier, C.; Villain, F. *Coordination Chemistry Reviews* **1999**, *192*, 1023-1047.
- (55) Sato, O.; Einaga, Y.; Fujishima, A.; Hashimoto, K. *Inorganic Chemistry* **1999**, *38*, 4405-4412.
- (56) Park, J. H.; Cizmar, E.; Meisel, M. W.; Huh, Y. D.; Frye, F.; Lane, S.; Talham, D. R. *Applied Physics Letters* **2004**, *85*, 3797-3799.
- (57) Park, J. H.; Frye, F.; Anderson, N. E.; Pajerowski, D. M.; Huh, Y. D.; Talham, D. R.; Meisel, M. W. *Journal of Magnetism and Magnetic Materials* **2007**, *310*, 1458-1459.
- (58) Park, J. H.; Frye, F.; Lane, S.; Cizmar, E.; Huh, Y. D.; Talham, D. R.; Meisel, M. W. *Polyhedron* **2005**, *24*, 2355-2359.
- (59) Pajerowski, D. M.; Frye, F. A.; Talham, D. R.; Meisel, M. W. *New Journal of Physics* **2007**, *9*
- (60) Frye, F.; Park, J. H.; Anderson, N.; Lane, S. M.; Meisel, M. W.; Talham, D. R. *Abstracts of Papers of the American Chemical Society* **2006**, *231*
- (61) Frye, F. A.; Pajerowski, D. M.; Anderson, N. E.; Long, J.; Park, J. H.; Meisel, M. W.; Talham, D. R. *Polyhedron* **2007**, *26*, 2273-2275.
- (62) Frye, F. A.; Pajerowski, D. M.; Park, J. H.; Meisel, M. W.; Talham, D. R. *Chemistry of Materials* **2008**, *20*, 5706-5713.
- (63) Frye, F. A.; Pajerowski, D. M. B.; Lane, S. M.; Anderson, N. E.; Park, J. H.; Meisel, M. W.; Talham, D. R. *Polyhedron* **2007**, *26*, 2281-2286.
- (64) Kobayashi, T.; Ito, K.; Katoh, N.; Kuwabara, K. *Bulletin of Electrochemistry* **2004**, *20*, 377-383.
- (65) Sone, K.; Konishi, K.; Yagi, M. *Chemistry-a European Journal* **2006**, *12*, 8558-8565.
- (66) Ricci, F.; Goncalves, C.; Amine, A.; Gorton, L.; Palleschi, G.; Moscone, D. *Electroanalysis* **2003**, *15*, 1204-1211.

- (67) Ricci, F.; Palleschi, G.; Yigzaw, Y.; Gorton, L.; Ruzgas, T.; Karyakin, A. *Electroanalysis* **2003**, *15*, 175-182.
- (68) Moon, S. B.; Xidis, A.; Neff, V. D. *Journal of Physical Chemistry* **1993**, *97*, 1634-1638.
- (69) Xidis, A.; Neff, V. D. *Journal of the Electrochemical Society* **1991**, *138*, 3637-3642.
- (70) Mccargar, J. W.; Neff, V. D. *Journal of Physical Chemistry* **1988**, *92*, 3598-3604.
- (71) Itaya, K.; Uchida, I.; Neff, V. D. *Accounts of Chemical Research* **1986**, *19*, 162-168.
- (72) Neff, V. D. *Journal of the Electrochemical Society* **1985**, *132*, 1382-1384.
- (73) Rajan, K. P.; Neff, V. D. *Journal of Physical Chemistry* **1982**, *86*, 4361-4368.
- (74) Ellis, D.; Eckhoff, M.; Neff, V. D. *Journal of Physical Chemistry* **1981**, *85*, 1225-1231.
- (75) Neff, V. D. *Journal of the Electrochemical Society* **1978**, *125*, 886-887.
- (76) DeLongchamp, D. M.; Hammond, P. T. *Chemistry of Materials* **2004**, *16*, 4799-4805.
- (77) Lin, R. J.; Toshima, N. *Bulletin of the Chemical Society of Japan* **1991**, *64*, 136-148.
- (78) Leventis, N.; Chung, Y. C. *Journal of the Electrochemical Society* **1991**, *138*, L21-L23.
- (79) Matsumoto, F. M.; Temperini, M. L. A.; Toma, H. E. *Electrochimica Acta* **1994**, *39*, 385-391.
- (80) Sone, Y.; Kishimoto, A.; Kudo, T.; Ikeda, K. *Solid State Ionics* **1996**, *83*, 135-143.
- (81) Agnihotry, S. A. *Bulletin of Electrochemistry* **1996**, *12*, 707-712.
- (82) Koncki, R.; Wolfbeis, O. S. *Analytical Chemistry* **1998**, *70*, 2544-2550.
- (83) Dostal, A.; Kauschka, G.; Reddy, S. J.; Scholz, F. *Journal of Electroanalytical Chemistry* **1996**, *406*, 155-163.
- (84) Zadroncki, M.; Linek, I. A.; Stroka, J.; Wrona, P. K.; Gajus, Z. *Journal of the Electrochemical Society* **2001**, *148*, E348-E355.
- (85) Kelly, M. T.; Arbuckle-Keil, G. A.; Johnson, L. A.; Su, E. Y.; Amos, L. J.; Chun, J. K. M.; Bocarsly, A. B. *Journal of Electroanalytical Chemistry* **2001**, *500*, 311-321.

- (86) Hartman, M. R.; Peterson, V. K.; Liu, Y.; Kaye, S. S.; Long, J. R. *Chemistry of Materials* **2006**, *18*, 3221-3224.
- (87) Kaye, S. S.; Long, J. R. *Journal of the American Chemical Society* **2005**, *127*, 6506-6507.
- (88) Chapman, K. W.; Southon, P. D.; Weeks, C. L.; Kepert, C. J. *Chemical Communications* **2005**, 3322-3324.
- (89) Murray, L. J.; Dinca, M.; Long, J. R. *Chemical Society Reviews* **2009**, *38*, 1294-1314.
- (90) Davidson, D.; Welo, L. A. *J Phys Chem-Us* **1928**, *32*, 1191-1196.
- (91) Karyakin, A. A. *Electroanal* **2001**, *13*, 813-819.
- (92) Koncki, R. *Crit Rev Anal Chem* **2002**, *32*, 79-96.
- (93) Day, P.; Herren, F.; Ludi, A.; Gudel, H. U.; Hulliger, F.; Givord, D. *Helvetica Chimica Acta* **1980**, *63*, 148-153.
- (94) Ludi, A.; Gudel, H. U.; Rugg, M. *Inorganic Chemistry* **1970**, *9*, 2224-2227.
- (95) Ludi, A.; Gudel, H. U.; Hugli, R. *Chimia* **1969**, *23*, 2255-2260.
- (96) Buser, H. J.; Schwarzenbach, D.; Petter, W.; Ludi, A. *Inorganic Chemistry* **1977**, *16*, 2704-2710.
- (97) Serrano, E.; Rus, G.; Garcia-Martinez, J. *Renewable & Sustainable Energy Reviews* **2009**, *13*, 2373-2384.
- (98) Tada, H.; Kiyonaga, T.; Naya, S. *Chemical Society Reviews* **2009**, *38*, 1849-1858.
- (99) Ravelli, D.; Dondi, D.; Fagnoni, M.; Albini, A. *Chemical Society Reviews* **2009**, *38*, 1999-2011.
- (100) Yu, H. T.; Quan, X. *Progress in Chemistry* **2009**, *21*, 406-419.
- (101) Malato, S.; Blanco, J.; Alarcon, D. C.; Maldonado, M. I.; Fernandez-Ibanez, P.; Gernjak, W. *Catalysis Today* **2007**, *122*, 137-149.
- (102) Pelizzetti, E.; Minero, C. *Electrochimica Acta* **1993**, *38*, 47-55.
- (103) Shankar, K.; Basham, J. I.; Allam, N. K.; Varghese, O. K.; Mor, G. K.; Feng, X. J.; Paulose, M.; Seabold, J. A.; Choi, K. S.; Grimes, C. A. *Journal of Physical Chemistry C* **2009**, *113*, 6327-6359.

- (104) Iwata, K.; Takaya, T.; Hamaguchi, H.; Yamakata, A.; Ishibashi, T. A.; Onishi, H.; Kuroda, H. *J Phys Chem B* **2004**, *108*, 20233-20239.
- (105) Subramanian, V.; Wolf, E. E.; Kamat, P. V. *Langmuir* **2003**, *19*, 469-474.
- (106) Subramanian, V.; Wolf, E. E.; Kamat, P. V. *J Am Chem Soc* **2004**, *126*, 4943-4950.
- (107) Nishijima, K.; Fujisawa, Y.; Murakami, N.; Tsubota, T.; Ohno, T. *Applied Catalysis B-Environmental* **2008**, *84*, 584-590.
- (108) Kontos, A. I.; Likodimos, V.; Stergiopoulos, T.; Tsoukleris, D. S.; Falaras, P.; Rabias, I.; Papavassiliou, G.; Kim, D.; Kunze, J.; Schmuki, P. *Chemistry of Materials* **2009**, *21*, 662-672.
- (109) Obare, S. O.; Ito, T.; Meyer, G. J. *Journal of the American Chemical Society* **2006**, *128*, 712-713.
- (110) Obare, S. O.; Ito, T.; Meyer, G. J. *Environmental Science & Technology* **2005**, *39*, 6266-6272.
- (111) Viehbeck, A.; Deberry, D. W. *Journal of the Electrochemical Society* **1985**, *132*, 1369-1375.
- (112) Itaya, K.; Uchida, I.; Toshima, S.; Delarue, R. M. *Journal of the Electrochemical Society* **1984**, *131*, 2086-2091.
- (113) Deberry, D. W.; Viehbeck, A. *Journal of the Electrochemical Society* **1983**, *130*, 249-251.
- (114) Ogura, K. *Journal of the Electrochemical Society* **1987**, *134*, 2749-2754.
- (115) de Tacconi, N. R.; Rajeshwar, K.; Lezna, R. O. *Electrochimica Acta* **2000**, *45*, 3403-3411.
- (116) Szacilowski, K.; Macyk, W.; Stochel, G. *Journal of Materials Chemistry* **2006**, *16*, 4603-4611.
- (117) Song, Y. Y.; Zhang, K.; Xia, X. H. *Applied Physics Letters* **2006**, *88*, 531121-531125.
- (118) Tada, H.; Saito, Y.; Kawahara, H. *Journal of the Electrochemical Society* **1991**, *138*, 140-144.
- (119) Brinzei, D.; Catala, L.; Louvain, N.; Rogez, G.; Stephan, O.; Gloter, A.; Mallah, T. *Journal of Materials Chemistry* **2006**, *16*, 2593-2599.
- (120) Tada, H.; Tsuji, S.; Ito, S. *Journal of Colloid and Interface Science* **2001**, *239*, 196-199.

- (121) Rothenberger, G.; Moser, J.; Gratzel, M.; Serpone, N.; Sharma, D. K. *Journal of the American Chemical Society* **1985**, *107*, 8054-8059.
- (122) Oregan, B.; Gratzel, M. *Nature* **1991**, *353*, 737-740.
- (123) Jose, R.; Thavasi, V.; Ramakrishna, S. *J Am Ceram Soc* **2009**, *92*, 289-301.
- (124) Li, K. X.; Yu, Z. X.; Luo, Y. H.; Li, D. M.; Meng, Q. B. *J Mater Sci Technol* **2007**, *23*, 577-582.
- (125) Lin, C. Y.; Lo, C. F.; Luo, L.; Lu, H. P.; Hung, C. S.; Diau, E. W. G. *Journal of Physical Chemistry C* **2009**, *113*, 755-764.
- (126) de Tacconi, N. R.; Chanmanee, W.; Rajeshwar, K.; Rochford, J.; Galoppini, E. *Journal of Physical Chemistry C* **2009**, *113*, 2996-3006.
- (127) Odobel, F.; Blart, E.; Lagree, M.; Villieras, M.; Boujtita, H.; El Murr, N.; Caramori, S.; Bignozzi, C. A. *Journal of Materials Chemistry* **2003**, *13*, 502-510.
- (128) Ma, T. L.; Inoue, K.; Yao, K.; Noma, H.; Shuji, T.; Abe, E.; Yu, J. H.; Wang, X. S.; Zhang, B. W. *Journal of Electroanalytical Chemistry* **2002**, *537*, 31-38.
- (129) Rao, T. N.; Bahadur, L. *Journal of the Electrochemical Society* **1997**, *144*, 179-185.
- (130) Arbeloa, F. L.; Martinez, V. M.; Arbeloa, T.; Arbeloa, I. L. *Journal of Photochemistry and Photobiology C-Photochemistry Reviews* **2007**, *8*, 85-108.
- (131) Dai, Q.; Rabani, J. *Journal of Photochemistry and Photobiology a-Chemistry* **2002**, *148*, 17-24.
- (132) Hagglund, C.; Zach, M.; Kasemo, B. *Applied Physics Letters* **2008**, *92*, 13113/1-13113/5.
- (133) Robertson, N. *Angew Chem Int Edit* **2006**, *45*, 2338-2345.
- (134) Gratzel, M. *Journal of Photochemistry and Photobiology a-Chemistry* **2004**, *164*, 3-14.
- (135) Oskam, G.; Bergeron, B. V.; Meyer, G. J.; Searson, P. C. *Journal of Physical Chemistry B* **2001**, *105*, 6867-6873.
- (136) Gorlov, M.; Kloo, L. *Dalton Transactions* **2008**, 2655-2666.
- (137) Kawano, R.; Matsui, H.; Matsuyama, C.; Sato, A.; Susan, M. A. B. H.; Tanabe, N.; Watanabe, M. *Journal of Photochemistry and Photobiology a-Chemistry* **2004**, *164*, 87-92.

- (138) Wang, P.; Zakeeruddin, S. M.; Exnar, I.; Gratzel, M. *Chemical Communications* **2002**, 2972-2973.
- (139) Usui, H.; Matsui, H.; Tanabe, N.; Yanagida, S. *Journal of Photochemistry and Photobiology a-Chemistry* **2004**, 164, 97-101.
- (140) de Freitas, J. N.; Nogueira, A. F.; De Paoli, M. A. *Journal of Materials Chemistry* **2009**, 19, 5279-5294.
- (141) Li, B.; Wang, L. D.; Kang, B. N.; Wang, P.; Qiu, Y. *Solar Energy Materials and Solar Cells* **2006**, 90, 549-573.
- (142) Guenes, S.; Sariciftci, N. S. *Inorganica Chimica Acta* **2008**, 361, 581-588.
- (143) Li, D. M.; Qin, D.; Deng, M. H.; Luo, Y. H.; Meng, Q. B. *Energ Environ Sci* **2009**, 2, 283-291.
- (144) Nogueira, A. F.; Longo, C.; De Paoli, M. A. *Coordination Chemistry Reviews* **2004**, 248, 1455-1468.
- (145) Tennakone, K.; Perera, V. P. S.; Kottegoda, I. R. M.; Kumara, G. R. R. A. *Journal of Physics D-Applied Physics* **1999**, 32, 374-379.
- (146) Karlsson, P. G.; Bolik, S.; Richter, J. H.; Mahrov, B.; Johansson, E. M. J.; Blomquist, J.; Uvdal, P.; Rensmo, H.; Siegbahn, H.; Sandell, A. *Journal of Chemical Physics* **2004**, 120, 11224-11232.
- (147) Kumara, G. R. A.; Kaneko, S.; Okuya, M.; Tennakone, K. *Langmuir* **2002**, 18, 10493-10495.
- (148) Tennakone, K.; Senadeera, G. K. R.; De Silva, D. B. R. A.; Kottegoda, I. R. M. *Applied Physics Letters* **2000**, 77, 2367-2369.
- (149) Kumara, G. R. R. A.; Konno, A.; Senadeera, G. K. R.; Jayaweera, P. V. V.; De Silva, D. B. R. A.; Tennakone, K. *Solar Energy Materials and Solar Cells* **2001**, 69, 195-199.
- (150) Kulesza, P. J.; Karwowska, B. *Journal of Electroanalytical Chemistry* **1996**, 401, 201-206.
- (151) Malik, M. A.; Kulesza, P. J.; Marassi, R.; Nobili, F.; Miecznikowski, K.; Zamponi, S. *Electrochimica Acta* **2004**, 49, 4253-4258.
- (152) Dostal, A.; Schroder, U.; Scholz, F. *Inorg Chem* **1995**, 34, 1711-1717.
- (153) Heimer, T. A.; Bignozzi, C. A.; Meyer, G. J. *J Phys Chem-Us* **1993**, 97, 11987-11994.

- (154) Ai, X.; Guo, J. C.; Anderson, N. A.; Lian, T. Q. *J Phys Chem B* **2004**, *108*, 12795-12803.
- (155) Sone, K.; Teraguchi, M.; Kaneko, T.; Aoki, T.; Yagi, M. *Chemphyschem* **2007**, *8*, 1357-1362.
- (156) Castro, S. S. L.; Mortimer, R. J.; de Oliveira, M. F.; Stradiotto, N. R. *Sensors* **2008**, *8*, 1950-1959.
- (157) Michel, R.; Reviakine, I.; Sutherland, D.; Fokas, C.; Csucs, G.; Danuser, G.; Spencer, N. D.; Textor, M. *Langmuir* **2002**, *18*, 8580-8586.
- (158) Choi, Y. C.; Yang, S. A.; Kim, J.; Jeong, K. O.; Cho, S. Y.; Bu, S. D. *Nanotechnology* **2009**, *20*, 425601-425605.
- (159) Masuda, H.; Kanazawa, K.; Nakao, M.; Yokoo, A.; Tamamura, T.; Sugiura, T.; Minoura, H.; Nishio, K. *Advanced Materials* **2003**, *15*, 159-161.

BIOGRAPHICAL SKETCH

Ian Ammon Rummel was born in 1981 in Arkansas to Chris and Cindy Rummel. He grew up in Arkansas, Colorado, California, Florida, and South Dakota. His undergraduate degree in chemistry was obtained at Hendrix College in Conway, Arkansas in 2004. While attending the University of Florida's Chemistry Department graduate visitation day in the spring of 2004 he met his future wife Julia Laney, a fellow visiting graduate student. During their first semester as graduate students at UF Ian and Julia coincidentally moved into the same apartment complex, were assigned to TA the same general chemistry class, and were assigned the same departmental mailbox. On March 11th of 2006 they gave in to the inevitable and were married in a ceremony in Livermore KY. He obtained his PhD in inorganic chemistry from UF in the fall of 2009.